Development of Flexible Lithium Sulfur Batteries Based on Laser-Induced Graphene

by

Ngai Yan Lau

A thesis

presented to the University of Waterloo

in fulfilment of the

thesis requirement for the degree of

Master of Applied Science

in

Chemical Engineering (Nanotechnology)

Waterloo, Ontario, Canada, 2018

Author's Declaration

I hereby declare that I am the sole author of this thesis. This is a true copy of the thesis, including any required final revisions, as accepted by my examiners.

I understand that my thesis may be made electronically available to the public.

Abstract

Emerging technologies have become increasingly advanced with flexible components and are integrated into various interfaces, finding themselves in applications such as rollable displays, wearable technologies and e-textiles. As a result, there is a need for a fully flexible battery with higher energy storage capacity that is simple to fabricate while being cost effective. While most commercially available flexible and thin-film batteries are formed through microfabrication techniques and other high capital cost methods, there is a need to explore higher energy density chemistries and determine a more cost-effective route to fabricating such batteries for the mass production and wide-spread use of flexible batteries.

The work in this thesis focused on the adaptation of a recently reported laser-scribing method to produce interdigitated electrodes from laser-induced graphene (LIG) towards the development of flexible lithium-sulfur (LiS) batteries. A proof of concept was demonstrated for this graphene material through sequentially patterning and depositing the active materials, sulfur and lithium, into the LIG fingers. A novel technique to introduce sulfur into carbon-based fingers was presented by the heterogeneous nucleation of sulfur crystals followed by their melting to wet the graphene and uniformly distribute within the porous network formed. In order introduce a dense lithium metal anode onto the porous substrate, silver nanoparticles were used as seeds for electrodeposition and a reverse pulse plating (RPP) technique was also utilized to reduce the lithium protrusions that would eventually form dendrites and high irreversible capacity loss due to the high surface area for solid electrolyte interface (SEI) formation.

Initial cycling displayed energy densities that exceeded lithium-ion microbatteries and thin-film batteries fabricated through microfabrication at almost 200 mWh/cm^3. However, the obtainable discharge capacities faded at the second cycle, suggesting a significant irreversible source of capacity loss. It was then determined the source to be a likely unstable solid electrolyte interphase (SEI) at the anode of the battery. Additionally, there was the finding of a prominent presence of macropores within the electrodes leading to an agglomeration of insulating sulfur within the pores that cannot be utilized in cycling.

The combination of two of the major conclusions from the initial proof of concept propelled the investigations of improving the defectiveness of the LIG and control over the LIG structure as well as Li plating efficiency on various carbons in different electrolytes. From the studies on LIG structure control, it was found that a lower power led to a reduced flux of gas evolution during a reduced local temperature induction upon laser irradiation. Thus, the formed electrodes are typically more dense, possessing a higher surface area with a reduced volume. Although the electrodes become less conductive with a reduced power, the conductivity can be improved, and the graphene annealed through several laser passes or the defocusing of the laser beam.

In the Li plating study, ether-based electrolytes were found to be detrimental to the cycling of plated lithium on the carbon electrodes, regardless of whether it was on a hard carbon with more sp^3 regions or a soft carbon with mainly sp^2 regions. This is because of solvent co-intercalation during lithium insertion and also the unstable SEI formed. Graphite, the soft carbon, performs best as a Li plating substrate in a carbonate-based electrolyte with a LiTFSI salt, while carbonized poly(furfuryl alcohol) (CPFA), a hard carbon, performs best in a carbonate-based electrolyte with a $LiClO_4$.

While further research is needed to understand how to control the carbonization of the PI to achieve a level of "hardness" or "softness" in the carbon, the results presented in this work contribute to the understanding of the novel LIG material in addition to the field of lithium electroplating onto substrates for the reduction of excess lithium use. Finally, the successful demonstration of a proof of concept of LiS batteries from LIG in an open architecture makes it possible for a number of future *in operando* analyses and characterizations of the LiS battery chemistry towards their commercialization.

Acknowledgements

I would like to thank my supervisor, Dr. Michael Pope, for taking me in and giving me the opportunity and space to explore and grow as a researcher. Thank you for urging me to keep pushing through the numerous challenges in my project while also being a compassionate and understanding supervisor.

I am also incredibly thankful for the pleasant group of people that I have had the opportunity to work with and know during my time in the research group. Particularly, I would like to thank from the bottom of my heart DY, MA, GH and AX for their friendships that have supported me in so many ways and especially so in the last few months leading to the consummation of this thesis work. Special thanks to GH for helping me revise my thesis and providing so many valuable suggestions.

I would additionally like to thank SX for his dedication and labour in providing me with the hard carbon material used in my work, even in the last day before he was flying back to China. I would also like to offer my gratitude towards Dr. Jeff Gostick for allowing me to work with the brand new surface area analyzer in the lab and MAM for training me on it and helping me fix it when I dislodged the hook that one time.

Dad, mom, Steven and grandma: thank you for constantly supporting me and loving me unconditionally throughout my undergraduate studies and masters. Thank you all for being proud of me and encouraging me to always look at the big picture.

I would like to also thank my friends from Grad Cell and Simply Church, and my mentor, CW, for walking with me and urging me to press on in light of eternity. Lastly, Ryan, thank you for being my emotional support, showing me ἀγάπη and being unceasingly patient with me especially when I need the reminder time and time again that it is to God that all glory is owed.

Dedication

To my family, Ryan and the true Maker who has shown me that I am merely a builder and discoverer.

Table of Contents

List of Figures

List of Tables

List of Abbreviations

Ag NP	Silver nanoparticles
ALD	Atomic layer deposition
BET	Brunauer-Emmett-Teller theory used for adsorption of gas molecules towards the determination of specific surface areas of different materials
BSD	Backscattered electron detector
CA	Contact angle
CE	Counter electrode
CEff	Coulombic efficiency
CNT	Carbon nanotubes
CPE	Constant phase element
CPFA	Carbonized poly(furfuryl alcohol)
CVD	Chemical vapour deposition
DC	Direct current
DI	Deionized water
DLW	Direct laser writing
DMC	Dimethyl carbonate
DME	Dimethoxy ethane
DMSO	Dimethyl sulfoxide
DOL	1,3-dioxolane

EC	Ethylene carbonate
EDL	Electric double layer
EDLC	Electric double layer capacitor
EDX	Energy-dispersive x-ray spectroscopy
EIS	Electrochemical impedance spectroscopy
EMImTFSI	1-ethyl-3-methylimidazolium bis(trifluoromethylsulfonylimide)
FA	Furfuryl alcohol
FWHM	Full width half maximum
GO	Graphene oxide
HER	Hydrogen evolution reaction
IoT	Internet of Things
LIG	Laser induced graphene
LiPSS	Lithium polysulfide species
LiS	Lithium sulfur
LiTFSI	Lithium bis(trifluorimethylsulfonylimide)
LSFB	Lithium sulfur flexible battery
NMP	N-methyl-2-pyrrolidone
NP	Nanoparticle
OER	Oxygen evolution reaction
P&S	Plating and stripping
PANI	Polyaniline

PDMS	Polydimethylsiloxane
PEDOT	Poly(3,4-ethylenedioxythiophene)
PFA	Poly(furfuryl alcohol)
PI	Polyimide
PMMA	Poly(methyl methacrylate)
PSS	Polystyrene sulfonate
PVDF	Polyvinylidene fluoride
PZT	Lead zirconate titanate
R2R	Roll-to-roll
RF	Radio frequency
rGO	Reduced graphene oxide
RPP	Reverse pulse plating
RTIL	Room temperature ionic liquid
SEI	Solid electrolyte interphase
SEM	Scanning electron microscopy
SNR	Signal-to-noise-ratio
TGA	Thermogravimetric analysis
WE	Working electrode
XRD	X-ray diffraction

"This act [creation], as it is for God, must always remain totally inconceivable to man. For we – even our poets and musicians and inventors – never, in the ultimate sense make. We only build. We always have materials to build from. All we can know about the act of creation must be derived from what we gather about the relation of the creatures to their Creator."

- C.S. Lewis, Letters to Malcom: Chiefly on Prayer

1.0 Introduction

1.1 The Need for Flexible Batteries

According to StatCounter, in 2016, the global usage of mobile and tablet devices for internet access has finally exceeded that of the usage of a desktop computer [1]. This is an important point in history as it is an indicator of the obvious transition into a technological era where desktops are no longer the preferred instrument for connecting to the internet, but rather, mobile devices, wearable technology and other portable devices are [2]. This is the emergence of the Internet of Things (IoT), where everyone and everything can be connected in a network and data can be transferred to and from [3]. The requirement to connect all these physical devices and other items with embedded sensors and circuits is to have an energy source to power it. Specifically, many of these devices need a certain level of mobility and the added sensors, circuit and energy source must also be sufficiently flexible or conformable. Figure 1 depicts several examples of such emerging technologies requiring flexible energy sources.

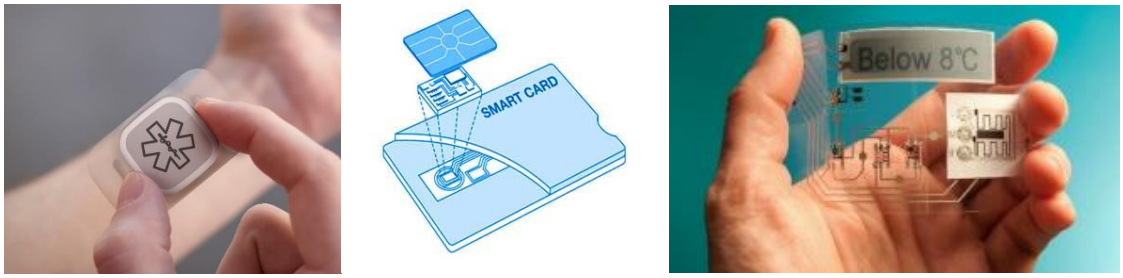

Figure 1. Examples of devices requiring flexible or conformable batteries (adapted from [4-6]*), from left to right: miniaturized, wearable medical device, smart card with implanted microprocessor, smart packaging powered by a paper-based battery*

Supercapacitors and batteries are both energy storage devices that have been developed in flexible forms in research and even sold on the market, showing great promise for powering IoT devices and other flexible and wearable technologies. Compared to supercapacitors, batteries have a very high capacity due to the energy storage mechanism being of an electrochemical reaction in nature, which typically exceeds the achievable capacity found in electric double layer capacitors (EDLCs), also known as supercapacitors, by over an order of magnitude. However, the

energy stored as an electrochemical reaction also imply a lower reversibility due to side reactions that consume active material contributing to a battery's capacity fade. Additionally, electrochemical reactions tend to be more sluggish in nature in comparison to the formation of an electric double layer. [7] Nonetheless, for the purpose of typical flexible devices, possessing a higher capacity is generally more desirable than having a higher power output as these devices are designed to consume smaller amounts of energy over a longer period of time. Some of the typical energy needs can be found in Table 1.

Table 1. Energy needs of flexible devices and IoT devices (adapted from [8]*)*

IoT, MEMS, CMOS memories, Medical implantable	**Smart cards, Skin patch, RFID**	**Wearables, E-textile, Medical device**
Capacity Range		
1 mAh	10 mAh	100 mAh
Important Features		
• Rechargeable • Small footprint, many micro-batteries • Long life time • Rapid discharge • Tend to incorporate with energy harvesting	• Can be both disposable and rechargeable • Laminar and thin, some with special form factor • Relatively low power • Cost sensitive	• High energy density for small volume • Long working hours • Flexible, stretchable or thin, some with special form factor
Technology Status		
Small volume production	Available, mostly customized	Prototypes available

Unfortunately, most flexible batteries store less energy than the traditional non-flexible coin, cylindrical or prismatic battery architectures as they are effectively thin film batteries with lower ratios of active material to inactive material in order to impart more flexibility to the battery. Various methods have been used to make flexible and miniature batteries and energy storage devices. Microfabrication techniques such as micro-patterning using scaffolds and etching has been used to prepare three-dimensional interdigitated structures for electrodes [9]. For the

deposition of very thin-films of active material onto electrodes, chemical vapour deposition (CVD) and radio frequency (RF) magnetron sputtering is also applied [10]. However, both of these methods come at the expense of high processing costs and require complex fabrication. Furthermore, the final device is either inflexible or not inherently flexible, which requires the addition of thicker packaging layers in order to offer flexibility to the final device. Simpler, less expensive techniques involve casting methods where slurries of active material are used with conductive and elastomeric binders [11]. Printable carbon-based inks using graphene or carbon nanotubes can also be prepared for the ink-jet printing of microsupercapacitors. Ink-jet printing of these storage devices has been reported on various substrates as well, but binders and sintering are often required in order to allow for higher conductivity of the traces [12,13].

Recently, there have been a number of reports on utilizing laser-scribing as a simple method to prepare energy storage devices from substrates such as graphene oxide (GO) and commercial polymers like polyimide (PI). El-Kady et al. [14] found that graphene could be induced from the laser of a computerized DVD drive on a GO film. However, the stability of GO presents a challenge in further developing the technology. Alternatively, the thermal energy from a CO_2 laser has been shown capable of forming a porous graphene network from PI [15]. Furthermore, the interdigitated electrodes that could be laser-patterned on the PI demonstrated the possibility of electrodepositing active material such as polyaniline (PANI), MnO_2 and FeOOH for the fabrication of pseudocapacitive microsupercapacitors, which store energy through the charging of the double-layer as well as charge transfer between the electrode and electrolyte [16].

Despite their high power density, the energy density of supercapacitors is still rather low, as previously mentioned, and thus it is more lucrative to develop a flexible, thin-film battery with a much higher energy density at a fraction of the production cost of current methods like CVD or microfabrication techniques. Of the next-generation battery chemistries available beyond the widely commercialized Li-ion batteries, one of the most promising is considered to be the lithium-sulfur (LiS) battery chemistry. The LiS chemistry with a sulfur cathode and lithium metal anode with theoretical capacities of 1672 mAh/g and 3860 mAh/g, respectively, promises a combined energy density of 2567 Wh/kg [17], which is several fold higher than current state-of-the-art Li-

ion batteries. Other benefits to the LiS chemistry include the low densities of both sulfur and lithium metal, allowing them to achieve higher energy densities at a lower weight, ideal for electric vehicles and other applications. Sulfur is also significantly more abundant and cost effective as a cathode material than many of the transition metal oxides used in Li-ion cathodes, fitting for use in some of the smaller electronic devices meant to be somewhat more disposable found in Table 1. Moreover, the high cost and controversial labour practices in mining cobalt [18], which is a major component of many Li-ion battery cathodes, further motivates the movement toward sulfur cathodes.

By coupling the facile and rapid patterning of flexible electrodes on commercially available polymer substrates with the promising high energy density and benefits of the LiS chemistry, flexible, thin-film batteries can be manufactured at an unprecedented simplicity while being cost effective and possessing higher capacity for emerging technologies. And since Li et al. proved the possibility of using these laser-induced graphene (LIG) electrodes for pseudocapacitive supercapacitors, it is believed that the same electrodes could also be used for the fabrication of flexible batteries that can be easily manufactured, unlike most reports of techniques requiring high capital cost equipment.

At the start of this thesis, there were no methods to selectively deposit sulfur onto a patterned electrode. Most methods of introducing sulfur into a conductive host involves the grinding of the insulating sulfur with the conductive material (e.g. graphene, carbon nanotubes, activated carbon, etc.), followed by melt imbibition [19]. Afterwards, the sulfur and conductive material would be pressed or cast onto a current collector to form the cathode of the cell. However, this is not an applicable method with an electrode that is already formed prior to the introduction of the active material components. Sulfur is electrically insulating and thus is not readily electrodeposited, although such a method has recently been developed [20]. Secondly, most LiS batteries reported use bulk Li metal anodes and there is little to no work on lithium electrodeposition onto LIG or other substrates. There are a number of challenges with utilizing Li metal anodes which will be presented later. But while many reports suggest a variety of methods to improve Li plating and stripping from bulk Li metal electrodes, there are no reports that

examine the cycling and plating of electrodeposited Li on foreign substrates. A study and understanding of such behaviour would be necessary in order to move towards the minimization of the amount of Li used in a battery system to reduce costs and conserve Li resources. Lastly, the LiS battery is an immature technology and suffers from several degradation mechanisms that consequently inhibit their commercialization. Accordingly, the best-practices presented in literature will need to be incorporated in the flexible LiS battery to achieve high capacity and cycle stability. It is also with the hope that utilizing an interdigitated system for the LiS battery will allow the *in operando* characterization and study of the LiS failure mechanisms in a system with near stoichiometric lithium.

1.2 Objectives

The primary objective for this thesis is to develop a proof-of-concept flexible and interdigitated LiS battery systems based on LIG electrodes as a result of the highly attractive motivators presented earlier. Fabricating LiS batteries using LIG will involve the development of methods and techniques for selective deposition of the active materials, lithium and sulfur, into the opposite-polarity interdigitated electrodes. Additionally, it will also require a deeper understanding of the nature and structure of LIG for its stability in its use for electrochemical devices as well as the efficiency of Li plating on different types of carbon to understand what carbon host and electrolyte would be ideal for Li metal anodes.

The specific objectives for this thesis include the following:

1. **Development of an appropriate method for the introduction of elemental sulfur into the cathode of the LIG battery.** Sulfur cannot be easily electroplated due to its insulating nature. Additionally, traditional methods of grinding the insulating sulfur with a conductive host is nonapplicable to LIG electrode fingers due to the fingers already having been formed through direct writing by the laser. Thus, a novel technique will be required to introduce sulfur.

2. **Enhance lithium electrodeposition into a porous conductive carbon host, namely, LIG.** Lithium, on the other hand, can be electrodeposited at the anode fingers in a relatively simple manner. However, lithium metal has been known to irreversibly react with electrolyte and other materials, leading to low plating efficiencies and mossy morphologies, posing great challenges to efficient and uniform plating of the metal on a porous host and a current collector such as LIG.
3. **Determine the effect of various laser parameters on crystallinity, defectiveness, porosity and conductivity on the formed LIG film.** There is very little that is known about the structure of PI-derived LIG, including the size of crystalline regions or the presence of amorphous-sp^3 regions vs true sp^2 regions. However, understanding how to control such properties through the variation of laser parameters is crucial to better exploiting LIG for electrochemical and electronic devices.
4. **Study the efficiency of Li electrodeposition on various carbon materials in various electrolytes.** Bulk Li metal as the anode is highly unstable and most published work utilize a gross excess of Li metal to compensate for its reactivity and loss over cycling. However, this is obviously undesirable and carbon hosts have been used for encapsulating Li due to their highly conductive and lightweight nature. As electroplating is a simple and common method for introducing Li metal, it is important to understand the plating efficiency of Li on different types of carbon and in different types of electrolyte to maximize efficiency and stability.

1.3 Outline of Thesis

This thesis covers the development of a flexible LiS battery based on a LIG material derived from PI as well as two very important aspects that are crucial to the fabrication of this device: 1) control over and characteristics of the LIG formed and 2) lithium electrodeposition onto carbonaceous materials. At the beginning of each chapter, an introduction pertaining to more specific background and fundamental details for the topic is provided preceding the experimental and results sections.

Chapter 2 is an extensive chapter on the specific details of the design, fabrication, characterization and testing of the battery. The chapter first begins with the characterization of the LIG electrodes, proceeded by the introduction of sulfur into these LIG electrodes and a more thorough analysis of the distribution of sulfur within the pores. The introduction of lithium through electrodeposition follows and various samples studied are presented in the argument for the final protocol of using silver nanoparticles and a reverse pulse plating technique. Lastly, the device is tested both as a full cell, a Li-Li symmetric cell and a coin cell, leading to the conclusions that there are limitations with the pore structure, sulfur deposition technique as well as the electrodeposited Li metal.

The conclusions from Chapter 2 motivate the need to better understand how to adjust and tune specific characteristics of LIG through the laser power, number of laser passes and defocusing, which form Chapter 3. Various characterization techniques are applied in order to understand the defectiveness and crystallinity within the LIG as a function of the different laser parameters used to induce the graphene.

Furthermore, the need to study Li plating on soft and hard carbons in different electrolytes are also prompted by the findings in Chapter 2, which constitute Chapter 4. Graphite, a hard carbon and copper are used as Li plating substrates in ether-based and carbonate-based electrolytes with two different Li metal salts. A thorough analysis of the plating and stripping efficiencies and electrochemical impedance spectra is conducted in order to gain a better idea of the carbon-solvent-salt interactions. Based on the results, a mechanism is proposed to explain some of the more intriguing discoveries.

Finally, Chapter 5 concludes the work from this thesis and offers suggestions for further work on specific aspects of the flexible battery and direction of future research.

2.0 Fabrication of Lithium-Sulfur Flexible Battery

2.1 Background

2.1.1 Types of Energy Devices Available

Now more than ever before, flexible energy storage devices are needed to progress alongside the evolving technology in society. For the target applications, there are typically three types of available options for miniature and flexible energy devices: 1) energy harvesting, 2) supercapacitors and 3) batteries. Each of these have distinctly different forms of energy storage mechanisms as well as different properties that may make them more appealing for a certain application over another.

Within energy harvesting devices, there are various types as well, such as triboelectric generators, thermoelectric generators and piezoelectric generators (Figure 2). Benefits of using energy harvesting devices is that the energy obtained from these sources would otherwise be considered as "wasted" energy, due to their losses in the form of heat or friction. Thus, it is highly attractive to use energy harvesting as a means for producing energy to power small electronics and devices that are very portable and perhaps do not require a lot of energy such as implantable biomedical devices. In particular, methods of efficiently harvesting energy from the human body would render the electronics as self-powering in that no other sources of energy would be necessary to charge them.

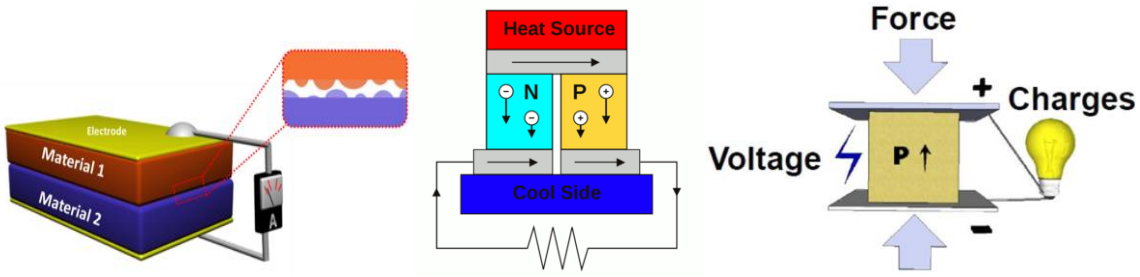

Figure 2. Schematic of the three common types of energy harvesting devices (left to right): triboelectric, thermoelectric and piezoelectric [21–23]

Despite the convenience and simplicity of such energy harvesters, in the end, they are only energy harvesters and not capable of storing the energy that is collected. Thus, true energy storage devices such as supercapacitors and batteries are required and can be coupled with the generators for a full, self-powering, high capacity energy harvesting and storage system. Additionally, many of the methods for preparing the materials required to enhance the energy harvesting method of the generators require more expensive or complicated techniques, such as the preparation of doped polymers into films or microfabricated pattern gratings [24].

Supercapacitors and batteries are both energy storage devices that have been developed in flexible forms in research and even sold on the market, showing great promise for powering IoT devices and other flexible and wearable technologies. Supercapacitors typically have a very high power density due to the energy storage mechanism being purely physical in the adsorption of ions to the electrode surface in EDLC based supercapacitors. Moreover, the highly reversible energy storage mechanism in these supercapacitors allow them to charge and discharge for thousands of cycles. Yet, the capacitance of EDLC supercapacitors is proportional to the surface area of the electrode used and thus, in order to maximize a supercapacitor's capacity, a very high surface area electrode must be used. Typically, these electrode materials are expensive to synthesize and keep stable in the electrode (prevention of aggregation) upon cycling. [7]

Researchers have found ways to fabricate thinner and more flexible supercapacitors, often dubbed microsupercapacitors. In 2007, Pushparaj et al. discovered a way of utilizing ionic liquid and unmodified cellulose to cast onto a film of multi-walled carbon nanotubes (CNT) to form a thin paper nanocomposite that can be used as the electrode of a supercapacitor [25]. They had also proposed to use it as a battery, mimicking the graphite-Li battery. Others have also used paper as a substrate for supercapacitors due to cellulose's inherent flexibility as well as the availability and convenience of paper [26–29]. However, as paper has a tendency to degrade as a result of cellulose's hydrophilicity, other options for flexible supercapacitors have also been explored. Furthermore, even simpler methods of fabrication as well as using direct patterning of interdigitated electrodes became desirable for faster prototyping in industry.

El-Kady et al. were the first to look into using the direct laser writing (DLW) of GO films to selectively reduce GO, forming conductive reduced graphene oxide (rGO) traces that can become free standing, flexible supercapacitors [14]. Graphene is very attractive as an electrode material due to its high surface area and carrier mobility. However, the typical indirect chemical synthesis of graphene through GO, which can be reduced to form rGO, is a long procedure with many harsh chemicals. In this indirect synthesis procedure, the graphene formed is often laden with defects and crinkled due to the destruction of the graphitic lattice upon oxidation and subsequent removal of the functional groups to form rGO. A few years later, Lin et al. found that by using a commercial CO_2 laser, porous graphene films could actually be induced by DLW from a commercial polymer known as Kapton©, or PI [15]. This allowed for the possibility of utilizing the polymer as both a substrate and a precursor for the electrodes as well as a very facile method of fabricating roll-to-roll EDLC supercapacitors.

Even with the advancements in preparing flexible supercapacitors, ultimately, supercapacitors still have a lower energy density, causing them to be less effective in particular applications in comparison to batteries which are capable of storing much more energy per volume or weight.

2.1.2 Flexible, Thin-Film Batteries

As batteries are much more complex than EDLC supercapacitors, their fabrication techniques and operations also tend to be more intricate. The formation of thin-film, flexible batteries can be made in a number of different methods and architectures. The two most common form factors are thin-film sandwiches and interdigitated electrodes. Most sandwich-form thin-film batteries are fabricated from blade coating an electrode slurry to a current collector [11,30,31], screen-printed [30,32] or by CVD and sputtering [10,33,34] of various battery materials and layers. Blade coating and screen printing have been shown to be effective and scalable methods for batch processing, where the former is also capable of producing roll-to-roll (R2R) films of electrode

material, while CVD and sputtering techniques are currently limited in industry due to the high operational and manufacturing costs.

While blade coating [35], screen printing and sputtering are methods that can also be used to fabricate interdigitated batteries, other techniques are available too, such as atomic layer deposition (ALD) [36] or nanotemplating [9], as examples of microfabrication methods. Yet printed electronics and direct-writing techniques are becoming more popular due to the ease and scalability of these methods. Batteries can be 3D-printed [37,38] and ink-jet printed [30] in any desirable configuration as well, after the development of suitable formulations that maintain the electrical contact of all components after drying. One of the challenges with using slurries, 3D-printing inks or inkjet-compatible inks is the necessity of using a high binder and conductive additive content in order to ensure the contact of electrode components with the bending and unbending of the battery. However, this also reduces the energy density of the final device. Thus, it is attractive to pursue systems that mitigate the need for binders and additional conductive additives altogether. This can be made possible in the DLW of 3D porous graphene films, as introduced by the Tour group [15], which creates highly versatile electrodes for any kind of flexible electronics.

2.1.3 Traditional, Non-Flexible Lithium Sulfur Batteries

There have been many reports of flexible Li-ion batteries in literature but generally, due to the nature of flexible cells, a higher portion of inactive components would be required in order to compensate for some stresses present in the cells during flexing and bending. As a result, the energy density of such batteries would be much lower than their non-flexible counterparts. It is for this reason that it would be of interest to explore higher energy density battery chemistries for use in such flexible batteries, such as the LiS battery chemistry.

The LiS battery chemistry promises a significant improvement in energy density over the highly commercialized Li-ion batteries due to the low density of lithium and sulfur as active materials. This is to be compared to the metal oxides and graphite used as Li-ion hosts in Li-ion

batteries. Most Li-ion batteries can reach a maximum of about 100-200 mAh/g theoretical capacity (depending on the cathode material) [39], while the sulfur cathode in LiS batteries have a theoretical capacity of 1672 mAh/g, based on the redox reactions of Li with the elemental S. While this only attests to the capacity improvement of the LiS chemistry, the low density of sulfur and lithium yields energy densities of 2500 Wh/kg, a several fold increase in energy density over Li-ion batteries [40]. This makes LiS batteries significantly more desirable especially for applications concerning transportation and other load-critical applications.

Despite the attractiveness of the LiS chemistry, so far, there have been only about two commercialized LiS batteries on the market, one by Sion Power© called the Licerion® and one by OXIS Energy. The slow commercialization of LiS batteries is due to a number of challenges that LiS batteries experience that are critical to their long-term stability and capacity retention as well as safe operation (summarized in Figure 3). The first challenge in designing LiS batteries is the fact that both the initial elemental sulfur and final discharge products Li_2S_2/Li_2S are all electronically insulating. As a result, it is not possible for sulfur to be used on its own as a cathode material, but it must be distributed within a conducting matrix, of which the conductive host must also be engineered to minimize its weight and volume so as to not diminish the increased energy density with the LiS chemistry. [40,41]

Another challenge is the shuttling phenomenon where highly soluble intermediate sulfide species, called lithium polysulfide species (LiPSS), have a tendency to migrate away from the cathode due to a concentration gradient formed within the cell. This results in a loss of active material and capacity fade. Additionally, during the charging of the device, the shuttle phenomenon leads to "infinite" charging which takes place when longer chain LiPSS migrate away from the cathode towards the anode and become reduced to shorter chain LiPSS there. The shorter chain LiPSS migrate back towards the cathode and once again become oxidized to longer chain LiPSS and the cycle begins again. Typically, the shuttle phenomenon can be mitigated by using electrolytes that have a lower solubility for these LiPSS, but some degree of solubility is required for the redox reactions to occur. Some other solutions have been to use either physical

entrapment or covalent interactions with these LiPSS, which can prevent their migration from the cathode. [40,41]

While the electrolyte must be stable to enable the redox reactions of sulfur with lithium ions, the electrolyte must also be inert towards the active material but also capable of forming a stable solid electrolyte interphase (SEI) upon its decomposition at the electrodes. SEI is a layer of electrolyte decomposition/side reaction products at the electrode. During SEI formation, it results in a lower cycling efficiency. But once stable, SEI is also helpful in preventing further side reactions at the electrode. This is particularly critical at the negative electrode which is typically metallic lithium. Lithium is highly reactive, forming SEI with the non-aqueous electrolyte upon contact, but its highly reactive nature also results in a porous, mossy structure upon many plating cycles due to the effectively infinite volume change of a metal anode where Li is completely stripped and completely re-plated during each cycle. As such, a more extensive SEI layer forms with the increase in surface area and porosity of the Li anode. This slows down the diffusion of Li-ions in and out of the anode in addition to irreversibly consuming electrolyte. Uneven deposition of Li metal at moderate charging rates also results in dendrite formation during plating, which can lead to the puncturing of the separator membrane, resulting in short circuits and cell failure. [40,42,43] More of the challenges pertaining to Li metal anodes will be discussed in greater detail (Section 4.1).

Though there are many challenges, there have also been many great efforts published in literature to mitigate these challenges, making LiS batteries safer to operate and closer to wide-spread commercialization. It is with the challenges of traditional LiS batteries in mind that the flexible LiS battery is designed as presented in this work.

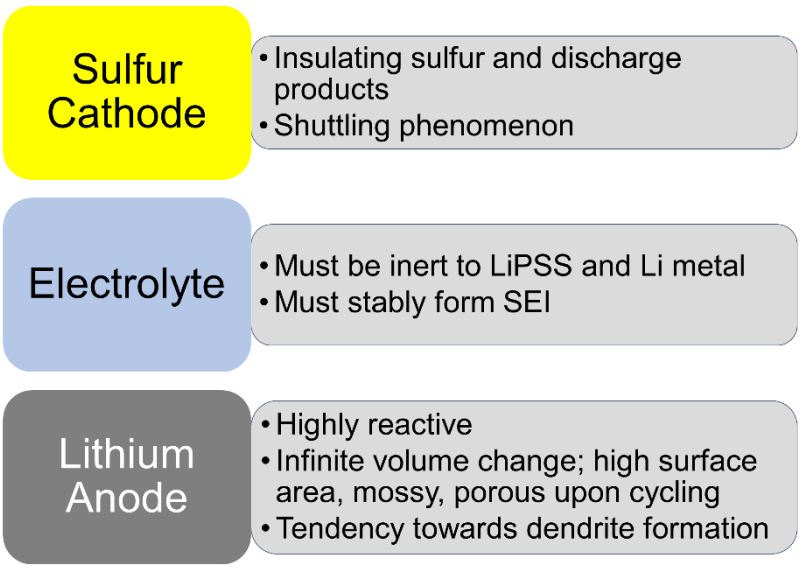

Figure 3. Summary of main challenges with traditional, non-flexible LiS batteries

2.2 Design of Device

Laser-scribing as an approach for the simple and cost-effective production of such flexible energy storage devices is very promising and was thus considered for the fabrication of the flexible batteries presented in this thesis. Thus far, batteries have not been made using this laser-scribing technique. It is possible that this is due to the challenge of the insulating nature of most cathode materials (e.g. Li metal oxides for Li-ion batteries, sulfur for LiS batteries) as well as the difficulty of selectively depositing the material onto the electrodes themselves. As a result, more complicated cleanroom techniques would typically need to be used. However, it is possible to utilize a simple approach to create interdigitated LiS batteries using the laser induction method (Figure 4). First, a simple, commercial laser engraving machine (i.e., CO_2 laser) was used to pattern conductive, flexible, high surface area graphene traces on top/within a commercial PI film. Next, sulfur is selectively deposited onto these traces by exposing electrodes to a bath of saturated sulfur in dimethyl sulfoxide (DMSO) in order to heterogeneously nucleate sulfur onto the LIG by lowering sulfur's solubility in a cooled, saturated solution. Repeating this procedure enabled control of the sulfur loading up to 3 mg/cm^2 or higher, which is near the optimal loading

for high energy density large format devices [17]. While this sulfur deposited as micron-sized crystals, it was found that brief heating beyond the melting point of sulfur allowed for melt imbibition into the laser-patterned pore network. In a second step, the anode was scribed onto the film by the same laser induction method. As lithium has a high nucleation energy on a number of materials, including carbon, silver nanoparticles (Ag NP), which were found to alloy with lithium to reduce the plating overpotential, were introduced [44]. The Ag NP act as a means to seed the growth of lithium during its electrodeposition onto the anode, resulting in smoother plating morphologies. Additionally, since lithium has a tendency to form dendritic morphologies at high plating currents, a reverse pulse plating technique was used, which, when combined with the Ag NP seeds, produced denser lithium films on the LIG electrodes. A room temperature ionic liquid (RTIL) is used as the cycling electrolyte, which is known to be thermally and chemically stable while also providing safety due to its non-flammability. This allows the device then to be suitable in flexible systems to be used in IoT devices and other related applications.

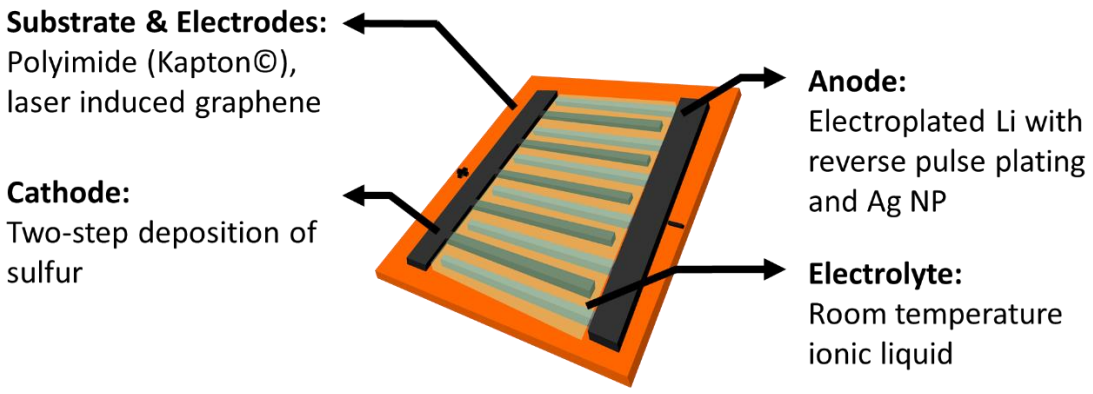

Figure 4. Schematic of design for lithium sulfur flexible battery

2.3 Method and Characterization

2.3.1 LIG Electrodes

The method of creating LIG on PI as published by the Tour group [15] was adopted in the preparation of the electrodes for the flexible battery. Kapton© (HN polyimide) film with a thickness of 127 μm was purchased from McMaster-Carr to be used as the substrate and source

of carbonizable material for the electrodes. The PI film was used as is without modification and a CO_2 laser system (Boss Laser LS1416, 50W) was used for the laser-patterning of the electrodes. The interdigitated pattern of the electrodes can be seen in Figure 5a) where the red area corresponds to the cathode of the battery and the blue area corresponds to the anode of the battery. After the induction of the porous graphene network, the width of each finger is found to be around 315 μm and 175 μm for the cathode and anode (prior to Li plating) fingers, respectively, with the separating distance between each adjacent finger of opposite polarity to be around 310 μm (prior to Li plating). The overlapping distance between the sets of fingers for each polarity is 1.2 cm. The design was explicitly chosen such that the anode fingers would be thinner in order that more Li metal can be plated onto the LIG without short circuiting the final device.

The two sets of electrodes are scribed separately, with the cathode first and then the anode, as will be further described later. Figure 5b) shows the sample after the laser-scribing of the PI film. A scan speed of 30 mm/s and 10% power (5W) were used in x-direction, bilateral raster scanning mode for the patterning of the interdigitated electrodes and the pattern was lased onto the PI twice (i.e. number of laser passes = 2). These LIG electrodes were used as the conductive network for the deposition of the active material in both the anode and cathode of the flexible battery.

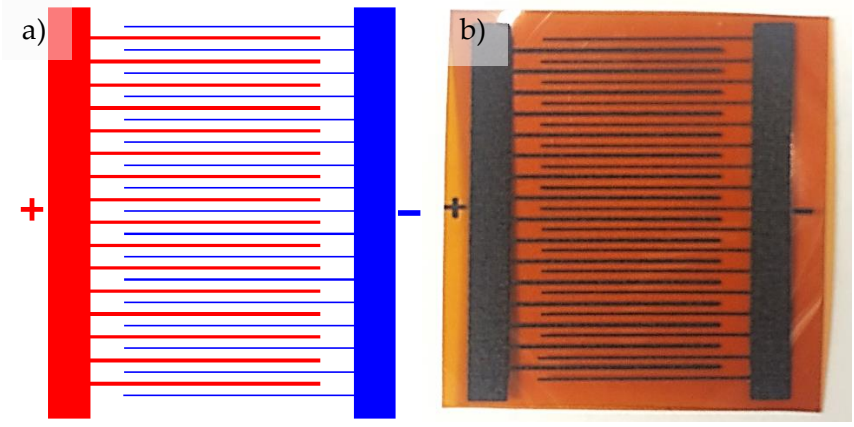

Figure 5. a) Laser-scribing pattern of device on computer software for laser and b) digital image of completed device after scribing

2.3.2 Sulfur Deposition into LIG

Sulfur crystals can be heterogeneously nucleated onto the surface of the LIG electrodes through a reduction in the solubility of sulfur by the cooling of a saturated solution of sulfur (purum p.a., >= 99.5%, from Sigma Aldrich) in DMSO (>= 99.7%, Fisher Scientific) with a concentration of 40 mg/mL. This solution was heated up to 180°C in order to dissolve the sulfur in the DMSO under stirring. The sample is placed with the electrodes facing down on a petri dish and weighed down by a glass slide in the petri dish, which are all preheated to 130°C on a hot plate. The heat is shut off on the hot plate after 750 μL of the hot S/DMSO solution was injected between the sample and the petri dish and sample were cooled on the hot plate for 15 mins. The sample was then gently but thoroughly rinsed with deionized water to remove any excess S/DMSO solution and dried at 110°C for 15 mins in air. A noticeable change in colour of the electrodes was found as the water evaporated from the sample. The electrodes were now a grey colour, with sulfur crystals that were detected by the naked eye due to the light that reflected off the crystals. The sample was flash heated at 165°C, the temperature at which sulfur possesses its lowest viscosity [19], on the hot plate for only a few seconds until the sulfur crystals had disappeared and melted into the electrode. The colour of the electrode was now almost black, just slightly lighter in colour than after scribing, but no more sulfur crystals could be detected by the eye.

For multiple sulfur depositions in order to obtain higher loadings, the same process (Figure 6) was repeated from 2-4 depositions.

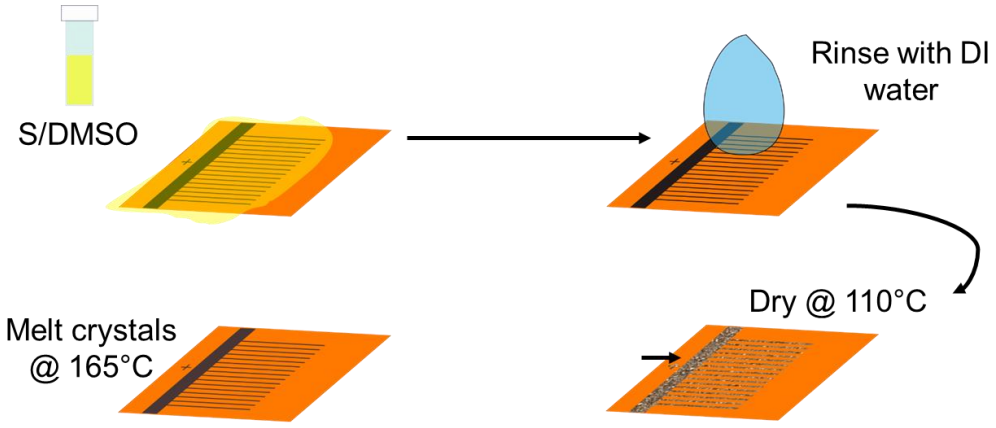

Figure 6. Schematic illustrating the sulfur deposition procedure which was repeated for increasing the sulfur loading as necessary

2.3.3 Lithium Electrodeposition into LIG

Following the sulfur deposition to a desired loading, the anode of the battery was patterned (blue area only of Figure 5). The device is then taken into an argon-filled glove box. For the electroplating of lithium onto the anode of the battery, the set up in Figure 7 was used, where the distance between the counter electrode (CE) and working electrode (WE) is 3 cm. A piece of lithium ribbon (length x width = 5 x 4 cm, thickness of ~0.75 mm, Sigma Aldrich) was used as a counter electrode and the working electrode is the anode of the sample itself. Both of these are contacted with a piece of brass (Ultra-Formable 260 Brass Sheet purchased from McMaster-Carr) while set 3 cm apart in a glass holder in a bath of the plating electrolyte composed of 1M lithium perchlorate ($LiClO_4$, 99+%, Acros Organics) in 1:1 ethylene carbonate (EC, anhydrous 99%, Sigma Aldrich)/dimethyl carbonate (DMC, anhydrous >= 99%, Sigma Aldrich), and used as is.

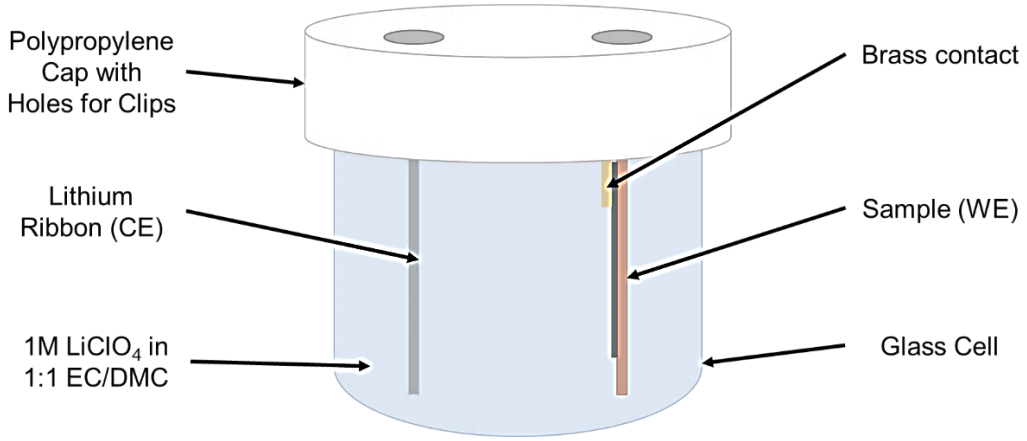

Figure 7. Diagram for the side view of lithium plating set up

Colloidal silver nanoparticles (Ag NP) were synthesized from $AgNO_3$ and reduced by sodium citrate as described by Ratyakshi [45]. The entire laser-scribed sample is submerged in a bath of ethanol for 10 mins in order to wet and displace the air from the porous hydrophobic LIG network Afterwards, the sample is submerged into the aqueous bath of the Ag NP for 10 mins which solvent exchanges the Ag NP dispersion with the ethanol. The sample is then heated on a hot plate at 110°C to remove all water from the sample.

Both direct current (DC) and a reverse pulse plating (RPP) techniques were applied to electrodeposit lithium onto the LIG. For using RPP, according to Chandrasekar et al. [46], the specific cathodic and anodic currents and times must be chosen with the consideration of the duty cycle as well as the amount of time required to charge the electrical double layer on each of the pulses. For the RPP technique, the average current density, I_A, is defined as:

$$I_A = \frac{I_C T_C - I_{AA} T_{AA}}{T_{AA} + T_C} \quad (1)$$

Where I_C is the forward, cathodic current and T_C is the length of the cathodic current pulse in time, I_{AA} is the reverse, anodic current and T_{AA} is the length of the anodic current pulse in time. Table 2 indicates the specific parameters used for lithium plating with the RPP technique, based on a study that was conducted by Yang et al. [47] in 2014 to determine the effects of various parameters on the morphology of plated lithium as well as the cycling efficiency of Li/Li symmetric cells. The values as listed in Table 2 yielded the most compact morphology while also

giving the highest cycling efficiency, indicative of the lowest rate of loss of lithium due to reactions with the electrolyte or dendrites that form and break off.

Table 2. Lithium plating parameters chosen for the RPP technique based on [47]

Parameter	Value
Cathodic current, I_C (mA/cm^2)	1
Cathodic current pulse length, T_C (ms)	5000
Anodic current, I_{AA} (mA/cm^2)	10
Anodic current pulse length, T_{AA} (ms)	20

Due to the nature of lithium being consumed in the process of creating the passivating SEI layer, it is recommended to always use an excess of lithium to mitigate the loss of lithium. A stoichiometric ratio of 1:2.5 for S/Li was chosen for determining the lithium loading into the anode fingers.

2.3.4 LIG-Based Full Cell

After Li electrodeposition, the samples were rinsed with 1:1 EC/DMC without the $LiClO_4$ salt to remove all traces of excess salt. Then the samples were fully dried by vacuum in order to remove excess solvent. As carbonate solvents are incompatible with the sulfur cathode due to the reactivity of lower-order polysulfides with the carbonate molecules [48], it is crucial to completely remove the carbonate solvent that was previously utilized for lithium electrodeposition. For the cycling of the cells, a RTIL-based electrolyte was chosen due to the non-volatility, high chemical and temperature stability as well as its low solubility for polysulfides, preventing its migration towards the anode leading to capacity fade. Specifically, 1M lithium bis(trifluoromethylsulfonylimide) (LiTFSI, 99.95%, Sigma Aldrich) in 1-ethyl-3-methylimidazolium bis(trifluoromethylsulfonylimide) (EMImTFSI, 99%, IoLiTec) was chosen as the cycling electrolyte. LiTFSI has been shown to form stable SEI decomposition products that

help stabilize the Li anode [49]. The cycling setup used in this study is shown in Figure 8, where the busbars of the device are contacted by copper foil, and the electrolyte and contacts are pressed against the cell by the use of glass plates held together using external clips.

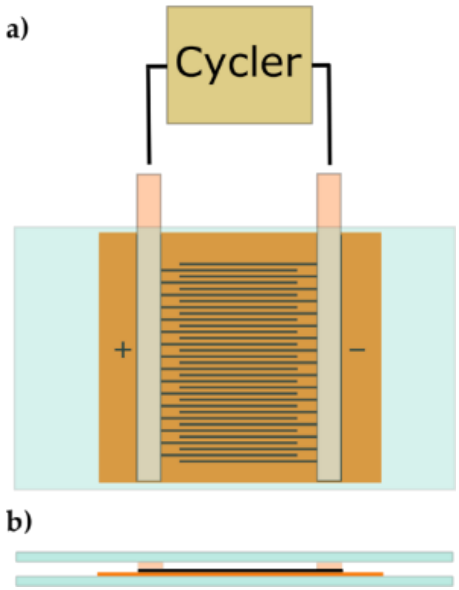

Figure 8. Cycling setup of the flexible LiS batteries with where a) is the top view and b) is the side view. The device is contacted by copper contacts at the busbars and held together by clips to contain the cycling electrolyte

2.3.5 Li vs Li Symmetric Cell

As most of the capacity loss can be elucidated by the consumption of Li through SEI formation during the first cycle, it was of interest to conduct a Li versus Li test on the LIG fingers where Li is electrodeposited on both sets of fingers at an equivalent capacity and cycled. In this study, both sets of LIG fingers contained a film of plated Li (by RPP seeded by Ag NP), plated to a capacity of 1.874 mAh on both (equivalent to 1.0x stoichiometric lithium to the sulfur loading of 3.9 mg/cm^2). This capacity was chosen so as to avoid short circuiting of the cell after both sets of electrodes were electrodeposited with Li. After Li was introduced to both electrodes, the sample was rinsed with solvent as described in Section 2.3.4 and dried prior to cycling in the

cycling electrolyte of 1M LiTFSI in EMImTFSI. The same cycling setup described in Figure 8 was used for the cycling of the cell.

2.3.6 S/LIG v. Li Full Cell

The S/LIG material was scraped off of the PI substrate after four cycles of the nucleation-imbibition technique and it was confirmed by TGA that the final weight percentage of sulfur was around 70%. The material was then pressed into an electrode (1/2" diameter) onto an Al foil current collector (as is conventional for sandwich cells) with a very low pressure, only sufficient enough to form a very thin pellet with an areal loading of 3.9 mg/cm^2. The cathode was then transferred into an Ar filled glovebox and used to make a CR2032 coin cell. The coin cell components comprise of a stainless-steel cathode pan, cathode (as described), glass fiber membrane (pore size of 2.7 μm, thickness of 160 μm, Sigma Aldrich), Li foil, stainless steel spacer, stainless steel spring, 100 μL of electrolyte and stainless steel anode cap with a Teflon O-ring. The coin cell was assembled entirely within the Ar glovebox with water and oxygen levels below 1.0 ppm, and the cell was pressed at 1000 psi. For comparison, two electrolytes were tested: 1M LiTFSI in 1:1 (v/v) 1,3-dioxolane (DOL, anhydrous 99.8%, with ~75 ppm BHT as inhibitor, Sigma Aldrich)/1,2-dimethoxyethane (DME, anhydrous 99.5%, Sigma Aldrich) and the RTIL-based electrolyte used previously, 1M LiTFSI in EMImTFSI. The ether-based electrolyte was chosen for comparison as it is a more commonly used electrolyte for LiS systems. After assembly, the cells were taken out of the glovebox for cycling between 1.5 V and 3 V at 0.1C.

2.3.7 Material Characterization

The pore structure of the laser scribed material was characterized through scanning electron microscopy (SEM, FEI Quanta FEG 250 ESEM with energy dispersive x-ray spectroscopy (EDX)) at an acceleration voltage of 20kV and surface area measurements were conducted using a DVS Advantage Surface Measurement System, between partial pressures of P/P_0 = 0-0.5 using ethanol as the adsorbate. The LIG was scraped off the PI substrate using a scoopula and then the mass

and surface area was measured by the surface measurement system equipped with a microbalance. Mass measurements in the surface measurement system were taken after having tared the microbalance and dry air flowed over the sample for at least 30 min.

While the surface area measurements yielded the pore size distribution, further BET analysis on the linear region of the isotherm corresponding to multi-layer coverage yielded the following linear fit of the form $y = mx + b$:

$$\frac{P/P_o}{V_{ad}\left(1-P/P_o\right)} = \frac{C-1}{CV_{ad,mon}}\left(P/P_o\right) + \frac{1}{CV_{ad,mon}} \rightarrow y = 2.84635 \cdot 10^{-2}x - 4.74421 \cdot 10^{-4}, \quad (2)$$

where P/P_o is the partial pressure, V_{ad} is the volume of adsorbate (ethanol in this case), C is the BET constant, $V_{ad,mon}$ is the monolayer volume of adsorbate which can be calculated to yield the surface area of the LIG material.

To understand confirm the presence of graphene and sp^2 regions within the LIG, Raman analysis was conducted by a Horiba Jobin-Yvon HR800 Raman system equipped with an Olympus BX 41 microscope with a 532 nm laser at 50% laser power (of the 50mW total laser power). The following empirically derived equation is used for the estimation of the number of graphene layers [50]:

$$\omega_G = 1581.6 + \frac{11}{1+n^{1.6}} \quad (3)$$

where ω_G is the position of the G peak and n is the number of graphene layers.

The crystallite size can be estimated through the following equation [51]:

$$L_a = 2.4 \times 10^{-10}\lambda^4 \frac{I_D}{I_G} \quad (4)$$

where L_a is the crystallite size of the graphenic domain and λ is the wavelength of the laser used, 532 nm, in this case. This is under the assumption that in the variation of I_D/I_G with L_a, the LIG lies within the regime of nanocrystalline graphite as opposed to the regime of amorphous carbon as described in [52].

For the determination of sulfur and Ag NP wt%, thermal gravimetric analysis (TGA, TA Instruments Q500) was conducted. For TGA, it is expected that for the samples, there would only be LIG, absorbed atmospheric water and sulfur or Ag NP. Other chemicals involved in the procedures should have been properly rinsed off and all interactions between the LIG, water and sulfur/Ag NP are purely physical. Thus, TGA is an appropriate analysis to carry out to determine the elemental gravimetric composition of the samples, specifically sulfur and silver, through the decomposition of sulfur in N_2 gas or LIG in air (to determine the remaining silver). TGA was carried out from 25°C – 800°C at a ramp rate of 10°C/min and the samples were held at 100°C for 30 min prior to further temperature increase in order to remove excess water. Sulfur/LIG samples were conducted under nitrogen gas while Ag NP/LIG samples were conducted in air. The weight fraction of sulfur was determined through the following formula:

$$wt\%\ of\ S = \frac{wt\%\ remaining\ at\ 100°C - wt\%\ remaining\ at\ 800°C}{wt\%\ remaining\ at\ 100°C} - wt\%\ loss\ of\ LIG\ in\ N_2 \qquad (5)$$

And for the Ag NP content:

$$wt\%\ of\ Ag\ NP = \frac{wt\%\ remaining\ at\ 800°C}{wt\%\ remaining\ at\ 100°C} - wt\%\ loss\ of\ LIG\ in\ air \qquad (6)$$

Both equations assume that any loss occurring at 100°C is purely due to the evaporation of water and the loss of LIG is found using a blank sample of LIG heated to 800°C in nitrogen gas for sulfur and in air for Ag NP.

To observe the sulfur distribution within the pores of the LIG fingers, they were encased in poly(methyl methacrylate) (PMMA, MW = 35,000, Acros Organics), formed through the dissolution of PMMA in acetone and dissolved PMMA was drop-casted onto the LIG fingers. Due to the low surface energy of acetone on LIG, it was expected that PMMA was able to also infiltrate the pores of the LIG. This was done so that the sulfur in the pores of the LIG would not sublime under the vacuum of the SEM/EDX chamber (as the sulfur crystals were found to slowly shrink and disappear with time during previous analysis). After the cast solution was dried, the sample was characterized through EDX.

To observe finer morphologies of the lithium plating samples, they were first rinsed with 1:1 EC/DMC without $LiClO_4$ in order to remove any residual salt. Afterwards, it was dried under vacuum to remove excess solvent and then imaged under the SEM.

2.3.8 Electrochemical Characterization

For the electrodeposition of lithium, the constant current and alternate pulse galvano cycling programs were used in the EC-Lab software of a BioLogic SP-300 instrument. The same instrument was also used to conduct electrochemical impedance spectroscopy (EIS) with the frequency range between 5 MHz and 100 mHz in potentiostatic mode.

In both the LSFB full cell, Li vs Li symmetric cell and S/LIG vs Li full cells, the cells were connected to a battery tester (BTS 3000, Neware). The full cells were cycled by galvanostatic cycling at 0.1 C between 3V and 1.5V, while the symmetric cells were cycled between +1.5V and -1.5V, at the same current as the full cells for a consistent current density. While most symmetric Li cells in a coin cell format would be cycled between +1V and -1V at most, the wider voltage range chosen in this instance is to accommodate any ohmic drop due to the distance between the sets of LIG fingers.

2.4 Results

2.4.1 LIG Electrodes

The open nature of the interdigitated architecture of the lithium sulfur flexible battery (LSFB) is inevitable in the device as PI is multifunctional, acting as the substrate, precursor for the electrodes as well as the separator between the opposite-polarity electrode fingers. This poses the challenge of requiring higher precision in the induction of electrodes for the anode in comparison to simply casting a slurry of electrode materials. However, the benefit of having the possibility for simple, cost effective processing as well as an open architecture for the opportunity

of conducting spectroscopic studies on the lithium-sulfur chemistry off-balances the challenges involved.

From the SEM images (Figure 9), it is clear that the pore structure appears to be hierarchical in nature, ranging from very large pores on the scale of several micron, to many smaller ones that are situated within these large pores. More specifically, some of the smaller pores appear to be fibrous in nature, as seen in the Figure 9b). BET confirms the mode of pore sizes below 10 nm as approximately 1.1 nm (Figure 10a)), which may be characteristic of the space between the fibrous structures. The presence of both very large pores and very small pores is desirable as a conductive host for the sulfur cathode due to the fact that large pores can facilitate rapid ion-transport while the small pores yield a higher surface area possible per mass of material so that the insulating sulfur can be well-distributed and be both ionically and electronically contacted. Especially in the present system where an ionic liquid-based electrolyte is used as opposed to a conventional organic solvent-based electrolyte, the ionic resistance is higher due to the increased viscosity. Thus, maximizing the ion transport is necessary to reduce any overpotentials required for cell operation.

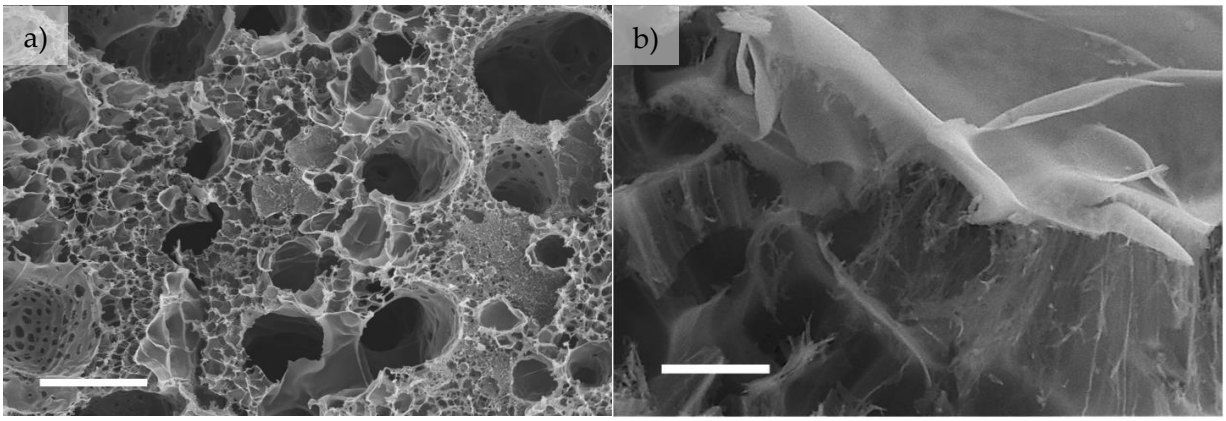

Figure 9. SEM image depicting hierarchical pore structure of LIG with scale bar = a) 10μm and b) 1 μm

Surface area measurements were conducted, and calculations based on the linear region of the BET isotherm ($0.05 \leq P/P_o \leq 0.35$, Figure 10b)) generated a surface area of 183.36 m^2/g. This value is quite far from graphene's theoretical surface area of ~2600 m^2/g [53], which suggests high occurrences of stacked material and the lack of ability for the laser source to properly induce few

layer graphene, yet at the same time, it is necessary to consider that most methods to produce single to few layer graphene involve low yield, time intensive methods like CVD or chemical exfoliation, requiring hours to days for production while laser-induction of graphene can be produced in seconds or minutes.

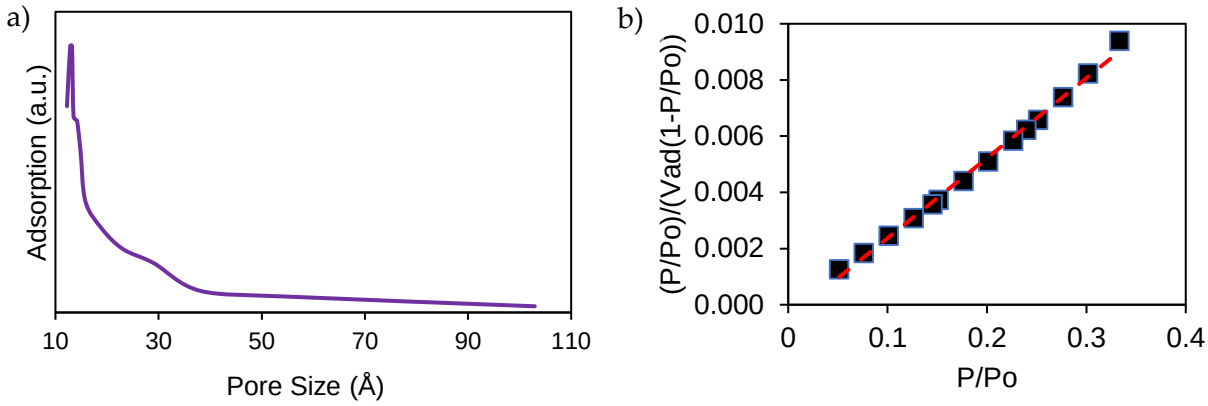

Figure 10. a) BET pore size distribution of LIG material and b) BET transform of isotherm between P/P_o of 0.05 and 0.35

It is also necessary to confirm the presence of graphene as opposed to amorphous carbon as the previous SEM image revealed that the structure of the LIG material is more akin to a 3D porous carbon like activated carbon as opposed to a well aligned 3D network of graphene. Thus, Raman analysis was conducted, and the spectrum can be found in Figure 11 and the characteristic D, G and 2D peaks can be observed at 1349.39 cm^{-1}, 1583.02 cm^{-1} and 2699.80 cm^{-1}, respectively. The spectrum obtained is consistent with the results of similar LIG work in published literature. [15,16,54,55] From the narrow G peak, it is clear that there is a significant graphenic region of sp^2 C atoms. The specific position of the G peak is also highly sensitive to the number of layers present in the graphene, ranging from single layer graphene at a peak position of 1587.1 cm^{-1} and graphite possessing a peak position of 1581.6 cm^{-1}. [50,52] According to equation (2), the estimated number of layers is, on average, ~3.

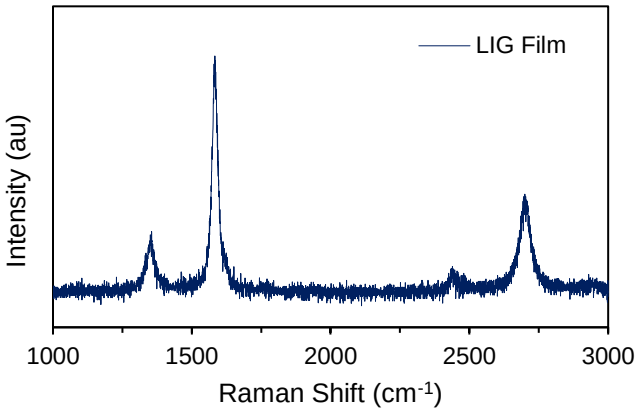

Figure 11. Raman spectrum for LIG film on PI with two laser passes at 10% power and 30 mm/s speed

The intensity of the D peak is reflective of the resonance due to scattering in the presence of a defect, such as the bending of sp^2 bonds. However, the ratio of I_D/I_G (here, I_D/I_G = 0.2014) suggests an abundance of nanocrystalline graphene domains. [52] The crystallite size was determined to be ~4 nm, hence nanoscale crystalline domains, as calculated by the relation in equation (3).

The 2D peak can be fitted with one peak at 2700 cm^{-1}, similar to single layer graphene. Without the splitting of this 2D peak, it is an indication that graphite is not present, but graphene. [56] The peak has an intensity of approximately half of the intensity of the G peak, which confirms that there is some stacking of layers of graphene, consistent with the calculated estimated layers of graphene above.

2.4.2 Cathode: Sulfur Deposition onto LIG

After the PI substrate is scribed with only the cathode (red area in Figure 5a)), sulfur is then deposited into the electrode. However, it is a challenge to introduce sulfur selectively into/onto the LIG electrodes, as sulfur is electrically insulating and is typically not electrodeposited onto an electrode. Traditional methods of introducing sulfur into a conductive host involves grinding of the elemental sulfur with the conductive host (e.g. carbon nanotubes, graphene, carbon black, etc.) followed by melt infiltration, a technique that has become very popular and widely adopted

from the Nazar group [19]. Unfortunately, due to the nature of the already formed electrodes by laser induction, it is not possible to directly utilize this common method to introduce sulfur.

As a result, in order to introduce sulfur into an already-formed porous conductive host like the LIG electrodes, a novel, two-step method is developed utilizing 1) the characteristic of heterogeneous nucleation to occur favourably on the defects and edges of surfaces like graphene as well as 2) the traditional melt imbibition technique (as depicted in Figure 6). To verify the effectiveness of this two-step method to introduce sulfur into the pores of the LIG material, the cathode material was analyzed under the SEM in backscattered electron detector (BSD) mode and EDX elemental mapping was conducted on the electrode prior and post-melting of the sulfur crystals after the first deposition. Figure 12a-d) depicts the presence of the sulfur crystals that have grown on the LIG electrode. Prior to the melting of these crystals, sulfur is present mostly only in the form of large (~10-25 μm diameter) crystals, seen in both c) and d). However, after the flash heating at 165°C, the temperature at which molten sulfur is the least viscous and is thus used as the temperature for melt imbibition [19], the sulfur is very uniformly distributed over the surface of the electrode so that it can readily be electrically contacted and reached by electrolyte for controlled redox reactions during cycling.

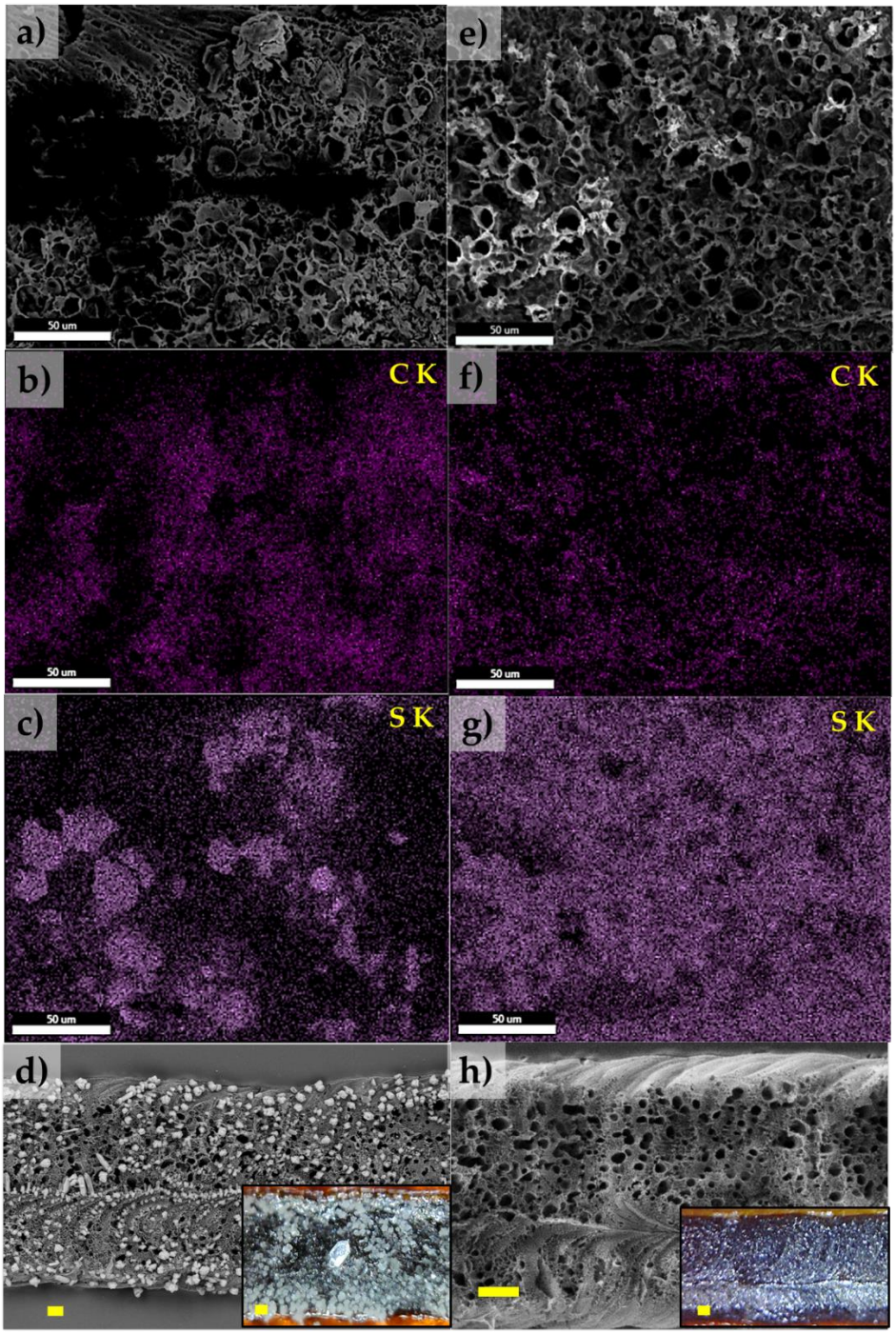

Figure 12. SEM/EDX mapping and optical microscope (inset of d & h)) images of the sulfur cathode after the first deposition of sulfur a-d) prior to the melting of the crystals and e-h) after the melting of the crystals to illustrate the presence of sulfur crystals that melt to uniformly wet the surface of the LIG. Scale bars in all images = 50μm

In order to better understand the distribution of sulfur within the LIG cathode after the melting of the sulfur crystals, the sulfur LIG fingers were encased in PMMA. During the drying process and acetone's high volatility, there was a great deal of strain in the PMMA film on top of the sample, resulting in a separation of the PMMA film at the top from the PI. This also led to the separation of the extruded LIG material from the LIG material that is below the level of the PI (from laser induction), but this is not expected to detrimentally affect the characterization. In Figure 13a), a larger cross-sectional area of the LIG sulfur cathode is shown with a separation of the LIG from the PI substrate, revealing brighter areas in the separated region (in the SEM micrograph under backscattered electron detector (BSD) mode) that corresponds to the accumulation of sulfur within large macropores of the LIG after the sulfur crystals were melted. This can be confirmed through the EDX elemental mapping as well. Although the EDX mapping shows a weak overall sulfur signal and a concentration of signal only near the bottom left quadrant, it is because of the low magnification of the mapping, which results in a smaller percentage of collected signal. Under a smaller cross-sectional area in Figure 13b), the sulfur is confirmed to be distributed over the LIG electrode still, proving that the sulfur did indeed wet and cover the surface area of the LIG, but also accumulated in larger pockets of space within the hierarchical structure. This finding could possibly suggest that the method of introducing sulfur into these LIG electrodes may have certain limitations. For example, during the wicking of molten sulfur into hierarchical pore structures, the sulfur would be easily wicked into the macropores first, followed by the mesopores. Lastly, the micropores would be filled with molten sulfur given sufficient time, as the wetting of viscous liquid into the micropores would be the most sluggish due to the small pore radius. Yet with the flash heating of the sulfur crystals, there may not be sufficient time for the sulfur to be drawn into the smaller pores, hence the observed collection in the macropores. However, this is not particularly concerning as sulfur has been known to redistribute over electrode surfaces upon cycling, a process called activation, and is expected to do so here [57,58].

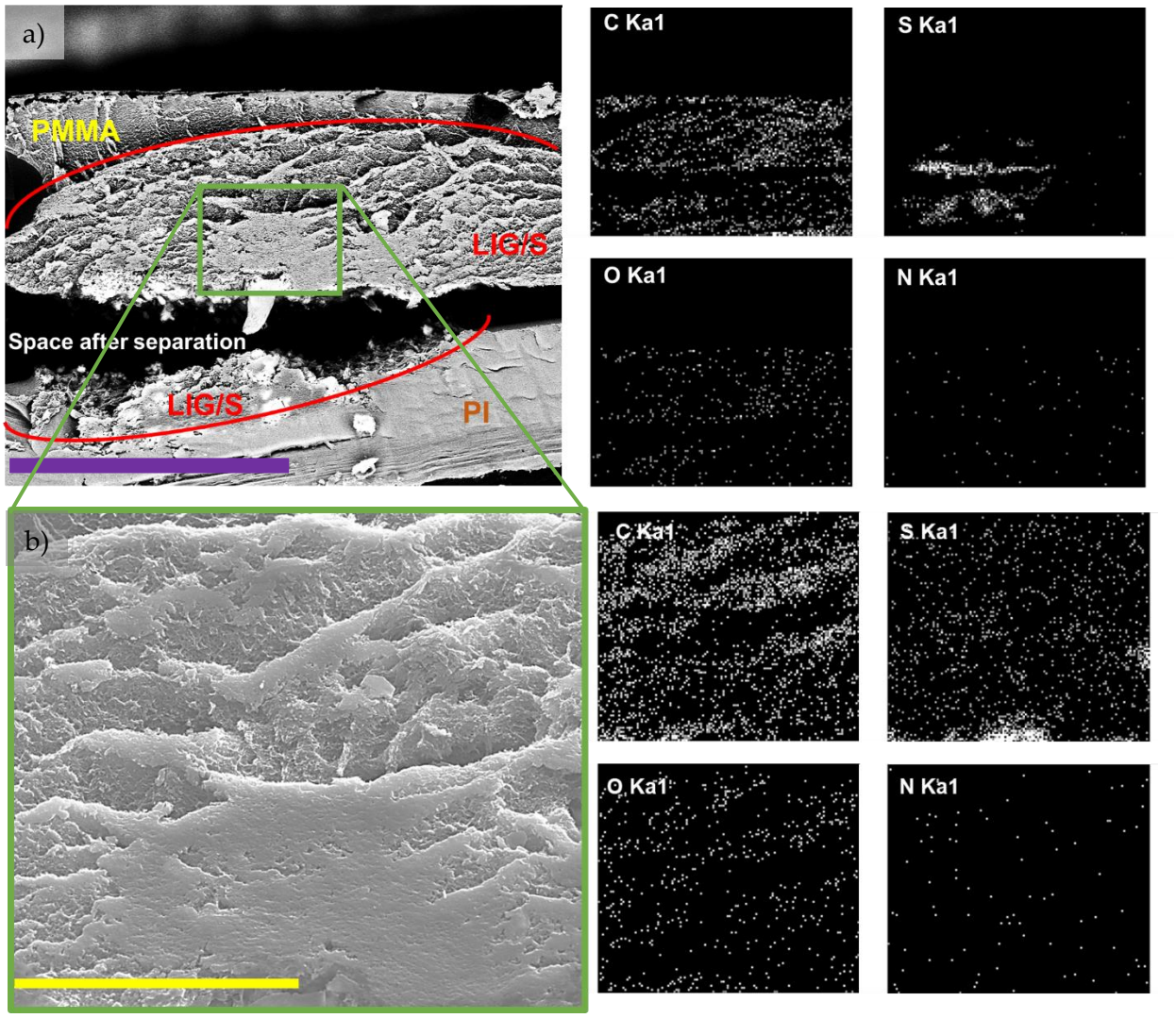

Figure 13. a) SEM micrograph in BSD mode and EDX elemental mapping of the cross-section of a LIG-sulfur cathode to indicate the distribution of sulfur within the pore structure of the LIG. Thicker sulfur films can be seen near the interface of the LIG/PI. Scale bar = 200 μm. b) SEM micrograph in SE mode and EDX elemental mapping of the cross-section of a LIG-sulfur cathode (indicated as the area marked by a green rectangle in a)). The close-up cross-section mapping of S Ka1 verifies that sulfur is still within the pores, contrary to the low signal of the large-area sulfur map in a). Scale bar = 50 μm

Digital images were taken of the cathode and are shown in Figure 14. Qualitatively, it can be observed that the nucleation density of sulfur crystals on the LIG electrodes is much lower for the first deposition compared to that of the second one. This can be explained by the fact that after the first deposition of sulfur where the melted sulfur crystals have wetted the surface of the electrodes, a very thin layer of sulfur was formed on the electrode surface. This provides many

more nucleation sites for sulfur in the subsequent depositions as heterogeneous nucleation on a like-material is more favourable than that on an unlike material, even though sulfur already preferentially nucleates on the edges and defects of the LIG.

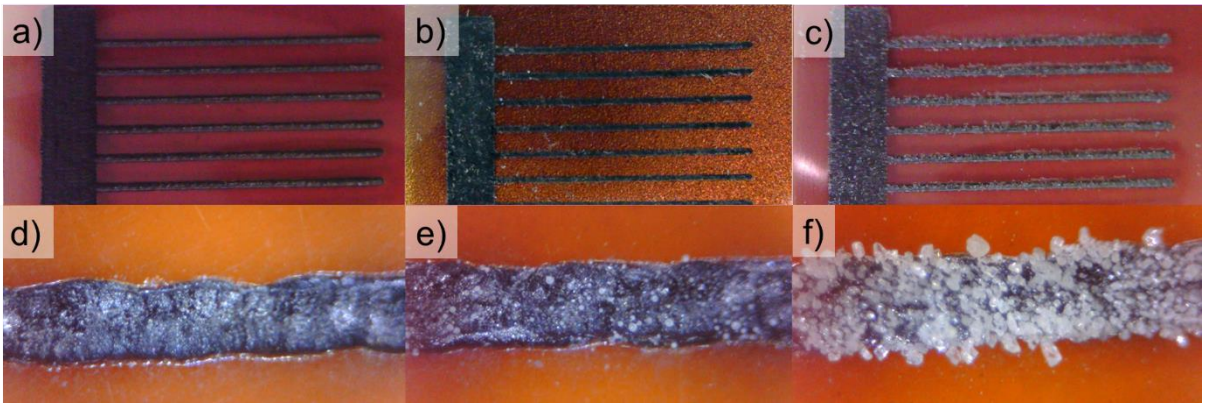

Figure 14. Digital images of LIG electrodes where a,d) show pristine LIG electrodes prior to any sulfur deposition and b,e) depict the electrodes after the first deposition of sulfur and the unmelted crystals while c,f) depict the electrodes after the second deposition of sulfur

Apart from the tendency of heterogeneous nucleation to occur at edges and defects, the surface energy of sulfur on the LIG versus the PI is also critical. Figure 15 depicts the differences in the wetting of molten sulfur on carbon versus PI. Glassy carbon was chosen as the substrate for this test as it is compositionally equivalent to LIG but due to its highly polished surface, it can be equated to a (near) perfectly smooth surface. The smooth surface makes it suitable for the contact angle (CA) comparison as it removes any surface roughness effects. While this is not a true CA measurement study for the two substrates, the digital images in the figure make it very clear that molten sulfur possesses a lower CA on carbon as opposed to PI. According to the Young equation, $\gamma_{LV}cos\theta + \gamma_{SL} = \gamma_{SV}$, where the surface energies of the solid (substrate), liquid (molten sulfur) and vapour (air) are compared to the CA, θ, sulfur also has a lower surface energy on carbon compared to PI. The lower surface energy enables a lower critical nucleation radius, thereby making the carbon more preferable for the heterogeneous nucleation of sulfur in this procedure.

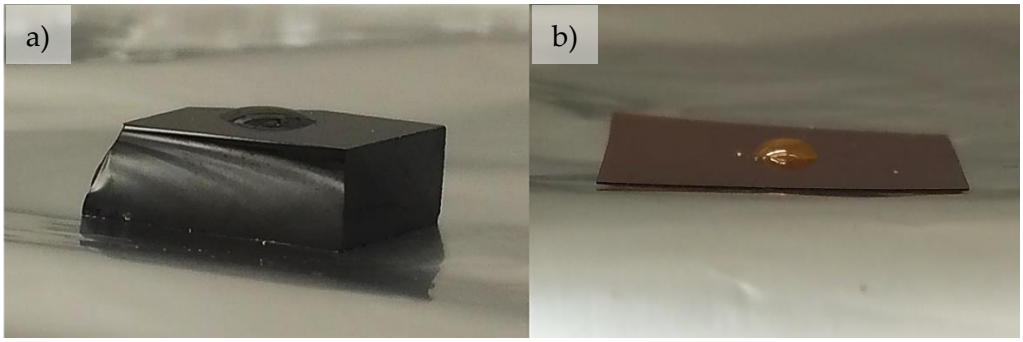

Figure 15. Digital images of molten sulfur droplet (10 mg) at 165°C on a) glassy carbon and b) PI to highlight the difference in wetting of sulfur on the two substrates and thus sulfur's preferential heterogeneous nucleation on carbon over PI

As previously mentioned, the deposition of sulfur onto the LIG cathode can be repeated until a desired loading is obtained. Practically, the optimal sulfur loading into an electrode was discovered to be between 3-5 mg/cm^2 in a review conducted by Pope and Aksay [17], where many literature publications of LiS batteries were analyzed in terms of the sulfur areal loading and the resulting energy density. A low sulfur loading led to an unoptimized usage of the electrode with high amounts of inactive material, but a high sulfur loading led to increased impedances during cycling and lower energy densities. It was only between 3-5 mg/cm^2 that the highest energy density (400-500 Wh/kg) is achievable. As a result, this was the target loading for the LIG battery system.

The repeatability of the deposition technique to yield a typical loading for a certain number of depositions was determined through the collection of samples (5 samples for each number of sulfur depositions) for TGA to determine the sulfur wt% within the LIG and displayed in Figure 16 as a box and whisker plot. It appears as though there is a higher amount of variability within the first two depositions, yet this decreases at four depositions, in which the average obtained wt% of sulfur is just about 75%, which is fairly acceptable and most common in literature reports of sulfur cathodes for LiS batteries. At four depositions, the loading is 3.9 mg/cm^2, within the aforementioned optimal loading and the theoretical capacities for each averaged loading as a function of sulfur deposition number is listed in Table 3. Theoretically then, if all of the sulfur introduced into the electrodes is electrically and ionically accessible, the capacity listed in the

table should be obtained and this can thus be a measure of how effective the deposition technique combined with the LIG material work together as a sulfur cathode.

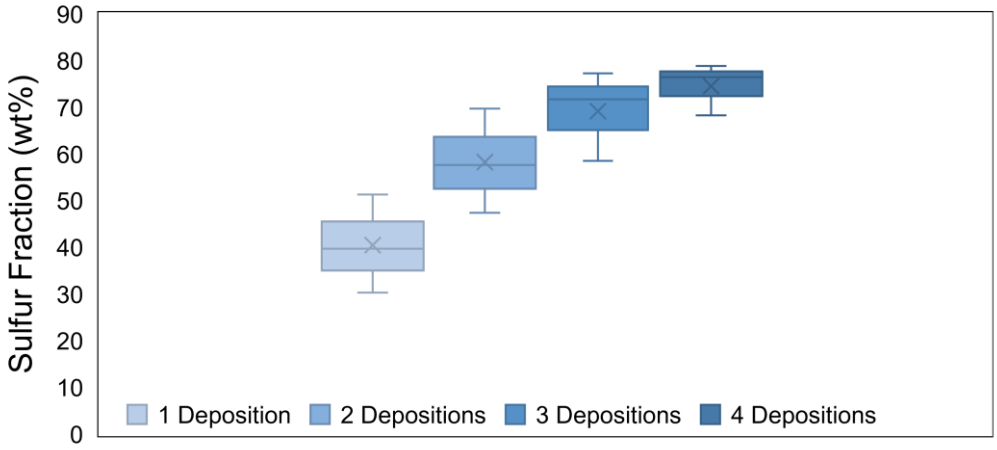

Figure 16. Box and whisker plot for TGA results of sulfur wt% as a function of number of depositions

*Table 3. Average wt% of sulfur and the corresponding loading and theoretical capacity obtainable as per Figure 16. *Loading calculated is dependent on the area of the sulfur cathode alone*

wt% of Sulfur	Loading (mg/cm^2) *	Theoretical Capacity (mAh/cm^2)
40.5	0.9	1.5
58.3	1.9	3.1
69.2	3.0	5.0
74.6	3.9	6.5

2.4.3 Anode: Lithium Metal Electrodeposition onto LIG

There are a number of challenges present with the electroplating of lithium, especially into a porous foreign substrate. These challenges will be discussed in further detail in Section 4.1 later but two of these challenges are addressed in this present section: 1) lithium has a high nucleation barrier (due to its high surface energy) leading to high overpotentials for nucleation on non-

wetting substrates and 2) its tendency to form dendritic morphologies during plating at practical current density.

A physical challenge of working with interdigitated electrodes for electroplating, especially with Li metal, is that if the plated metal is not uniform along the length of the fingers, there may be short circuiting with the adjacent fingers of opposite polarity. Particularly for Li metal, if the initial plated metal begins as non-uniformly porous and rough in morphology, it can accelerate the formation of Li shorts during cycling, leading to rapid cell failure. Since LIG is still a 3D porous film, it cannot be avoided that the morphology will be rough at the microscopic level since LIG itself is not a uniformly porous material. However, at the very least, the macroscopic roughness can be mitigated to produce a somewhat more uniform film of Li along the length of the fingers. This can be done so by using Ag NP and RPP.

Certain metal nanoparticles, such as silver, have been suggested for use as nucleation seeds to reduce the nucleation barrier of lithium plating as the solubility of lithium in the nanoparticles lowers the nucleation activation energy [44]. For example, in Figure 17b), the overpotential present with carbon as a substrate (marked by the green curve) is around 25 mV while in Figure 17a), the overpotential for silver as a substrate (marked by the orange curve) is practically non-existent. This is because lithium forms alloys with silver in the process of lithium plating, while some carbons are only capable of being lithiated or act only as substrates purely for plating, hence the overpotential present. It is for this reason that silver nanoparticles were chosen to act as seeds for the electrodeposition of Li onto the LIG material.

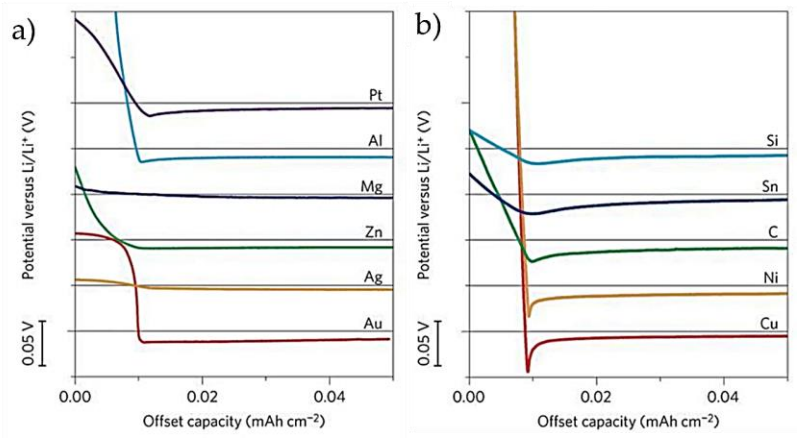

Figure 17. Voltage profiles of Li electrodeposition onto various substrates where Li has a) some solubility and b) negligible solubility as obtained from [44]*. The capacities are offset to show where the Li plating on the substrate begins and the horizontal lines present are to show where the 0V mark is, with each vertical division being 0.05V*

SEM was used to verify the presence of Ag NP in the anode after the imbibition (Figure 18a)). Under BSD mode, the much higher elemental number Ag NP appears to be very bright in the SEM micrograph and it can be observed that the size of the NP used vary from almost 1µm to tens of nm in diameter. It is apparent from these images that the size of the NP is not monodisperse nor uniform. This is mostly due to the fact that the Ag NP are dried onto and into the LIG fingers. As a result, the drying process will inevitably lead to agglomeration and growth of the NP from a reduced electrostatic repulsion in the absence of a liquid medium. However, for the purpose of acting as Li plating seeds, the specific size and polydispersity of Ag NP is not critical to its function to reduce overpotential during plating. Moreover, the TGA results (Figure 18b)) show that a typical loading of Ag NP using this imbibition method followed by drying yields an Ag wt% of ~4% when LIG with and without Ag NP is heated under air.

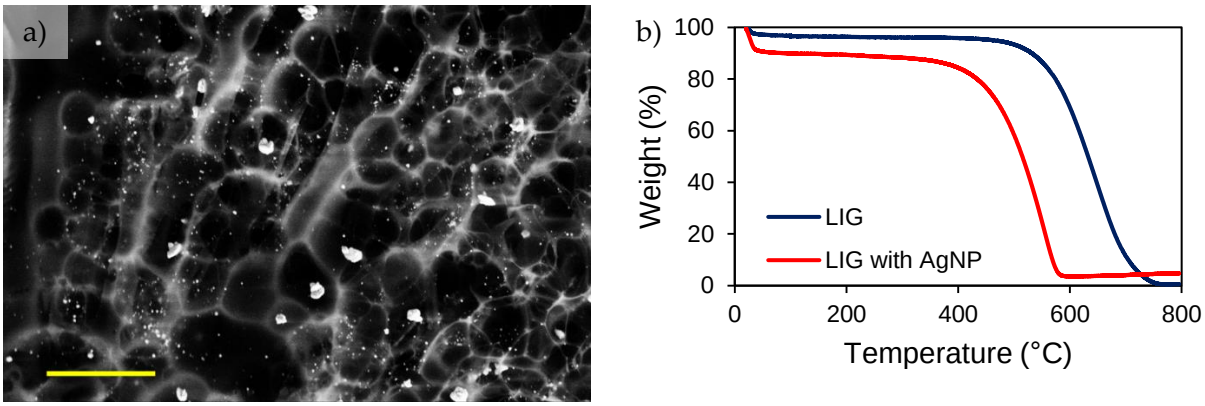

Figure 18. a) SEM micrograph in BSD mode of Ag NP present in the LIG electrode after imbibition. Scale bar = 5 μm; b) TGA results of LIG with and without Ag NP run in air for the determination of loading

Even with Ag NP, Li electrodeposition is still limited in terms of the plating current density as higher currents tend towards dendrite formation. Typically, it is recommended that Li electrodeposition current densities do not exceed 0.1 mA/cm^2 as higher current densities will result in Li ion diffusion limitations, tending towards porous and mossy morphologies. However, it is also not a practical approach as it would require a very long time in order to electrodeposit a sufficient amount of Li metal to stoichiometrically balance the sulfur in the cathode.

To address the trade-off of requiring lower plating currents, an RPP technique was applied. This plating technique involves forward, cathodic currents interrupted by brief pulses of reverse, anodic currents of higher intensity. The rationale for using pulse plating over DC plating is to compensate for local, diffusion-limited regions that will be present in solution when using higher current densities which can be replenished through interruptions in the cathodic current. With the introduction of the anodic current pulses as well in the case of RPP, unwanted protrusions which can grow into dendritic structures can be dissolved to form more uniform deposits [46,47]. Additionally, the thickness of the electric double layer (EDL) is proportional to the overpotential present in the cell. As a result, Li ions are obstructed from reaching the electrode, especially more so at high overpotentials. Thus, the dissolution of Li protrusions and breaks in the forward current are very effective towards aiding Li ions to reach the working electrode.

The plating voltage curve and EIS spectra (as a function of the amount of lithium plated out of the 2.5 times stoichiometric amount) are displayed in Figure 19a) and b), respectively. As the voltage measured will "jump" with each anodic pulse, only the voltage measured for the cathodic pulse is indicated in Figure 19a) and the inset shows the measured voltage jumps with the anodic pulse over 20 cycles of cathodic-anodic pulses. Due to the presence of the silver nanoparticles, the initial nucleation overpotential is negligible and the measured plating overpotential is about 40 mV (as seen in the inset figure).

To probe some of the changes in the LIG anode during the course of plating, EIS was conducted at 0%, 25%, 50%, 75% and 100% plating capacities. The initial state of the anode indicated a higher resistance in the electrode components, R_e = 93.6 Ω, but a small semi-circle corresponding to the double-layer capacitance inherent of the LIG electrode material. Upon plating, the semi-circle enlarges with the presence of a more porous electrode with the plated lithium while the electrode also becomes more conductive, R_e ~ 60 Ω.

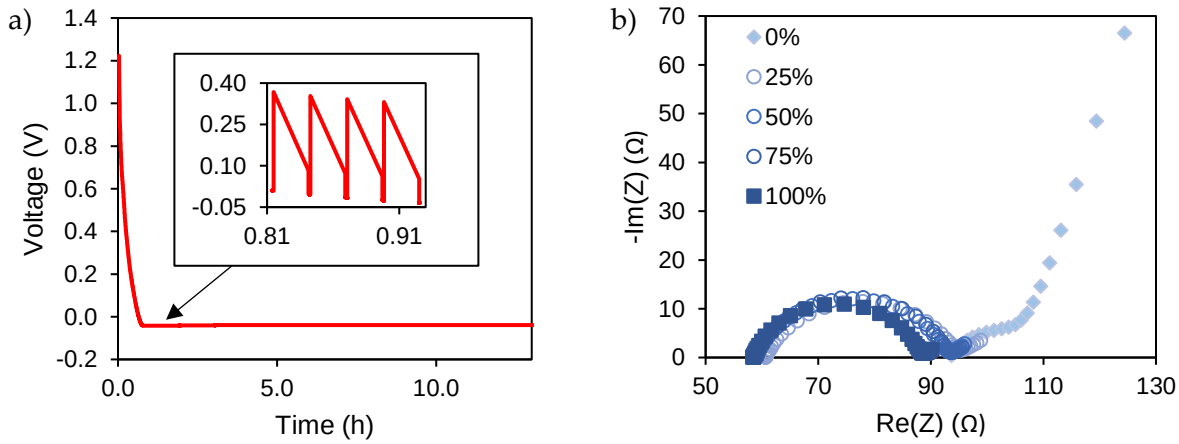

Figure 19. a) Plating voltage curve of lithium onto the LIG; b) EIS spectra as a function of the 2.5 times stoichiometric amount of lithium

Digital images of the LIG electrodes were taken of the cross-section and top-down view at 25%, 50%, 75% and 100% of the plating capacity selected and displayed in Figure 20. In Figure 20a), lithium metal is seen as the larger, silvery-grey regions in the LIG cross-section (compare with S cathode). Most of the Li metal when deposited appears to first grow on the tips of the M-

shaped cross-sections (observable at 25% and 50% plating capacities). This is expected so since this region is physically closer to the counter electrode. Furthermore, since the tips are convex, the electric field generated in this region is also stronger, giving a stronger pull towards the Li ions. After the initial preferential plating at the tips of the M-shaped cross-section, Li is then somewhat more uniformly plated at the surface of the LIG, forming a rough dome and spreading out at the edges of the fingers towards the adjacent cathode fingers (observable at 75% and 100% plating capacities). While the images in Figure 20 correspond to LIG fingers plated with Li using Ag NP seeds and RPP, similar results are observed with RPP without Ag NP and direct current (DC) plating without Ag NP. The main difference in the result is the obtained morphology of the plated Li on the LIG which will be discussed later below.

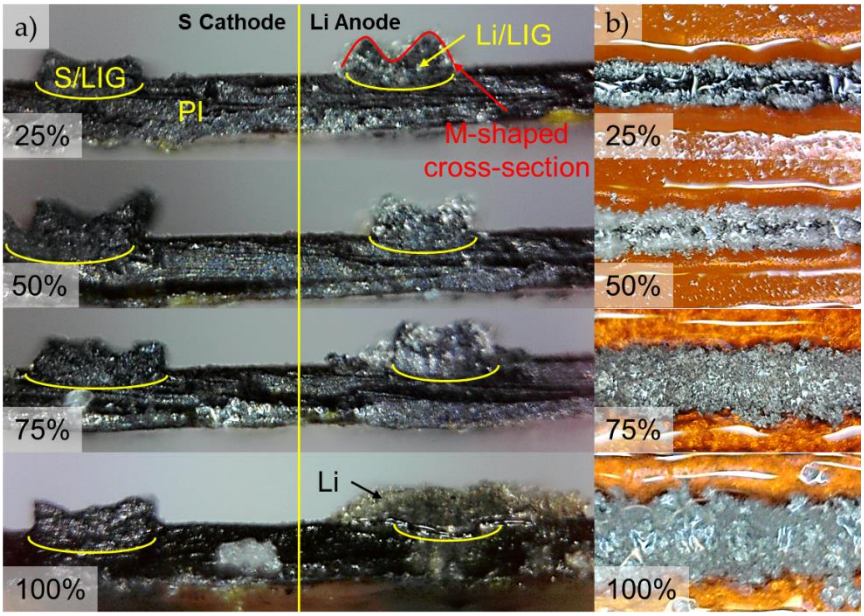

Figure 20. Digital images of the a) cross-section of Li plating on the LIG fingers at different plating capacities. The anode is shown on the right with the sulfur cathode on the left; and b) the top-down view of Li plating on the LIG fingers at different plating capacities. Here, Li was plated with Ag NP seeds as well as RPP

To illustrate the improvements in the macroscopic morphology of plated Li by using Ag NP and RPP, samples plated with DC without Ag NP, RPP without Ag NP and RPP with Ag NP were prepared. As mentioned earlier, current densities above 0.1 mA/cm^2 are not generally recommended due to the poor plated Li morphology. However, to highlight the importance and

results of pursuing methods to mitigate high current density consequences, 1 mA/cm^2 was selected for all studies. Digital images were taken to compare the resulting Li film that was plated in Figure 21, where a,d) depict the sample plated with DC without Ag NP, b,e) depict the sample plated with RPP but without Ag NP and c,f) depict the sample plated with RPP and Ag NP.

From Figure 21a,d), the macroscopic morphology can be seen to be very rough and bulbous due to the high current density used. It is also especially noticed that the Li metal had plated more preferentially at the end of the finger due to the heightened electric field at the ends of the traces, leading to an inhomogeneous plating along the length of the finger apart from just the width of the fingers as discussed previously. Due to the preferential deposition at the tips of the fingers, the sample also suffered from severe short circuiting along many regions of the anode fingers.

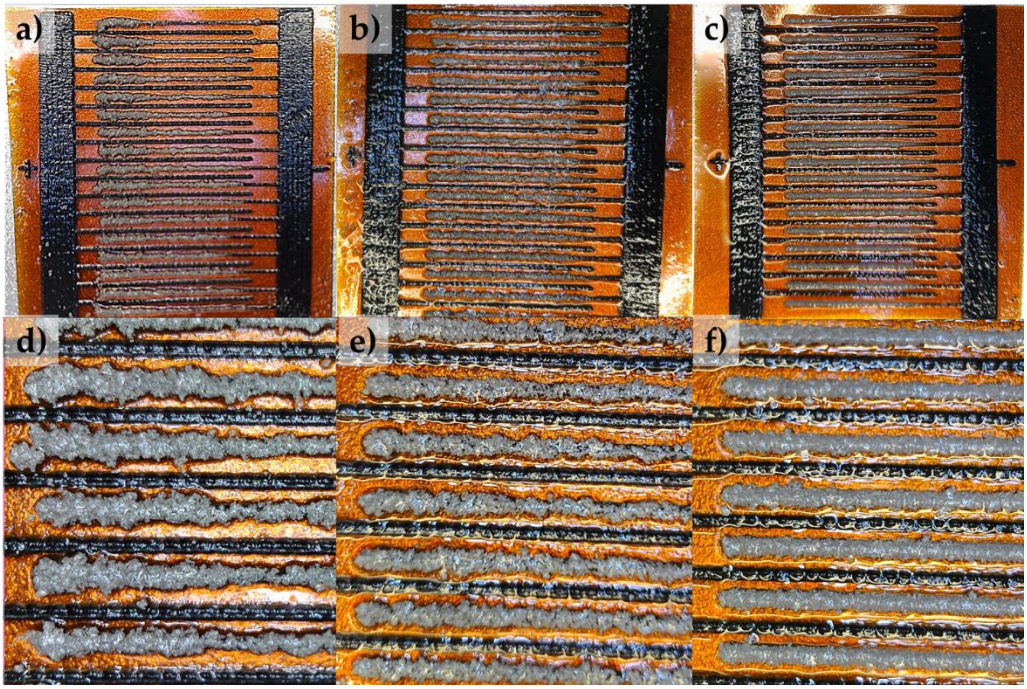

Figure 21. Digital images of electrodes after lithium electrodeposition using a,d) DC plating without Ag NP, b,e) RPP without Ag NP and c,f) RPP with Ag NP, where all samples were plated at a(n) (average) current density of 1 mA/cm^2 to a capacity of 12 mAh/cm^2.

By utilizing RPP, the homogeneity along the fingers vastly improved so that it is more or less uniform without any short circuiting of the sample (Figure 21b,e)). This is owing to the presence of the reversed pulses of high current density at 10 mA/cm^2, which allows for an

interruption of the forward high current pulses to replenish the local ion concentrations through dissolving Li dendritic protrusions. However, the Li film is still irregular as a result of the high nucleation potential that Li metal has on carbon [44]. The high nucleation potential then leads to the formation of overlapping islands of multilayered-growth crystals of Li [59,60] as opposed to layer by layer growth on an otherwise low nucleation potential substrate. The morphology at higher nucleation potentials would not be too critical an issue if the substrate were a 2D substrate. However, as the substrate is a 3D irregularly porous substrate, it becomes very difficult for a macroscopically uniform film of Li to be plated. This is especially so since it would be more preferential for latter Li ions to adsorb onto Li crystallites already present than to adsorb and nucleate on fresh carbon surface. It is for this reason that the Ag NP-seeded growth of electrodeposited Li metal on LIG combined with RPP yields the smoothest macroscopic morphology (Figure 21c,f)), where the roughness of the Li is very much improved while maintaining a homogeneous film along the entire length of the fingers.

While the macroscopic differences in morphology have been more obvious, the macroscopic structures observed with the eye are formed through the microscopic structure affected by the different plating techniques and presence of Ag NP alloying. Accordingly, it would also be necessary to ascertain the expected microscopic structures. SEM micrographs were obtained for the plating samples from Figure 21 and shown in Figure 22. The sample plated by DC in a) yields a stringy, "noodle-like" microstructure, reminiscent of Li dendrites leading to the failure of Li metal batteries. It is the uncontrollable growth of these stringy microstructures that likely cause the bulbous macrostructures. The samples with RPP in both b) and c), without and with Ag NP, respectively, have a reduced amount of the stringy microstructure, but are characterized by the presence of a different microstructure. These samples have many very small "flower-like" deposits on the existing, larger Li structures. While these deposits are also present in the DC plated sample, they are not as prevalent. They can be explained as the beginnings of what could become longer needles that form the structures seen in Figure 22a), but due to the high reversing current, the flowers do not generally grow to become stringy but may merge

together as islands to form the film (Figure 22c)). Due to the increased merging of these flower deposits, the macrostructure of the samples with RPP are more dense, controlled and uniform.

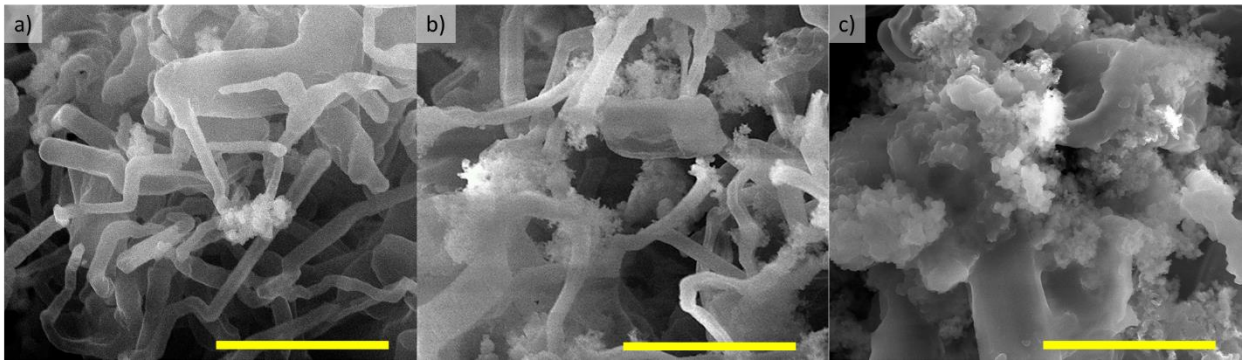

Figure 22. SEM micrographs of samples plated by a) DC plating without Ag NP, b) RPP without Ag NP, c) RPP with Ag NP. Scale bars = 10μm

Ideally, the LIG fingers would not simply just act as a 2D electrode in that all the Li plated would be at the surface, but that the LIG fingers would act as a 3D current collector and host for the Li metal. This would allow for the local current densities to be reduced during the stripping and plating process, also simultaneously reducing the local overpotentials, ideally providing a more densely plated structure. From Figure 23a), it is clear that there is a thick, porous film of Li on top and around where the LIG finger is. Because of the nature of LIG as a working electrode for Li electrodeposition, the resulting film is not a uniform and dense film but one that is likely as porous as the LIG itself, as was confirmed earlier through EIS in Figure 19b). Additionally, the growth of Li films has previously been shown to be strongly affected by the pressure applied to the cell against the propagation of Li film itself. The application of pressure against the growth of Li is expected to ensure that Li deposition occurred as densely as possible in/on the porous host (filling gaps, pores, etc.), thereby reducing the irreversible consumption of electrolyte and improving cycling efficiency [60]. But with the open architecture of the LIG fingers, it is challenging to apply pressure to the electrodes during plating or cycling to confine the growing and receding Li film.

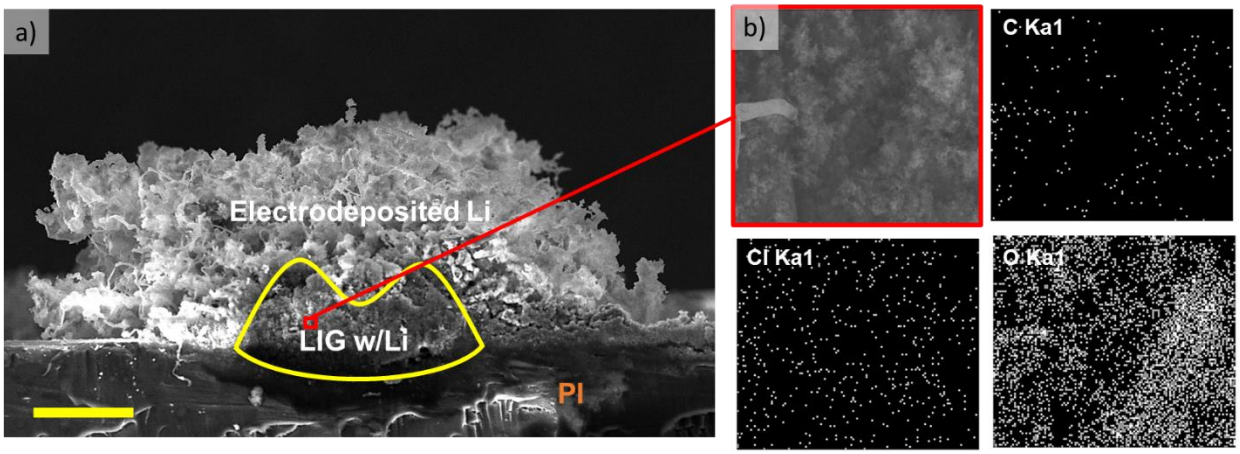

Figure 23. a) SEM micrograph of cross-section of Li plated on the LIG anode after rinsing excess plating electrolyte and salt. Scale bar = 100μm. b) EDX elemental mapping of the interior of the LIG anode, showing that Li had also plated within the finger. This sample was plated with Ag NP using RPP and plated to a 2.5x stoichiometric amount of Li.

An EDX elemental mapping was conducted of a small region within the LIG anode and the presence of chlorine is an indicator of LiCl as a decomposition product of Li reaction with the electrolyte at the LIG surface forming SEI [61], which would occur with the lithiation and plating of Li within the LIG finger. The high oxygen content is also due to the presence of other decomposition products, many of which are composed of both Li and O, such as LiOH, Li_2O, $LiCO_3$ and Li_2O_2 [61]. Li cannot be directly observed through EDX due to it being a very light element, thus Cl and O were chosen instead to indirectly infer the presence of Li plating within the finger from the formation of SEI with the reaction of Li and the electrolyte.

2.5 Electrochemical Results

2.5.1 LIG-Based Full Cell

The first three discharge and charge curves can be found in Figure 24a), where the first discharge yields a specific capacity of over 1000 μAh/cm^2, or an equivalent of over 250 mAh/g (at the current sulfur loading of ~3.9 mg/cm^2). This value exceeds many reports of thin film or flexible batteries, including ones made from microfabrication techniques, as seen in the Ragone plot of Figure 24c). The voltage profile is very typical of a LiS chemistry system, with an upper plateau of around 2.3 V and a lower plateau around 2.1 V. However, upon the first charge and thereafter, the capacity of the battery suffers a very rapid drop. Usually LiS batteries undergo a few work-in cycles where the capacity of the cell will fade slightly due to the establishment of a stable SEI at the expense of electrolyte decomposition and irreversible reactions with the Li metal. In this case, as the Li metal is introduced through electrodeposition, there is already an inherent layer of SEI as seen in Figure 24d). To illustrate the presence of the SEI layer on the anode fingers, all the Li metal was stripped away from the LIG to leave behind an obvious grey deposit that is the SEI formed during electrodeposition. Ideally, this SEI layer formed should be sufficient to protect the Li plated in latter cycles from further degradation. In light of this, a reduction of the magnitude observed in both a) and b) of Figure 24 is highly unusual. The subsequent cycles do experience a relatively more stabilized capacity after the initial drop, but the capacity fade at the beginning required further investigation.

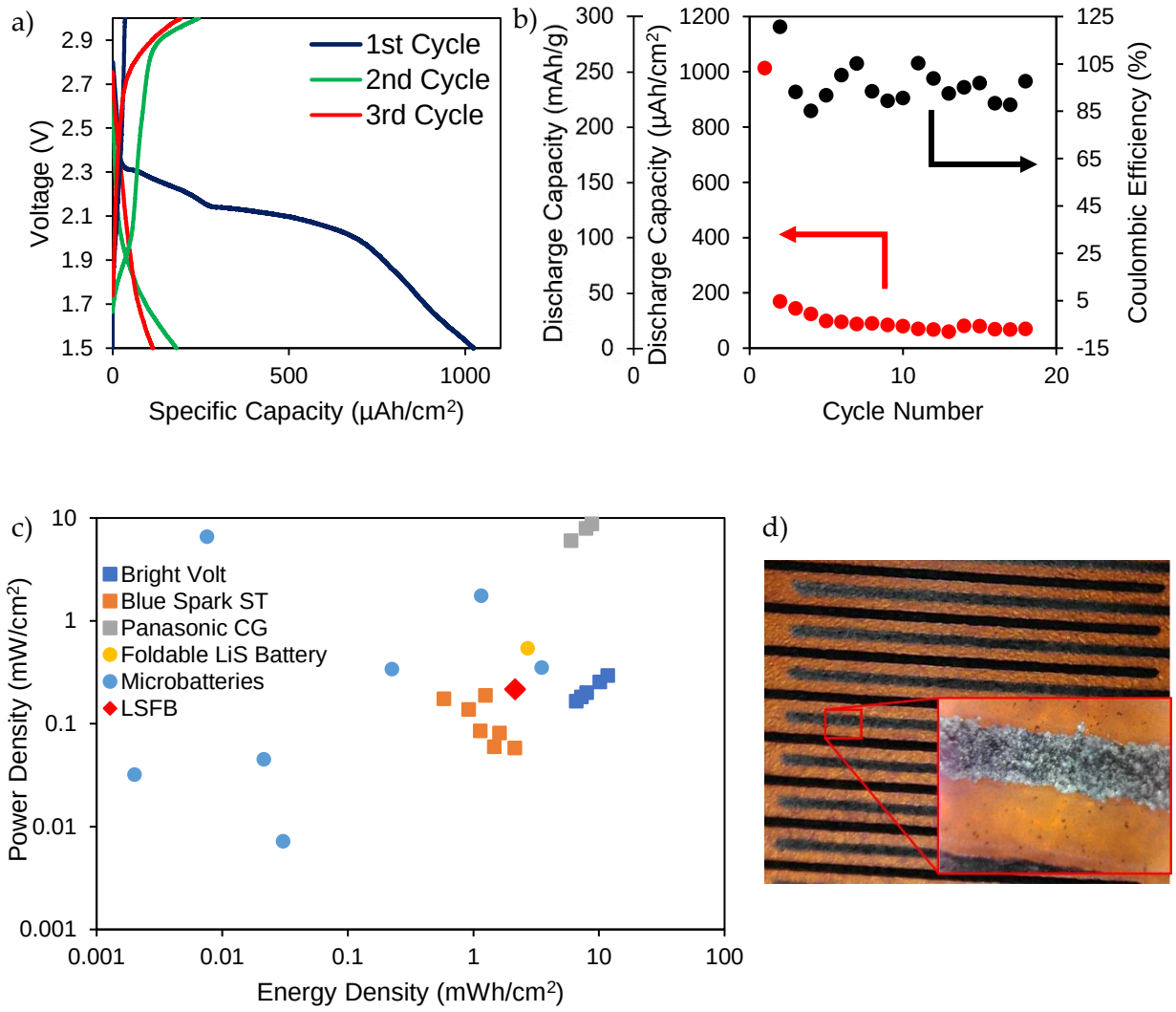

Figure 24. a) Typical voltage curves of the first three discharge and charge cycles, b) Galvanostatic cycling results of a full cell, c) Ragone plot comparing LSFB (red diamond) to thin-film/flexible/microbatteries present on the market (squares) [62]–[64] *and in literature (circles)* [9], [11], *d) Digital image of Li anode fingers after completely stripping Li metal to 1 V vs Li, indicating the grey SEI remaining*

2.5.2 Li vs Li on LIG Fingers

As most of the capacity loss can be elucidated by the consumption of Li through SEI formation during the first cycle, it is of interest to conduct a Li versus Li test on the LIG fingers where Li is electrodeposited on both sets of fingers at an equivalent capacity and cycled (Figure

25). Obviously, both during plating and cycling, the Li plated will experience side reactions leading to an efficiency that is consistently below 100%. The first discharge capacity in the symmetric cell is 0.222 mAh, which is about 16% the value of the theoretical capacity that should have been obtained based on the amount of Li plated on the fingers. This shows that the first cycle of plating Li from one electrode to the other led to a rather large loss of useable Li to side reactions in the formation of SEI. After a slower, gradual decrease in capacity over the next 5 cycles, the capacity remains constant, suggesting that a significant amount of sacrificial Li was necessary in order to produce a stable SEI after the change in electrolyte.

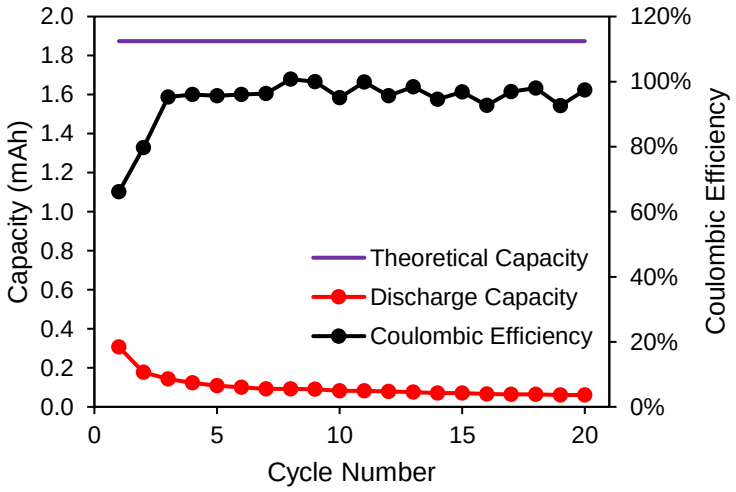

Figure 25. Cycling results of Li vs Li on LIG fingers, both plated to a capacity of 1.874 mAh, which is displayed as the purple horizontal line

In comparing this 16% retrievable capacity of the Li-Li symmetric cell to the capacity reduction in the full cell, it can be concluded that there is a correlation between the drop in capacity in both systems. For the full cell, the reduction in capacity at the second cycle is from ~250 mAh/g to ~42 mAh/g, or about 17% of the first cycle's capacity. Previous analysis on the sulfur cathode indicated that not all of the sulfur is properly electronically contacted due to the thick layer of sulfur films in the macropores. As a result, the low capacity obtained in the first cycle can be attributed to the limitations of the sulfur cathode. However, the re-plating of lithium metal in the charging cycle followed by the second discharge led to a capacity that is 17% of the first discharge. Assuming that the ~250 mAh/g capacity of the first cycle is approximately the

maximum achievable by the sulfur cathode, it can be assumed that the reduction of capacity seen in the second cycle is owing to the loss of retrievable Li due to SEI formation in the initial cycle. This phenomenon, though observed in all LiS systems, is particularly heightened in this LIG-based system due simply to the fact that the Li was electrodeposited onto a highly porous, 3D graphene structure. The high surface area of the LIG provided many reaction sites for the formation of SEI in addition to the limited Li metal present in the initial system as opposed to an infinite reservoir of Li metal found in a sheet of Li in coin cell battery forms.

2.5.3 S/LIG vs Bulk Li

To further verify that the limitation faced in the full device is a result of the low utility of the plated Li metal, the cathode material formed through the repetition of the novel nucleation-imbibition technique was used as the cathode material in a coin cell configuration with a piece of Li metal as the anode. While the loading is the same between this coin cell and the interdigitated system, the most important difference is that the coin cell uses a dense, thick lithium foil which is several orders of magnitude in stoichiometric excess.

From the cycling results in Figure 26, the most notable observation is that the specific capacities obtained are very low compared to the theoretical capacity of 1672 mAh/g. This can be attributed to the fact that there are regions of agglomerated sulfur that are not electronically contacted by LIG, as was established previously in Section 2.4.2. Aside from the low capacities compared to the theoretical value, the obtained capacity in both electrolytes are initially very similar while the ether-based electrolyte cell suffers a more rapid capacity fade, followed by a stabilized capacity. The RTIL-based electrolyte, on the other hand, suffers a slow and gradual capacity fade, causing it to reach a very similar capacity of ~110 mAh/g as the ether-based electrolyte (~105 mAh/g) at the end of 33 cycles.

Another observation is that the initial capacities obtained for these cathodes are very similar not only to each other but also to the LIG-based full cell, at least for the first discharge. The first discharge in the LIG-based system gave a capacity of 259 mAh/g while the coin cell configurations

gave capacities of 270 mAh/g and 239 mAh/g, for the RTIL-based and ether-based electrolytes, respectively. For the coin cells, the capacity retention from the first to the second cycle is ~86% and ~72% for the RTIL-based and ether-based electrolytes, respectively. While capacity fade is observed even in the coin cells, it is not as severe as the full cells with the limited Li anode, which was a 17% retention of capacity in the second cycle. This confirms that in a system not limited by the Li anode, the S/LIG cathode is functional, though perhaps not a high performing electrode, but the nucleation-imbibition technique, though it can be further optimized, is effective for depositing sulfur within a porous carbon structure.

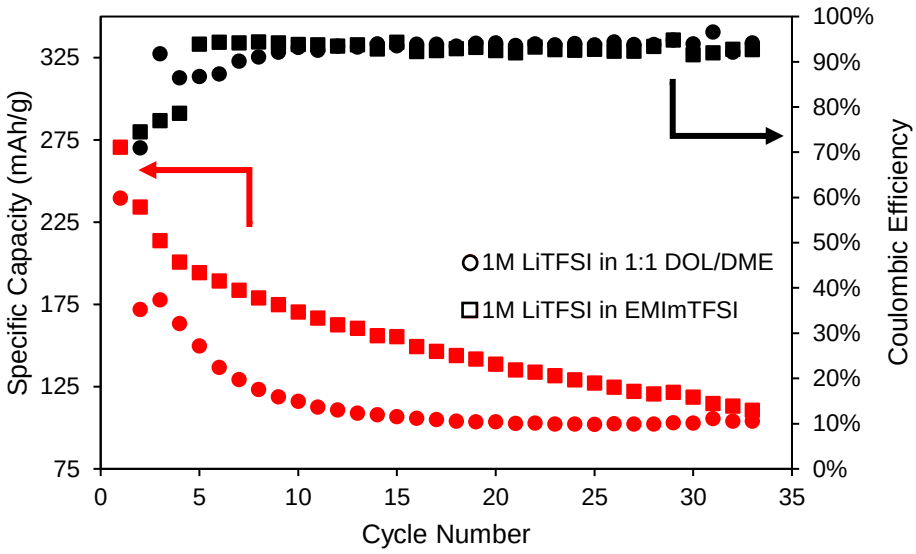

Figure 26. Cycling results for S/LIG material vs. bulk Li anode in a coin cell configuration in two different solvents, 1M LiTFSI in 1:1 DOL/DME (ether-based electrolyte) and 1M LiTFSI in EMImTFSI (RTIL-based electrolyte)

2.5.4 Other Methods of Li Introduction

At this point, it should also be noted that the results of electrodeposited Li on LIG suggest the fact that this may not be the most ideal method of introducing Li despite the simplicity and cost effectiveness of the technique. As the rationale behind using DLW and solution-based processing for the fabrication of the device was to retain a simplistic and scalable process, it was

decided to avoid any possibly high-cost steps, such as cleanroom techniques. Efforts to improve the electroplating of Li and also other efforts to avoid electroplating Li while maintaining a simple procedure were attempted as well. These efforts were not included in detail this thesis work but will be briefly mentioned here.

It was hypothesized that the LIG possibly possessed too many defective sites which led to the defect-catalyzed decomposition of the electrolyte resulting in the low Li utility. Thus, attempts were made to introduce a very thin layer of Cu through electroplating to act as a plating substrate for Li that would be somewhat more inert. Cu was electrodeposited in a setup similar to that which was used for Li plating but in a bath of $Cu(II)SO_4$ in water. However, it was found that the introduction of a Cu layer that covered the entire surface of the porous LIG resulted in decreased flexibility of the individual fingers. The fingers then delaminated from the PI substrate, removing the LIG as well.

In a separate attempt to improve Li utility using electrodeposition, it was thought that the SEI on the LIG could be stabilized through cycles of plating and stripping (P&S) Li from the LIG anode. However, after 20 cycles, the Li utility finally increased only to about 40%, but due to the time scale required for such a poor result, this technique was deemed to be impractical.

While Li metal can be introduced with higher efficiency through thermal evaporation or sputtering, Li metal could also be melt imbibed into pores due to its relatively low melting temperature, compared to most metals, at 180.5°C. Unfortunately, as Li is a metal, its surface energy is very high and thus would not be wicked into a porous host like LIG. However, molten Li metal has been shown to reactively wet and fill a porous host that possessed a conformal ZnO layer formed through ALD [65]. Taking this idea but avoiding the high capital cost of using ALD, ZnO nanoparticles (NP) were synthesized and imbibed into the LIG in hopes that the NP could possibly still draw the molten Li into the pores of the LIG. Unfortunately, this was unsuccessful and only certain sites of the ZnO on the LIG were wet with Li.

In a similar manner, GO was shown to successfully act as a host for reactive wetting with Li due to the oxygen functional groups present that would react with and draw in the molten Li

[66]. Thus, it was attempted to use ozone treatment as a low cost technique for the introduction of functional groups on the LIG that could possibly react with molten Li and allow the pores of the LIG to be filled with Li. The result of this effort was also negative and Li did not wet the LIG.

Considering the results of these other methods that were undertaken to introduce Li into the LIG, the final Li deposition technique presented in Section 2.3.3 was selected and presented Additional research would be required to determine a low cost yet effective manner for Li introduction into a porous carbon host like LIG.

2.6 Conclusion

The concept of using LIG electrodes for the fabrication of LiS batteries has been shown possible through the development of a novel, two-step nucleation-imbibition technique combined with the electrodeposition of lithium aided by RPP and Ag NP seeding. With the preliminary results, the system has shown itself to be capable of reaching capacities that exceed the reports of flexible and thin-film batteries, even ones fabricated with cleanroom techniques. However, it is also clear that the performance of these devices is also limited by the pore structure of the LIG for the distribution of the molten sulfur during the melt imbibition process as well as the utility and efficiency of the Li metal plated onto the graphene traces. As such, further work is required to both characterize the LIG and determine methods of controlling the pore structure as well as understanding the efficiency of Li plating on carbon materials within different electrolytes.

3.0 PI-Derived LIG Properties

3.1 Introduction to LIG

Since its discovery, graphene research has grown in many different applications owing to the numerous alluring properties of strength, surface area, carrier mobility, etc. [67]. In particular, it has been very attractive and widely used as electrodes in electrochemical devices. This is due to its high surface area, wide potential stability window, electrical conductivity and chemical stability [68]. Yet, the challenge with working with graphene-based electrodes is to reach a maximum surface area while attempting to minimize any amount of aggregation and stacking from the van der Waals forces between the sheets. Additionally, simpler, scalable, cost-effective ways must be determined for the synthesis of graphene for it to be used in industrial manufacturing of electrochemical devices.

Recently, there has been interest in looking into methods for directly patterning graphene electrodes for simpler and faster approaches to forming conductive electrodes in thin film and micro-electronics. In 2012, El-Kady et al. found that a film of GO could be reduced by a DVD drive laser to directly pattern interdigitated electrodes for micro-supercapacitors [14]. Others have looked into using 3D printing or inkjet printing as other methods of directly patterning graphene electrodes [30,37,69]. However, the difficulty with these methods is still that the conductive graphene-based inks still require a prior synthesis step of graphene.

Currently, there are several ways to synthesize graphene, typically categorized by bottom-up approaches and top-down approaches. Popular top-down approaches include the use of chemical and mechanical methods to exfoliate graphite or to cleave the sheets, breaking the van der Waals forces that are holding the individual graphene sheets together. Chemical methods, such as the Hummer's method, uses strong acids and oxidizers to form graphite oxide followed by sonication in order to separate the sheets forming GO, which can be later reduced to form rGO, effectively graphene [70,71]. Some mechanical methods like ball-milling or liquid-phase exfoliation with surfactants involve less toxic and hazardous routes of synthesis, but are not quite as effective in producing a high yield or may be energy intensive [70–72]. In terms of bottom-up

approaches, the most common are CVD or the unzipping of carbon nanotubes to form graphene nanoribbons [71]. Yet the challenge with such bottom-up approaches are that they tend to be difficult to mass produce for electrochemical electrodes and thus, are not cost effective.

Interestingly, there are some other scalable bottom-up approaches for the synthesis of porous graphitic carbon material through the pyrolysis of biomass material or certain polymers [73–76]. From this observation, Lin et al. discovered that by using a CO_2 laser that raises local temperatures to above 2000°C, the laser beam can convert PI into a 3D porous graphene film [15]. This finding radically changes the industrial outlook of flexible electronics as well as graphene synthesis since it suggests the possibility of a very effortless and R2R way of preparing graphene films that can be done in a matter of minutes, usable for flexible electronics and as a source of graphene material. Furthermore, the technique of using DLW has a wealth of benefits over other methods as the operational cost is fairly low, without the requirement of masks or expensive equipment. The process is non-contact as well as non-hazardous or toxic with high throughput. [77]

The LIG was found to be useful as interdigitated EDLC supercapacitor electrodes combined with a solid-state electrolyte [15,78] and even as electrodes for the electrodeposition of pseudocapacitive supercapacitor materials, such as MnO_2, FeOOH, and PANI [79]. The electrodes were also found to be useful for water-splitting for the hydrogen evolution reaction (HER) and oxygen evolution reaction (OER) [80] and also for stretchable electronics after the transfer of the LIG film onto polydimethylsiloxane (PDMS) [81]. Non-electrochemical applications were also found for the LIG as a desalination membrane after tuning the LIG for superhydrophobicity [82].

Since the discovery of forming LIG from PI and a CO_2 laser, various other substrates were found to be good precursors for LIG from a CO_2 laser as well, such as wood [55], cloth, paper and food items [54]. Some other polymers could also yield LIG, but would require additional pre-treatment prior to the laser induction [54]. It was found that by adjusting various processing parameters, the resulting LIG properties could be tuned. Specifically, examples of the parameters are laser power, scan speed, depth of defocus, number of laser passes [54] as well as the gases

present at the time of laser induction [83]. The laser power and scan speed affect the spot size of the laser applied and also the residence time of the laser beam on each local area. The depth of defocus also affects the spot size and delocalization of the laser spot while the number of laser passes has an annealing effect on the LIG formed [54]. The atmospheric conditions at the time of laser induction has been shown to influence the hydrophilicity of the LIG due to different functionalization of the surface and edge groups of the formed LIG [83].

So far, researchers have mostly only looked into how to produce more conductive traces with LIG [54], tune its interactions with water [82,84] or other more available precursors for LIG [54,85]. However, it is also very important to control the defectiveness of the graphene and the porosity or surface area of the graphene too. Additionally, there is also interest in probing the uniformity of these films as the bottom of the film in contact with the PI is likely to be of some transitional material between being pyrolyzed and graphitized as opposed to still being an insulating polymer. These unknowns are critical to determine because the viability of using LIG for electrochemical devices involving chemical reactions will depend on the quality of the material as well as their chemical stability for various processes.

It is also of high importance to investigate the control of graphitization and disorder of the structures to obtain material that has a precise surface chemistry for the sake of being able to properly control chemical reactions occurring at the surfaces of the graphene material. This is of particular interest for utilizing the LIG electrodes for sulfur and lithium metal hosts in LiS batteries. As discussed in Section 2.4.2, as a consequence of the short heating time in the sulfur deposition technique, most of the sulfur accumulated in the few larger pores. This can be mitigated possibly by a more uniform pore size distribution centered around mesopores. Additionally, the surface area and quality of the LIG may have affected its suitability as a porous host for lithium metal due to the low efficiency of the electrodeposition step.

But it is of high significance to explore LIG as a porous host for lithium metal in lithium metal batteries or other electrochemical reactions. Compared to graphite as an intercalation host for lithium, graphene was shown to be superior in specific capacity, at least doubling that of

traditional graphite anodes, as well as good cycle stability due to a reduced volume change with the higher surface area. However, the higher surface area as well as points of defects also lead to more side reactions with the organic electrolyte. [86] Although this finding was pertaining to the use of graphene as lithium-ion intercalation anodes, a similar behaviour can also be expected for the use of graphene for the electrodeposition of lithium metal as a host. In light of this, it is crucial to determine ways to modify the density of defects as well as porosity or surface area of the formed LIG, various aspects that will be covered in this chapter.

3.2 Methods

3.2.1 Synthesis of LIG Films and Bulk Powder

Type HN Kapton© (or polyimide, PI) film (127 μm thick) was purchased from McMaster-Carr and used as is without modification as the substrate and precursor of LIG. A BOSSLaser LS-1416 CO_2 laser system with a 50 W tube was used for the patterning of the LIG films and electrodes. After affixing the PI film to the stage of the laser system, a specific set of laser parameters are applied to produce the LIG, as indicated in Table 4, where the power is a percentage of the total power of the laser, 50 W, the number of laser passes is the number of times laser beam passed over the entire pattern again and defocusing is the deviation from the height of focus on the substrate surface. To produce the films, the patterns were induced by the laser in raster scanning mode using the x-swing and all of the laser induction was carried out in atmospheric conditions.

Table 4. Summary of various LIG samples tested

Sample ID	Power (%)	Scan Speed (mm/s)	Number of Laser Passes	Defocusing (mm)
10%-2-0Z	10	30	2	0
10%-2-1Z	10	30	2	- 0.5
10%-2-2Z	10	30	2	- 1.0
9.5%-2-0Z	9.5	30	2	0
9.5%-2-1Z	9.5	30	2	- 0.5
9.5%-3-1Z	9.5	30	3	- 0.5
9.5%-2-2Z	9.5	30	2	- 1.0
9.5%-4-2Z	9.5	30	4	- 1.0

The LIG films were used as is after laser induction and bulk powder was obtained by scraping the LIG film off with a scoopula or razor and collected for characterization and analysis.

3.2.2 Characterization of LIG

The digital images of the electrode cross-sections were obtained by cutting across traces of LIG electrodes to reveal the shape of the cross-section which was then mounted on a 90°sample holder to be viewed under a digital camera. Various lighting levels were used to image the electrodes and verify where the PI/LIG interface was prior to the selection of the final images included in the results section. The images that were chosen and displayed in this thesis possessed a relatively better contrast.

Conductivity measurements were obtained on the LIG films by patterning traces that were 1.6 cm by 300 μm in size with a contact pad of 2 mm by 2 mm at the ends of the traces. These contact pads were then covered by a nickel ink (Nickel Conductive Pen, MG Chemicals) for the purpose of providing a more robust point of contact for the multimeter. The sheet resistance was then calculated by using the following equation:

$$R_s = R\frac{W}{L} \tag{7}$$

Where R_S is the sheet resistance (Ω/□), R is the resistance measured (Ω), W is the width of the trace (equivalent to 300 μm in this case) and L is the length of the trace (equivalent to 1.6 cm in this case).

For the sheet resistance measurements that were conducted for the bulk film, the LIG traces were scraped off using a sharp razor blade such that the remaining LIG was flush with the height of the PI.

Powder X-ray diffraction (XRD) was conducted on the LIG material after the film was scraped off of the PI substrate. The samples were then sprinkled onto a very thin layer of high vacuum grease on a thin PI film (Kapton® Polyimide Film, 0.001" thick, McMaster-Carr) for XRD characterization in a D8 Focus Bruker XRD system. The samples were analyzed between a 2θ of 15° and 50° with an increment of 0.01° and a scan speed of 0.5 sec/step.

To characterize the presence of defects and graphitic regions within the LIG material, Raman spectroscopy was conducted with a Horiba Jobin-Yvon HR800 Raman system equipped with an Olympus BX 41 microscope with a 532 nm laser at 50% laser power (of the 50mW total laser power). The samples were analyzed as specified (as films, scraped off bulk material or partially scraped off material revealing LIG material at a height that is flush with the height of the PI film) and the range of interest was between 1000 and 3000 cm^{-1}. A laser power of 50% was used with an integration time of 10s over three accumulations.

SEM micrographs and EDX mappings were obtained from a FEI Quanta FEG 250 ESEM with EDX. Surface area measurements were conducted using a DVS Advantage Surface Measurement System, between partial pressures of P/P_0 = 0-0.5 using ethanol as the adsorbate.

3.3 Effect of Laser Parameters on Electrode Density, Surface Area and Conductivity

As active material hosts in LiS batteries, LIG electrodes have a number of requirements regarding the electrode density, surface area and conductivity depending on whether it is for the

sulfur cathode or the lithium anode (Table 5). For sulfur cathodes, a high electrode density (low porosity) can be beneficial for the purpose of allowing for a higher level of polysulfide confinement while also leading to a lower use of electrolyte, contributing to a higher energy density. Due to sulfur's insulating nature, a higher electrode surface area would greatly reduce the overpotential involved during cycling as well, and in a related manner, the electrode should also be highly conductive. LIG for the lithium anode, on the other hand, has more options depending on the specific design desired. The density of the electrode should still ideally remain high as a higher porosity electrode leads to a greater void volume of which electrolyte can enter and react with the lithium during plating while also reducing the energy density. A high electrode surface area would be desirable as a host for lithium metal in order that the current densities be reduced during plating and stripping. However, if the LIG host is highly defective, the defects will act as catalytic sites for Li reaction with the electrolyte, vastly reducing the efficiency of the plating. Furthermore, it was shown in an earlier section that the highly porous and non-uniform structure of the LIG led to non-uniform Li plating on the surface. Thus, a slightly lower surface area may be more desirable. Lastly, the LIG should be highly conductive as an electrode for Li metal. Non-conductive hosts have been shown to be beneficial as the lithium plating would occur only where the conductive lithium metal is beneath the surface of the host. The presence of the host then confined the formation of dendritic structures. [87] However, in the instance of a low conductivity host, a more conductive counterpart at the bottom of the film would be necessary for the Li plating to begin there and grow outwards. This in itself is challenging and thus, a highly conductive, thinner electrode acting as a current collector would be more beneficial for Li plating.

Table 5. LIG requirements for use as sulfur and lithium hosts

Property	Sulfur Cathode	Lithium Anode
Electrode Density	High	High
Surface Area	High	Low-Medium
Conductivity	High	High

From the samples tested as presented in Table 4, digital images were captured of the cross-sections to compare the cross-sectional area and shape (Figure 27). It is clear that the samples carried out at 10% laser power (a-c)) possess a significantly larger cross-sectional area in comparison to those done at 9.5% (d-h)), being the dominant contributor to the effect compared to the defocusing or the number of laser passes. The use of a higher laser power corresponds to a higher ratio of protrusion height to the depth of cut (material above and below the PI substrate level). This can be explained by the higher intensity of the 10% power laser beam causing a higher temperature of localized heating compared to the laser beam at 9.5% power. At a higher localized temperature, the carbonization of the PI occurs much more quickly, rapidly releasing gases such as CO_2, CO and N_2 and thus leaving behind larger pores and a larger protruding volume of LIG material. For the samples at 9.5%, the local temperatures are not as elevated and the flux of energy irradiating the PI film is reduced, with a lower flux of gas evolution and thus smaller macropores and a smaller protruding volume. The high flux of gases escaping the carbonizing PI film in the 10% power LIG samples can also explain the more concave cross-sections that are observed in a-c) compared to the almost rectangular or trapezoidal shapes of the lower powered samples in d-h).

Also, generally, it appears that the multiple laser passes and defocusing broaden the width of the cross-sections. For the case of defocusing, Tour's paper demonstrated that the defocusing of the laser beam also broadened the laser spots, leading to wider LIG traces [54]. This is a similar effect with multiple laser passes as well since the multiple passes lead to the laser beam being distributed in a slightly different spot over each pass, an artifact of the laser being a hobby commercial laser and not of a high precision nature.

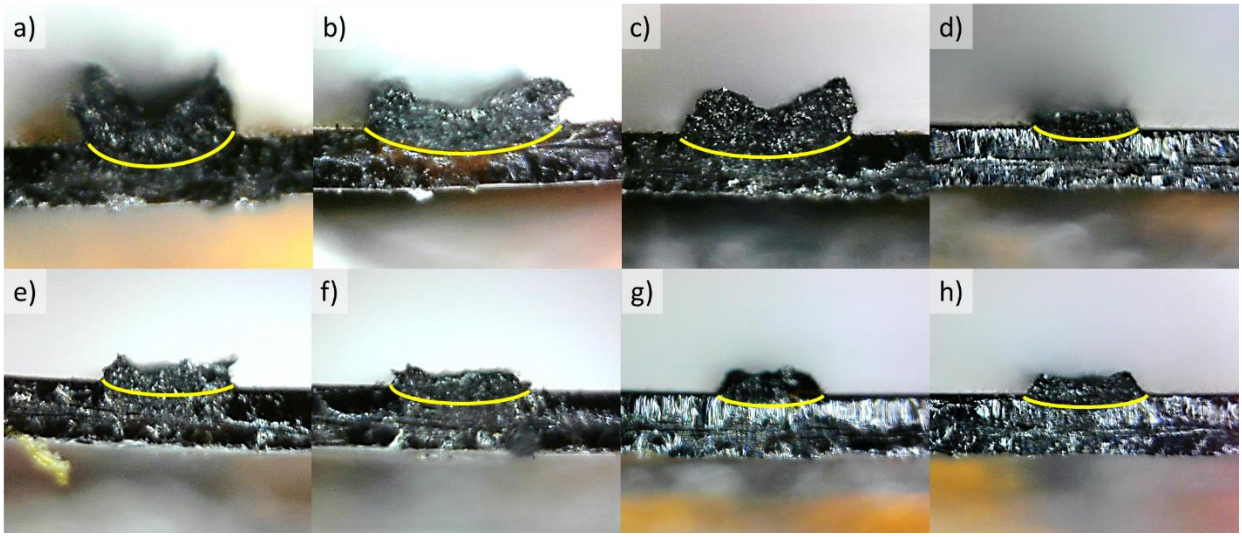

Figure 27. Digital images of cross-sections of various LIG samples as used for conductivity measurements (pattern is 300µm x 1.6 cm) with the following laser parameters: a) 10% power, 0Z, 2 passes, b) 10% power, -1Z, 2 passes, c) 10% power, -2Z, 2 passes, d) 9.5% power, 0Z, 2 passes, e) 9.5% power, -1Z, 2 passes, f) 9.5% power, -1Z, 3 passes, g) 9.5% power, -2Z, 2 passes, h) 9.5% power, -2Z, 4 passes, where a yellow line is used to indicate the interface between the LIG and the PI substrate in each of the images. No scale bar is provided here but the thickness of the PI film is 127µm thick and is thus used effectively as a scale bar.

The surface area of each of these samples was also determined in order for it to be combined with the cross-sectional area for a better idea of how the electrode structure changes in terms of its density and pore sizes (Figure 28). The surface area of the samples conducted at 10% power does not significantly change despite the defocusing present. For all the samples conducted at 9.5% power regardless of the defocus present or the number of laser passes, the surface area is typically equivalent if not higher than that obtained by the higher laser power. Even for the samples in which the surface area is lower than the ~180m^2/g of the 10% power samples (i.e. 9.5% power, 0Z defocusing, 2 passes and 9.5% power, -2Z defocusing, 4 passes), the electrode clearly contains pores that are much smaller, resulting in an electrode with a significantly smaller cross-section. Of the samples tested, the sample with the highest surface area is the sample at 9.5% power, -1Z defocusing and 3 laser passes, yielding a surface area of almost 250m^2/g. At a cross-sectional area that is about 1/3 of that belonging to the samples at 10% laser power, this places

this particular set of parameters to be yielding LIG with the highest electrode density and surface area, at least of the samples tested.

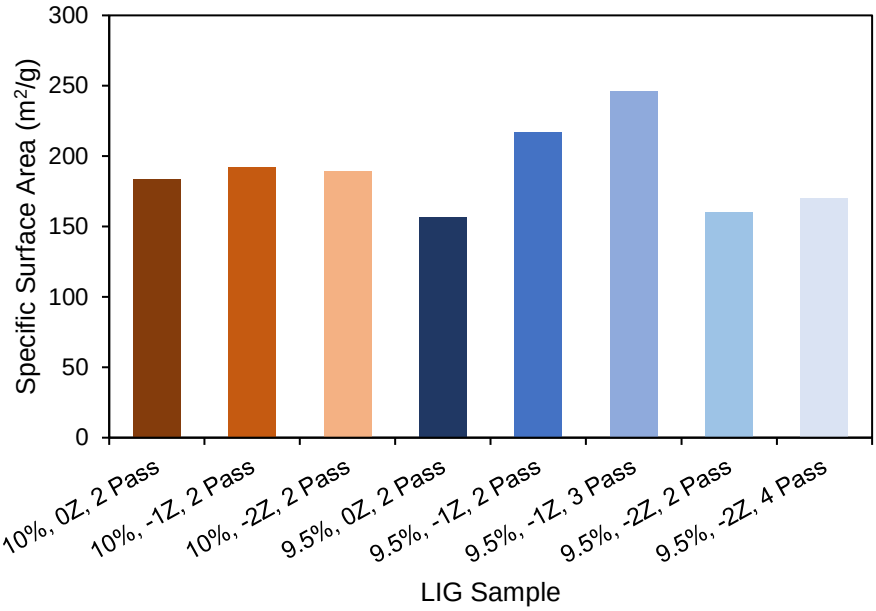

Figure 28. Specific surface area obtained through ethanol adsorption on the various LIG samples tested

Although the samples irradiated at a lower laser power yielded denser electrodes, it should also be noted that the low laser power reduces the total laser irradiation received compared to the samples at the otherwise equivalent laser parameters. This is expected to generally result in a lower conductivity as seen in Figure 29. Two sets of measurements were obtained for the LIG samples, the first being a neat film of LIG and the latter being from the protruded half of the LIG material scraped off, measuring the resistance of the residual film. As predicted, the samples at the lower laser power resulted in generally lower resistances, though multiple lasing from defocusing and number of laser passes certainly appears to reduce the sheet resistance so that it is comparable to that of the 10% laser power samples. This effect is confirmed for both sets of measurements obtained.

Another major observation is the vast difference between the sheet resistance of the neat film and the partially-scraped film, where the sheet resistance of this set of data is displayed on the secondary y-axis in a log scale. The reduction in conductivity after the protruded material has

been removed can suggest an inhomogeneity within the film across the vertical dimension from the top of the film towards the bottom near the PI substrate. This may be because the top of the film being closer to the laser beam also absorbs more of the laser irradiation. As a result, the LIG at the top of the film becomes more annealed, less amorphous and thus more conductive. When the material at the top of the film becomes removed, the conductivity is thus greatly reduced due to the lower degree of carbonization and graphitization of the material underneath. Should this postulate be true, a change in the defectiveness of the LIG in the bulk material should be observed possibly through a number of laser passes as the effect of multiple lasing has been shown to reduce the resistivity in both the top of the film and the partially scraped samples.

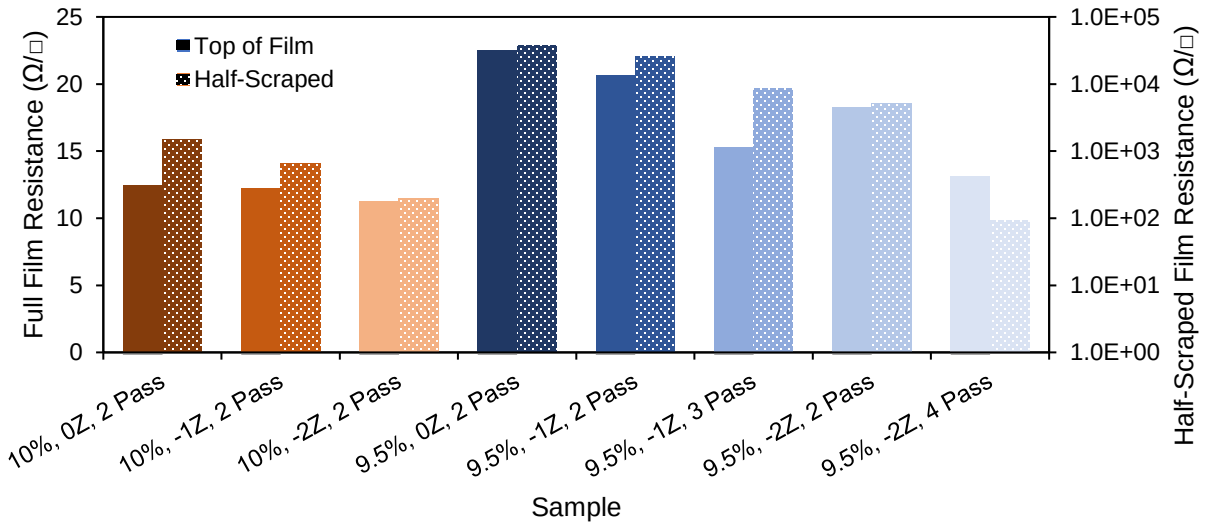

Figure 29. Sheet resistance measured for the LIG samples tested, conducted for both a neat film and also a film with the protruded material scraped off

3.5 Top of Film vs Bulk Properties

To further probe the differences in the top of the LIG film and the bulk LIG material, several analyses were conducted. The first was to observe the change in the D, G and 2D peaks at different regions of the LIG film. At the top of the neat film, the rastering of the laser beam leaves behind regions that are more protruded due to a higher intensity of the focused region of the parabolic beam and regions that are less protruded due to a lower intensity in the parabolic distribution of

the beam. Not surprisingly, the LIG here experience structural differences characterized by the inconsistent I_D/I_G ratio that decreases from the valley to a minimum at the peak of the LIG film (Figure 30a,b) from iii) to ii) and then i)). And to confirm the observation of a reduced conductivity in bulk material, iv) shows a significant broadening of the D and G peaks due to the presence of a highly amorphous and defective carbon structure. The 2D peak in this spectrum is also non-existent, suggesting that this material in the bulk is not truly graphene, but a transitional material between PI and LIG. Figure 30c) also indicates distinct difference in the presence of oxygen from the bottom of the LIG film to near the top through EDX mapping. This possibly implies that many of the oxygen containing groups have not been removed to form CO_2 and CO gas closer to the bottom of the film. This is then consistent with the Raman data that there are small and few crystalline regions of graphite and graphene in the bulk of the film and this only increases and grows towards the top of the film under an increased laser exposure.

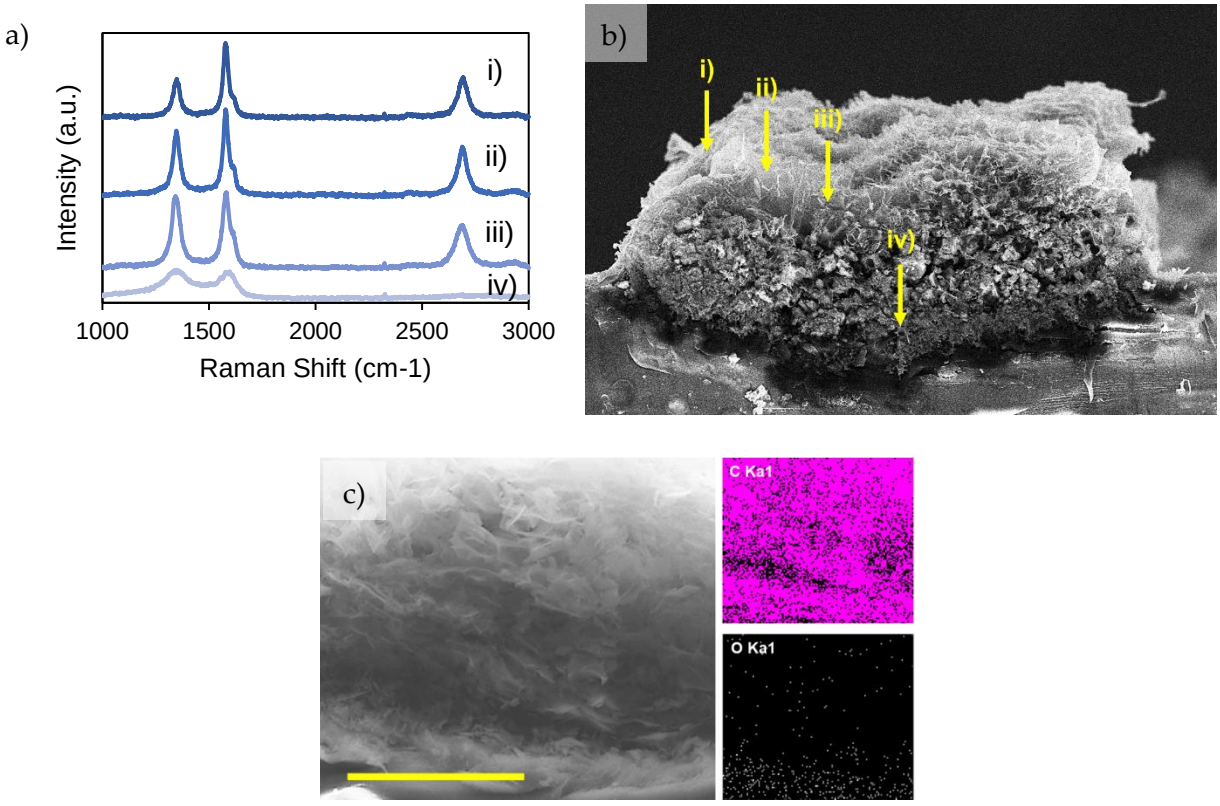

Figure 30. a) Raman results of the LIG at different heights of the film corresponding to i) the peak, ii) the mid region and iii) the valley; b) SEM micrograph illustrating the points of Raman data collection in a); c) EDX mapping of cross section over a long collection period, scale bar = 30 µm

Due to the observed inhomogeneity from the initial Raman characterization, it was decided that for the purpose of examining the possible annealing effect of the number of laser passes, the partially scraped film should be analyzed, as the top of the film is non-representative of the entire film while the completely scraped off LIG material would contain a mix of both material from the top of the film and very amorphous bulk material. For a more statistically relevant data set, five sampling points were taken of each sample from 1 laser pass to 5 and represented in Figure 31 as the 'X' markers while the average is indicated by the line. From Figure 31a), the full width half maximum (FWHM), indicator of the uniformity of the material, is seen to moderately decrease for the D, G and 2D peaks as a function of the number of laser passes, although this is the most noticeable from the first to third laser passes, while the change is less significant in the fourth or fifth laser passes.

Along with the reduced FWHM, the ratio between the D and G peaks and the G and 2D peaks are also expected to decrease as a low I_D/I_G ratio is indicative of a reduced region of sp^3 amorphous material and an increased graphenic region. A lower I_G/I_{2D} ratio, on the other hand, points to a presence of fewer graphene layers. Similar to the trend observed with the FWHM and lasing, Figure 31b) suggests an improvement in the graphene structure only up until two or three laser passes, while beyond that, the ratios remain on average the same. While there are instances of the average FWHM of the D peak increasing at 2 passes and the average FWHM of the G peak increasing at 4 passes, this may just be a fact of significant variation within the data.

XRD was conducted on the bulk, scraped off LIG film to detect any changes in graphitization of the material as a whole resulting from the laser passes (Figure 32). There is a fairly low signal-to-noise-ratio (SNR), most likely due to the fact that the majority of the bulk material is non-graphitized and still amorphous. However, from what is observable from the graphite peak around $2\theta = 26°$, there is an increase in the peak intensity from the first laser pass to the second and from the second laser pass to the third, there is a reduction in the broadening of the peak. Yet congruous to the Raman data, the XRD spectra for the fourth and fifth laser passes do not suggest any substantial improvement in the peak intensity or FWHM.

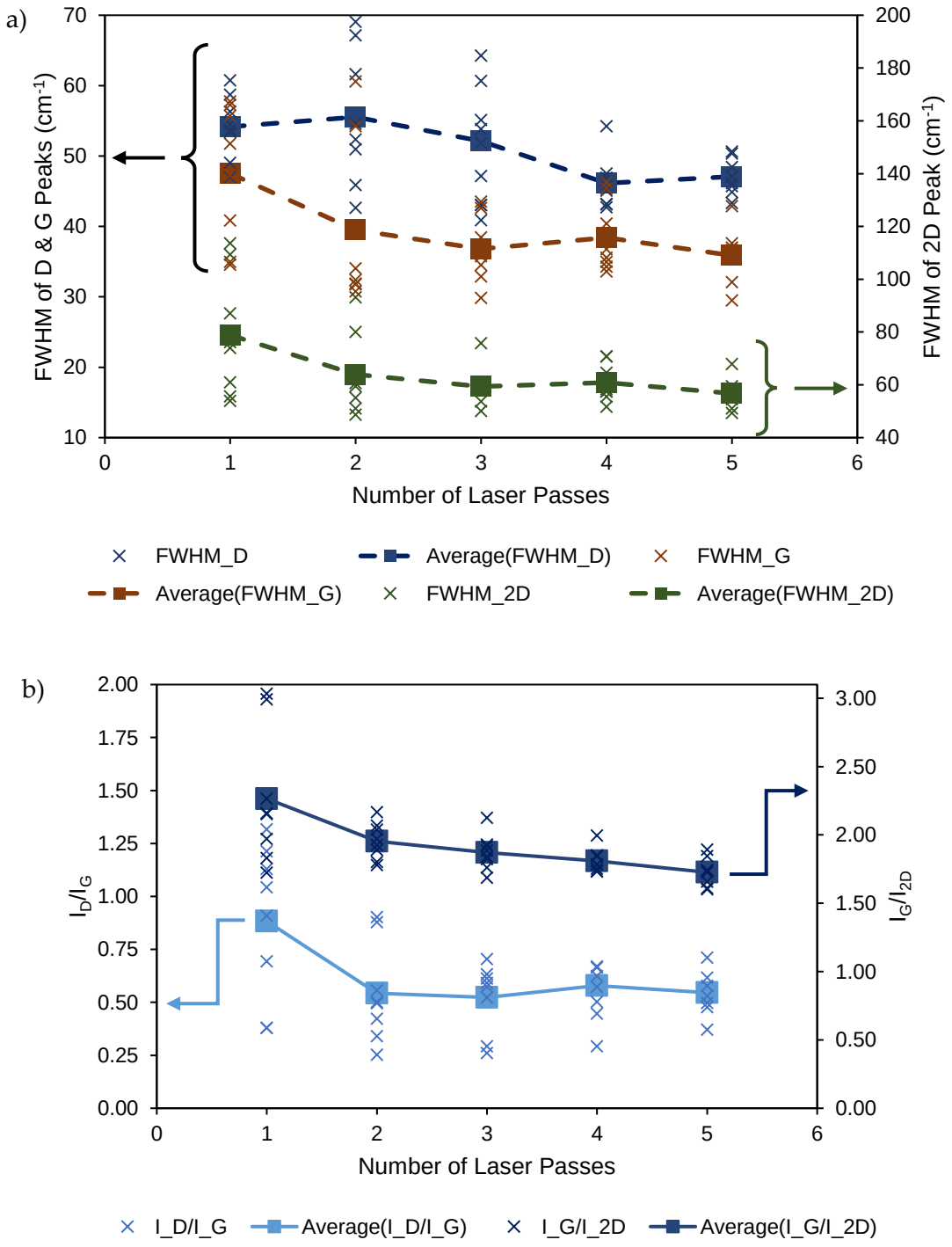

Figure 31. Raman results displaying a) the FWHM of the D, G and 2D peaks and b) the I_D/I_G and I_G/I_{2D} ratios as a function of the number of laser passes for the partially scraped LIG samples

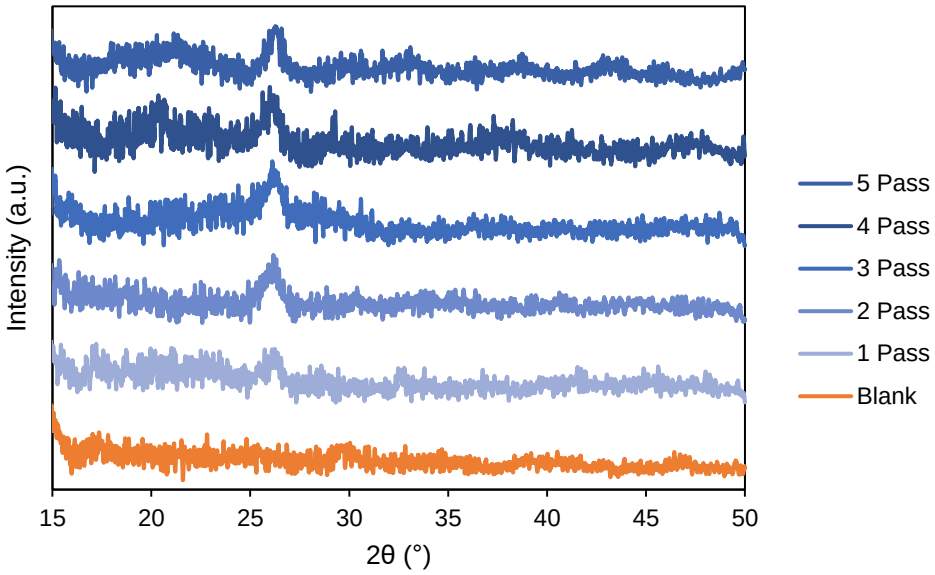

Figure 32. Powder XRD results for the bulk LIG material as a function of the number of laser passes with PI and high vacuum grease as the blank

From the characterization conducted on the LIG material, it appears as though there is little significant change in the material in terms of the graphitization or the defectiveness after approximately 3 laser passes. A potential explanation for the observed trend across the data is that the laser power is not sufficient to reach past a certain height of the LIG film, after having been partially absorbed by the existent LIG. The CO_2 laser is capable of annealing the LIG film to convert more of the amorphous carbon into sp^2 carbon with each subsequent pass of the laser. However, the specific power and energy of the laser beam is also critical to determine whether the defects are reduced or if the present material is ablated through oxidative etching [88]. Thus, more study will be required to determine the proper laser parameters to properly convert more of the film to become more graphene-like.

3.6 Conclusion

Based on the present findings in this chapter, LIG as a new material is quite promising with many applications that have been published and many more that are likely to be discovered. However, there are still critical challenges with the material that will need to be addressed in future work in order to utilize LIG to its full potential within electrochemical systems.

LIG films were discovered to be rather inhomogeneous in the vertical dimension from the top of the film to the bottom. Thus, it was discovered that most of the desirable LIG properties (i.e. conductive films, low defectiveness, higher sp^2 regions, graphitic nature etc.) observed are likely present mainly at the top of the LIG films closest to the laser source upon application. Laser irradiation at 9.5% power was shown to produce denser films with a higher surface area to volume ratio but suffered from lower electrical conductivities that can be improved upon multiple lasing by the number of laser passes or defocusing. However, multiple laser passes do not appear to significantly improve the graphitic property or defectiveness of the LIG films beyond 2 or 3 laser passes.

While the laser parameters used in Chapter 2 for the LSFB (10% power, no defocusing, 2 laser passes) had worked for the proof of concept, as previously mentioned, it did not yield the most suitable set of parameters for the anode and cathode. In light of the discoveries in this chapter, the more ideal laser parameters for the LSFB likely come from using 9.5% as the power at 0.5 mm defocusing and 3 laser passes for use as a sulfur cathode due to its denser pore structure, high surface area and lower sheet resistance. For the lithium anode, 9.5% power at 1.0 mm defocusing and 4 laser passes yields a LIG electrode structure that possesses a dense pore structure with a medium surface area and a lower sheet resistance. With the higher number of laser passes in these sets of parameters, the LIG will be graphitized and annealed as much as possible, according to the parameters studied.

However, it is highly suggested that more experiments be conducted to further control the carbon structure of the LIG. For example, it would be ideal to control the “hardness” or “softness” of the carbon relating to the sp^3 and sp^2 regions of the carbon through other parameters such as

irradiation gas conditions or pre-treatments. Such control as well as being able to make more homogeneous films would further make the DLW of LIG an appealing platform for more flexible electrochemical devices in the future.

4.0 Lithium Plating on Hard vs Soft Carbons

4.1 Motivation of Study

Lithium metal has been a very attractive choice as an anode in electrochemical cells due to its very high theoretical capacity (3860 mAh/g) and low density which can contribute to an overall higher specific energy density in a full cell [50]. Additionally, it has a very low reduction potential, enabling it to work very well as an anode material. However, using lithium metal as anodes have a number of challenges as well (Figure 33). Lithium metal is extremely reactive to water and oxygen, but also to organic electrolytes, which are necessary for the operation of the battery, forming a SEI. The presence of an SEI is crucial to protect the Li metal from further reactions with the electrolyte, however, the films are often unstable due to the effectively infinite volume change of the metallic anode, resulting in the need for forming more SEI, depleting the Li as well as the electrolyte. Despite having an SEI, as Li is highly reactive and this protection layer is not perfect and is sensitive to cracking, Li metal anodes suffer from a low coulombic efficiency. Additionally, Li metal has a tendency to plate in a dendritic manner, causing short circuits over many cycles as well as the formation of a highly diffusion limited, porous layer of dendrites that can break off, leaving behind a dead Li layer.

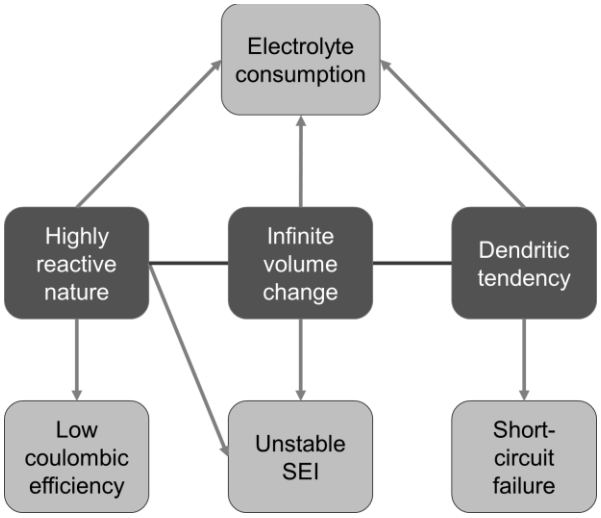

Figure 33. Summary of the challenges with lithium metal anodes and recent developments

A variety of techniques have been employed to try to resolve the challenges with Li metal so that it can replace Li-ion battery anodes, due to the better energy density. Simple electrolyte additives have been found to reduce the surface energy of the electrolyte and metal and also aid the formation of more stable SEI [42,49,89,90]. Researchers have also found ways to add an artificial SEI, through polymers or hybrid ceramic materials that can be tuned to have mechanical properties ideal for the prevention of reaction with electrolyte or the formation of Li dendrites at the surface [90]. Other strategies involve the pre-patterning [91] or seeded growth [44] of the Li metal which can provide sites for the formation of more stable, directed, metallic crystals as opposed to a random growth of dendrites.

Of the many methods published in literature, the ones most of interest to the reduction of excess Li metal involve the pre-lithiation of an anode material or the use of a host for Li [49,89]. Most of the Li metal batteries presented involve the employment of a thick piece of Li metal, with excesses of beyond 300% of stoichiometric Li (with respect to the active material present in the cathode) due to the highly reactive nature of Li as well as the expectation of the formation of an unusable, dead Li layer. However, with the use of a pre-lithiated anode material, preferably one with a high Li capacity, such as silicon [92,93], the volume change is reduced with respect to the otherwise infinite volume change of elemental Li metal. Unfortunately, the use of pre-lithiated anodes also come with a wealth of other challenges, such as the necessity for high precision control of the amount of lithiation to avoid lithium plating onto the electrode, which would nullify the benefits of the lithium host [94].

The benefit to using conductive hosts for Li metal is that the local current densities in the anode can be reduced, which has been shown to reduce the local overpotentials leading to dendritic, mossy Li plating. Additionally, as Li will plate into the host, the volume change is also greatly reduced, forming more stable SEI films. Carbon materials are common host materials as they possess low density, good mechanical strength as well as high surface areas. Some common carbon host materials include rGO, graphene, CNT and carbon fiber. [95] A vacuum filtrated GO membrane was found to simultaneously reduce while wicking molten Li between the layers through reactive-wetting for a stably cycling anode [66]. While another report proved that the use

of an ALD "lithiophilic" coating of ZnO could allow for the wetting of molten Li into the pores of a porous host [96]. As most carbon materials were found to be lithiophobic [66,96], molten Li cannot easily be used to impregnate a carbon host. Thus, electrodeposition is most commonly used to introduce Li metal into carbon [95].

For the plating and stripping of Li metal, a carbonate-based electrolyte is found to be the most efficient, such as 1:1 EC/DMC with 1M $LiClO_4$. However, for the cycling of LiS batteries, an ether-based electrolyte, such as 1M LiTFSI in 1:1 DOL/DME, is more commonly used for the cathode. This is because the carbonate solvents would irreversibly react with intermediate polysulfide species during cycling. [97] It is then of interest to consider in what kind of electrolyte might a non-infinite Li anode cycle most stably in after its electrodeposition. Furthermore, it is known that the defects in carbon materials tend to be centers of high chemical reactivity [98,99], which suggests that the specific structure of the carbon material will play a very large role in its chemical stability as a conductive host for the Li anode. To date, there has not been a study comparing the efficiency of Li plating on ordered, graphitic carbon versus disordered, amorphous carbon as well as the effect of electrolyte and salt on the carbon. In this chapter, 1:1 DOL/DME and 1:1 EC/DMC will be compared as solvents for the electrolytes with 1M $LiClO_4$ and 1M LiTFSI as salts in terms of the provided cycle stability and coulombic efficiencies in Li plating and stripping on graphite and a hard carbon from carbonized poly(furfuryl alcohol) (PFA) as substrates.

4.2 Method and Characterization

4.2.1. Synthesis of Carbonized Poly(furfuryl alcohol)

The procedure outlined by Yao et al. [100] was adapted for the synthesis of colloidal microporous carbons from furfuryl alcohol (FA; 98%, Sigma Aldrich). A two-step polymerization was used based on the stabilization of FA oligomers through the use of an amphiphilic triblock copolymer (Plurionic F127, $EO_{106}PO_{70}EO_{106}$, MW 12600, Sigma Aldrich) followed by the growth of the spherical polymers using H_2SO_4. For the first step, FA, F127, ethanol, water and HCl were

used with the weight ratio, 1:1:6:2:0.17. The solution was added to a capped vial and left to react at 70°C under stirring overnight. After the initial oligomer formation, the PFA solution is added to a new beaker uncapped along with 8.55 M H_2SO_4 (where 2.4 mL of 98% sulfuric acid is mixed with 2.6 mL of DI water) at a 2:1 ratio of PFA solution to H_2SO_4 solution, under stirring at 90°C for one hour. This step is to allow for the evaporation of water and ethanol while growing the PFA spheres.

After fully polymerizing, the spheres are rinsed with DI water and centrifuged and then dried overnight at 70°C. When the polymer was dried, it was carbonized in a tube furnace (diameter of 5.5 cm, Carbolite Gero STF) under high purity Ar gas flow, with a ramp rate of 10°C/min to 200°C for two hours, followed by a ramp rate of 10°C/min to 1100°C for a full carbonization, held for five hours. At the end of the heating, the tube and polymer were left to slowly cool by resting within the tube furnace until reaching room temperature.

4.2.2. Preparation of Electrodes

Two types of electrodes were prepared using a spray coating method: artificial graphite-based electrodes and also carbonized PFA (CPFA) electrodes. Lastly, for comparison, copper foil (50.8 μm thick, McMaster-Carr) electrodes were used for the testing of different electrolyte compositions as well. The same copper foil was used as the substrate for the spray coating of the graphite and CPFA electrode material. Graphite (artificial graphite powder, MTI XTL) or CPFA (as synthesized) were added at 70 wt% to 20 wt% conductive additive (TIMCAL Graphite & Carbon Super P® Conductive Carbon Black, MTI XTL) and 10 wt% poly(vinylidene fluoride) (PVDF, MW = 534,000, Sigma Aldrich), totalling to 100 mg of material, and 3 mL of N-methyl-2-pyrrolidone (NMP) (99%, Sigma Aldrich). The electrode material (graphite or CPFA), PVDF, Super P® and NMP were sonicated in a bath sonicator (360 W, 40 kHz) for 25 min and then used in a spray coater. The substrate was heated to 130°C for a rapid evaporation of the solvent as multiple, thin coats were deposited using the spray coater. After the electrode material was fully

dried, all electrodes (graphite, CPFA, copper) were cut into discs with a diameter of 7/16". The final obtained loading of graphite or CPFA on the electrodes was approximately 0.3 mg/cm^2.

4.2.3. Cell Assembly

The spray coated and cut electrodes were moved into an argon-filled glovebox with H_2O and O_2 levels below 1 ppm. The graphite, CPFA or copper electrodes were used as the working electrode and the counter electrode was a piece of lithium ribbon (diameter = 0.625", thickness of ~0.5 mm, Sigma Aldrich). CR2032 stainless steel cell casings, pans and spacers were used as is from MTI XTL and pressed at 1000 psi to crimp the cells. Celgard© membrane was used as the battery separator (25 μm thickness, pore size of 0.21 x 0.05 μm, MTI XTL) and 90 μL of a specific electrolyte was used. Four electrolytes were tested, comprised of either ethylene carbonate (EC, anhydrous 99%, Sigma Aldrich)/dimethyl carbonate (DMC, anhydrous >= 99%, Sigma Aldrich) or 1,3-dioxolane (DOL, anhydrous 99.8%, with ~75 ppm BHT as inhibitor, Sigma Aldrich)/1,2-dimethoxyethane (DME, anhydrous 99.5%, Sigma Aldrich) and 1M of lithium perchlorate ($LiClO_4$, 99+%, Acros Organics) or lithium bis(trifluoromethanesulfonyl)imide (LiTFSI, 99.95% trace metals basis, Sigma Aldrichs): 1M $LiClO_4$ in 1:1 EC/DMC (F1), 1M LiTFSI in 1:1 EC/DMC (F2), 1M $LiClO_4$ in 1:1 DOL/DME (F3) and 1M LiTFSI in 1:1 DOL/DME (F4). The samples prepared are denoted as follows in Table 6.

Table 6. Samples tested for Li plating experiment

Sample Name	Material	Salt	Solvent
G1F1	Graphite	$LiClO_4$	1:1 EC/DMC
G2F2	Graphite	LiTFSI	1:1 EC/DMC
G3F3	Graphite	$LiClO_4$	1:1 DOL/DME
G4F4	Graphite	LiTFSI	1:1 DOL/DME
P5F1	CPFA	$LiClO_4$	1:1 EC/DMC
P6F2	CPFA	LiTFSI	1:1 EC/DMC
P7F3	CPFA	$LiClO_4$	1:1 DOL/DME
P8F4	CPFA	LiTFSI	1:1 DOL/DME
C9F1	Copper	$LiClO_4$	1:1 EC/DMC
C10F2	Copper	LiTFSI	1:1 EC/DMC
C11F3	Copper	$LiClO_4$	1:1 DOL/DME
C12F4	Copper	LiTFSI	1:1 DOL/DME

4.2.4. Material Characterization

For the characterization of the graphite and CPFA, Raman analysis, powder XRD, SEM and EDX were conducted. Raman analysis was carried out with Horiba Jobin-Yvon HR800 Raman system equipped with an Olympus BX 41 microscope with a 532 nm laser at 50% laser power (of the 50mW total laser power), conducted between the range of 1000-3000 cm^{-1}. XRD was carried out with a D8 Focus Bruker instrument between the range of 2θ = 15-50° and SEM was conducted with FEI Quanta FEG 250 ESEM with EDX under scanning electron mode.

4.2.5. Electrochemical Characterization

The cells were tested using galvanostatic cycling with a Neware BTS 3000 instrument (5V, 1 mA) and a Bio-Logic SP-300 potentiostat was used for conducting EIS between 5 MHz and 100 mHz in the potentiostatic mode.

For the graphite and CPFA cells, the electrodes were first discharged and charged at 0.1 C between 0 and 1 V five times first to generate stable SEI relating to volume expansion due to the intercalation of lithium ions.

All cells were then ready for 50 plating and stripping cycles at a plating density of 0.1 mA/cm^2 where plating occurred for 2 hours and stripping until 0.1 V. EIS was conducted at the 1st, 2nd, 3rd, 4th, 5th, 10th, 20th and 50th cycles in order to probe the changes in the electrode. To analyze the EIS data, the following equivalent circuit was used, as per [101]:

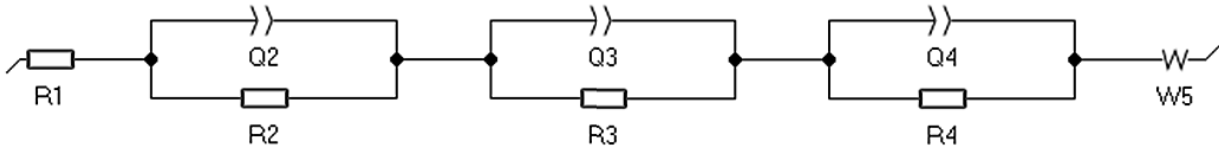

Figure 34. Schematic of the equivalent circuit for EIS analysis of Li plating cells

Here R1 is the resistance found in the electrode components, Q2 and R2 are the constant phase element (CPE) and resistances corresponding to the surface film or SEI in the electrode, Q3 and R3 are the CPE and resistances corresponding to the bulk of the electrode, Q4 and R4 are the CPE and resistances corresponding to the double layer capacitance and charge transfer resistances, respectively and lastly, W5 is the Warburg impedance present in the system.

4.3 Results

4.3.1 Structural Characterization of Graphite vs CPFA

To probe the structural differences in the two carbon materials, Raman spectroscopy and XRD was carried out on the graphite and CPFA powder. Figure 35 shows the Raman and XRD results. From the Figure 35a), the spectrum of the CPFA is characterized by a wide and high intensity D peak at ~1340 cm^{-1} with a slightly more narrow G peak at ~1585 cm^{-1} but equally intense, while lacking a well-defined 2D peak. This suggests a presence of sp^2 carbons by the G peak, while a large amount of sp^3 carbons as well, due to the amorphous structure of randomly

organized layers of sp^2 carbon. The graphite spectrum, on the other hand, shows a much smaller D peak at ~1350cm^{-1}, resulting from a smaller amount of defects with the layered structure and the defects may be from the edges of the graphite layers. The sharp, narrow G peak at ~1580cm^{-1} points to the highly ordered sp^2 regions within the graphite with there being several layers of graphite shown by the broad and relatively low intensity of the 2D peak around 2700 cm^{-1}.

The amorphous nature of the CPFA is further verified through XRD. A typical graphite peak corresponding to the (0 0 2) diffraction line [102] is expected around 26°, which is very clearly seen in the graphite spectrum, but is not seen at all in the CPFA spectrum, where there are no distinguishable peaks, like the Kapton used for the blank. There are also very small peaks at 42.5° and 45°, corresponding to the (1 0 0) and (1 0 1) diffraction lines as well in the graphite [102].

Due to the differences in structure between the highly ordered, soft carbon, graphite and the amorphous, hard carbon, CPFA material, it is expected that their lithiation and delithiation would occur differently as well as their behaviour as lithium electrodeposition substrates.

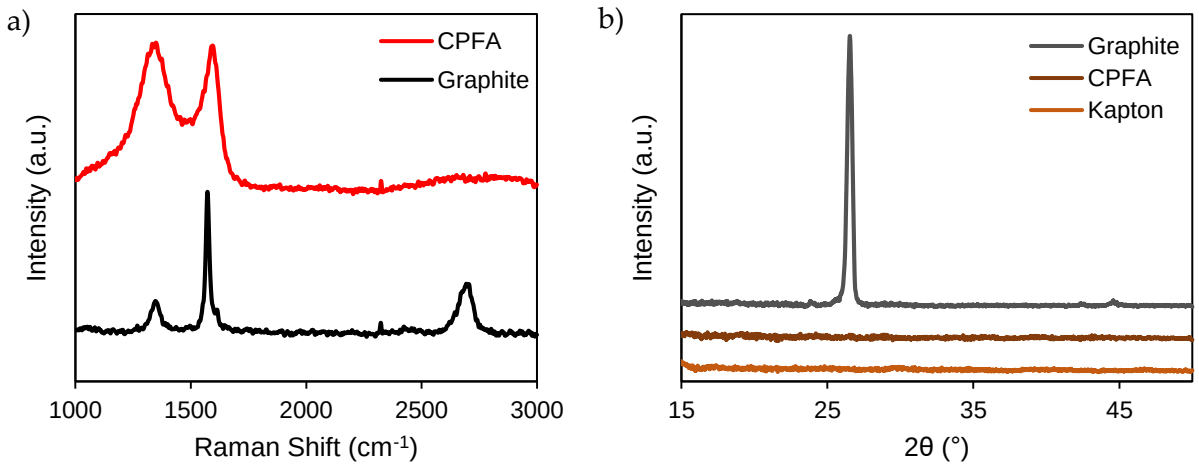

Figure 35. a) Raman and b) XRD spectra of CPFA vs graphite used in the plating study

4.3.2 Electrochemical Results

Lithiation of carbon materials involve the formation of various Li_xC_y structures until the carbon is fully lithiated at LiC_6 [103]. The specific shape of the voltage curve as well as the

presence of plateaus and tails can be used to analyze the kinetics and mechanisms of Li insertion within graphite and CPFA. The first lithiation voltage curves for graphite and CPFA in the various electrolytes tested can be seen in Figure 36, where the solid lines represent the carbonate-based electrolyte and the dashed lines represent the ether-based electrolyte. SEI formation typically occurs around 0.5 – 1.0V and for the graphite anode, a plateau is seen quite clearly for all four electrolytes. For CPFA, the SEI formation shoulder in the voltage curve is not obvious with the exception of the electrolyte with 1M LiTFSI in 1:1 EC/DMC. The SEI formed during this stage is a film along the edges of the graphite layers in an attempt to passivate these sites of lithiation/delithiation from further reaction with the electrolyte in latter cycles.

Apart from the plateau for SEI formation, several other plateaus are typically formed to indicate different Li_xC_y structures formed, such as Li_xC_{32} around 0.2 – 0.12 V, Li_xC_{12} around 0.1 – 0.075V and LiC_6 after 0.075 V until 0 V [103]. However, the definition of these particular plateaus may not be clear, depending on what else may be occurring within the carbon particles. For example, for F3, representing 1M $LiClO_4$ in 1:1 DOL/DME, with graphite, the voltage curve does not have distinguishable plateaus between 0.5 – 0 V and are just characterized by one plateau or slope. This indicates the presence of Li-solvent co-intercalation, which has been well documented for ether-based electrolytes such as the one used here [104,105]. While the graphite samples all notably otherwise possess various plateaus for the Li_xC_y structures formed during lithiation, the CPFA samples do not possess such a variety of plateaus. This is due to the lack of order and generally amorphous nature of the hard carbon material, leading to a non-uniform lithiation of the carbon as opposed to the layered structure lithiation of graphite [106].

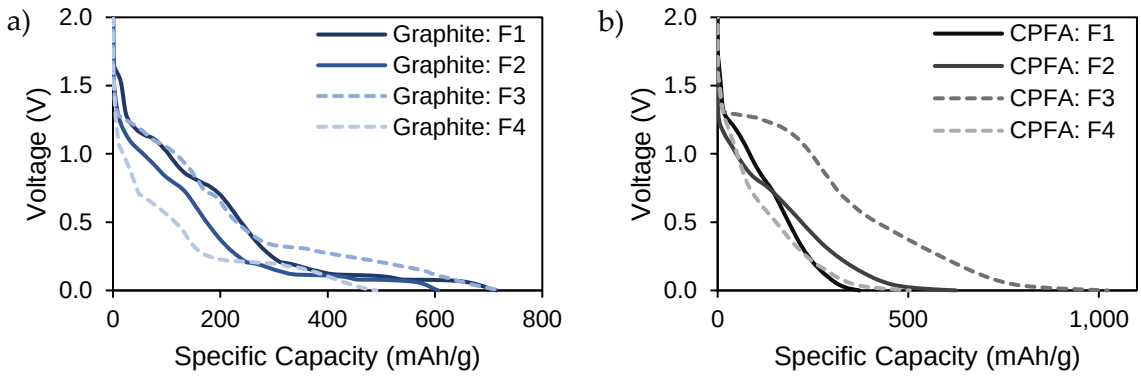

Figure 36. First lithiation curves for a) graphite and b) CPFA in various electrolytes, where F1 = 1M $LiClO_4$ in 1:1 EC/DMC, F2 = 1M LiTFSI in 1:1 EC/DMC, F3 = 1M $LiClO_4$ in 1:1 DOL/DME, F4 = 1M LiTFSI in 1:1 DOL/DME

The stability of the carbon anode can be observed through any hysteresis and changes in the obtainable capacity as well as the voltage curves (Figure 37). Graphite within a carbonate-based electrolyte (Figure 37a)) is gradually lithiated in stages as seen in the first lithiation curve. When the graphite is delithiated, various plateaus of delithiation stages are observed as well. Though the next lithiation cycle is much lower in capacity, the same plateaus are still present and the obtained capacity is similar to the expected theoretical capacity of 375 mAh/g. This suggests a stabilized SEI formed in the first cycle with its high irreversible capacity. The second delithiation shows little to no hysteresis with the first. In an ether-based electrolyte, though there is little to no hysteresis of the delithiation curves (Figure 37b)), it is clear that the lack of plateaus present as well as the significantly reduced capacity of under 100 mAh/g points to a damaged structure that leads to a lithiation more akin to the CPFA curves in c,d).

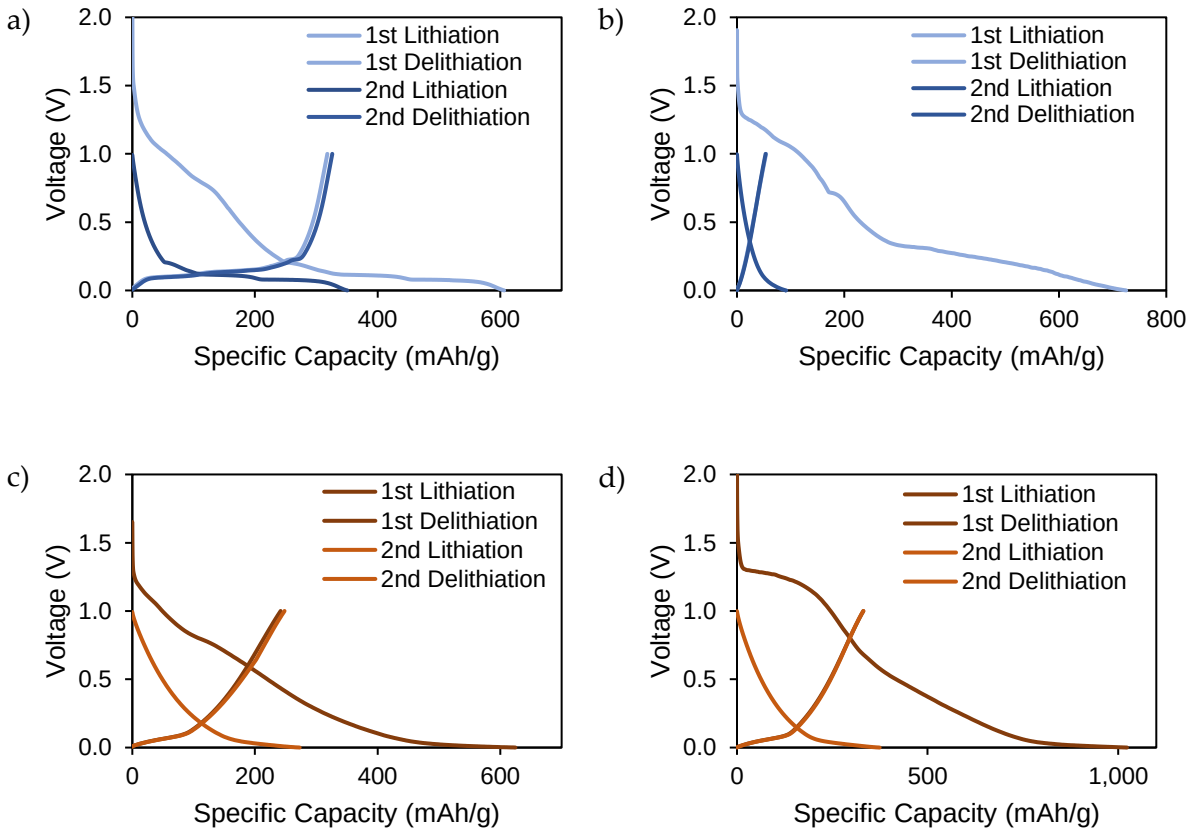

Figure 37. First and second lithiation cycles for a) G2F2, b) G3F3, c) P6F2 and d) P7F3

The lithiation/delithiation curves for CPFA in carbonate-based electrolyte indicate a large irreversible capacity in the first cycle due to the formation of SEI, but the subsequent cycle is rather stabilized around 300 mAh/g, which is lower than the theoretical capacity of graphite, but shows good reversibility. In an ether-based electrolyte, CPFA exhibits the highest irreversible capacity in the first lithiation of beyond 1000 mAh/g. This possibly points to a large portion of lithium-solvent co-intercalation resulting in the long tail of the voltage curve. Interestingly, the second lithiation and delithiation cycle indicates a capacity of 330 mAh/g, which is close to the theoretical capacity while also being stably so. This behaviour is different from that of the graphite anode in the same electrolyte, which suggests that the solvent co-intercalation capacity of CPFA may be higher but does not lead to an electrode that is quite as damaged as that of the graphite material.

The EIS results of select samples G2F2, G3F3, P6F2 and P7F3 are shown in Figure 38. Across G3F3 and P7F3, both samples with an ether-based electrolyte, very large impedances for the surface film, bulk electrode and charge-transfer resistances are observed after the five lithiation and delithiation cycles. This is significantly larger than those for the carbonate-based electrolytes (G2F2, P6F2). This can be attributed to the breaking up of the structure of both the graphite particles and CPFA particles from solvent exfoliation by the ether electrolyte. After the sheets are exfoliated and particles damaged, the lithium ions are delithiated to a voltage of 1V and the remaining carbon electrode is left with thick SEI and high contact resistance between the particles. As previously observed from the lithiation/delithiation voltage curves, the carbonate-based electrolytes did not co-intercalate into the electrodes but developed a stable SEI allowing for a low hysteresis cycling of the electrode.

All of the samples also experience a higher impedance after the first plating and stripping cycling of lithium, which is then reduced in the next few cycles before increasing as the plating and stripping continues. This phenomenon is also observed in symmetric Li vs. Li cells where the initial surface area of the Li metal anode is rather low, leading to a high flux of Li ions out of the metal anode, resulting in higher impedances. After a number of plating and stripping cycles, the surface area of the anode gradually increases due to the natural tendency of lithium plating and thus the impedance reduces. [107] This behaviour is also likely behind the observed decrease then increase in impedance with the cycle number, however in the case of G3F3, after the decrease in impedance, there is no further increase in impedance which is probably due to the exfoliation of the sheets as previously explained.

There are also differences between samples with the two different solvent-based electrolytes. For carbonate-based electrolytes, if the structure of the graphite or CPFA particles are relatively stable with the plating and stripping as well partial re-lithiation (as the stripping of the metallic lithium occurs to 0.1V), the thickness of the SEI layers are expected to grow to accommodate for the volume and structural changes in the metallic lithium that is plated and stripped away. Accordingly, the impedance of the SEI layer should increase with the number of cycles (for both a) and c)), which is what is generally observed when comparing the spectra

between the 1st, 10th, 20th and 50th plating cycles. On the other hand, due to the constant re-exfoliation of the layers within the graphite and CPFA particles by the partial re-lithiation in the ether-based solvent, SEI layers are expected to form on the newly exposed edges and surfaces of the carbon particles. Thus, the thickness of the SEI layers may not necessarily thicken, but merely that there would be more surfaces to form SEI on, hence a similar impedance is observed over the course of cycling in the spectra for both b) and d).

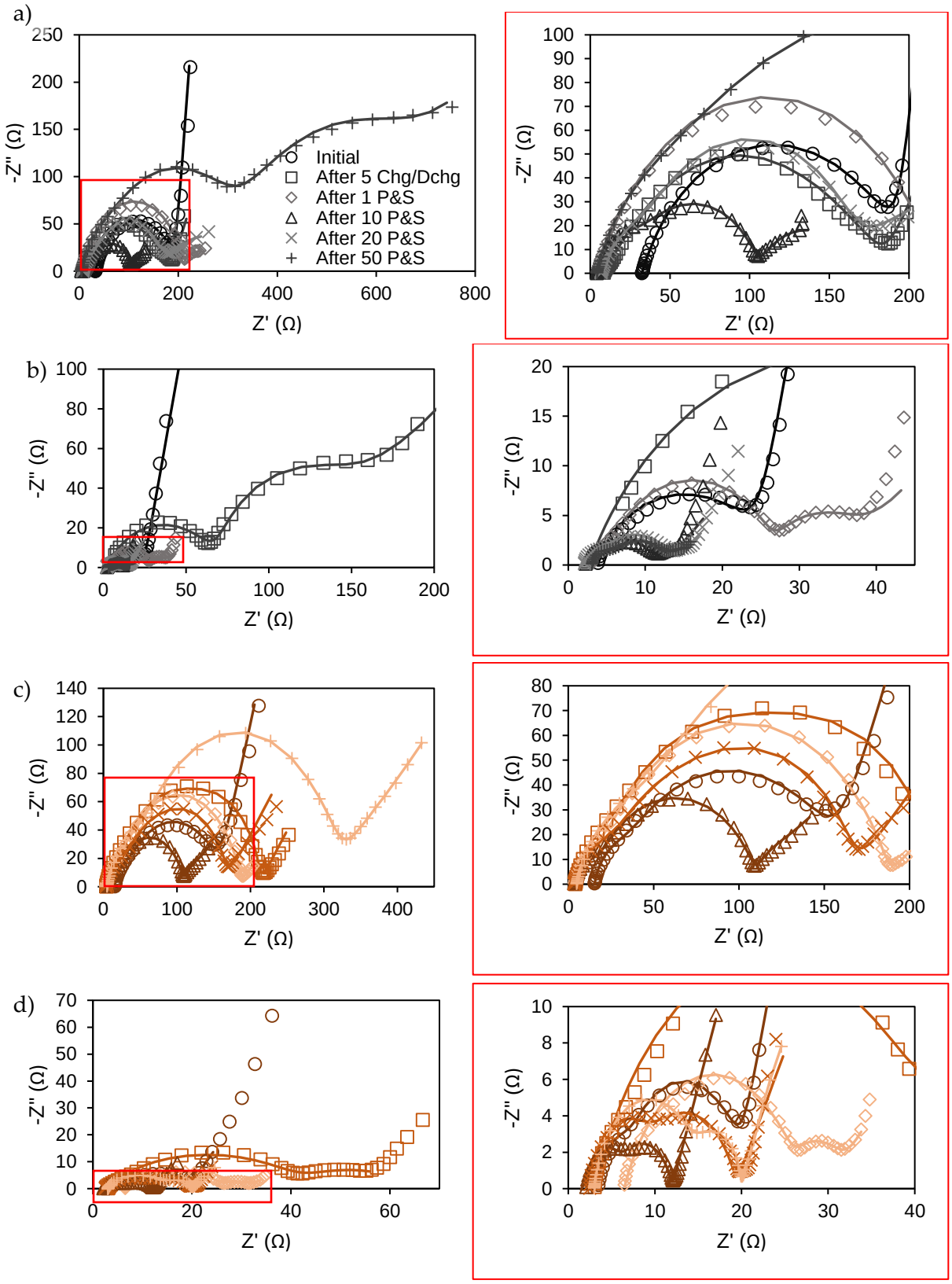

Figure 38. EIS data for selected samples: a) G2F2, b) G3F3, c) P6F2, d) P7F3, where all data is displayed on the left and the close-up of the data is on the right. Within all the plots, the initial spectrum at OCV

after assembly is indicated by a circle (o), after five lithiation and delithiation cycles to 1V, the spectrum is indicated by a square (□), after the first plating and stripping cycle to 0.1V, the spectrum is indicated by a diamond (◊), after the 10th cycle, the spectrum is indicated by a triangle (Δ), after the 20th cycle, the spectrum is indicated by an 'x' (X) and after the 50th cycle, the spectrum is indicated by a plus sign (+).

To illustrate the proposed mechanisms of lithium intercalation/de-intercalation as well as lithium plating and stripping into graphite and CPFA in different electrolytes, the schematic in Figure 39 was prepared based on [104,108].

With the insertion of lithium ions at the edges of the graphite particles, the graphite interlayer thickness is expected to increase while SEI forms at the edges of the graphite layers. Alternatively, CPFA as a hard carbon does not experience interlayer distance increase and remains relatively stable. For this reason, hard carbons have been an attractive anode material in Li-ion batteries to mitigate the volume changes in the anode. When there is no solvent co-intercalation in the case of the carbonate-based electrolytes, SEI simply forms stably at the ends of graphene layers and Li ions are reversibly inserted and removed in both the graphite and CPFA. However, in the presence of ether-based solvents, there is an exfoliation of the graphene layers in both graphite and CPFA due to the co-intercalation of the ether molecules. While the oxygens on the DME molecules has been shown to interact very strongly with Li ions, the oxygens on the DOL molecules have less of an interaction [104]. With the close solvation shell formed first with the DME then the DOL molecules, the complex leads to the co-intercalation of these solvation shells. The graphite exfoliation then leads to an increased electrode surface area, and thus increased SEI formation on the newly created surfaces, and eventually contact resistance due to the SEI layers between the particles and loss of contact upon volume changes.

When the graphite and CPFA particles are lithiated beyond their capability, that is, beyond the formation of LiC_6, Li metal begins to nucleate as sites for Li plating. In graphite, this begins at the edges of the graphene sheets as Li ions can no longer be inserted into the interlayer. At this point, the graphite is also in a metallic state and Li easily plates on the basal planes of the exposed graphite layers and SEI is formed on the newly plated Li while more Li plates underneath the

SEI. With an increased surface area of the particles in ether-based electrolytes, there are more sites of Li metal nucleation as well for the plating and stripping of Li.

In CPFA, a slightly different mechanism takes place as hard carbons possess nanopores that are sites of nucleation for Li metal once the interlayer spacing can no longer be inserted with Li ions. These nanopores are then first filled with Li metal before Li continues to grow out of these nanopores. In a similar manner as with the graphite, SEI forms on the newly plated and exposed Li metal and more Li begins to be added underneath the SEI. SEI typically does not form within the nanopores due to their small size as the Li-solvent complex cannot easily fit into the nanopores, but rather, the Li ions diffuse into the nanopores. When the CPFA is also fully lithiated, it is expected that Li metal is easily capable of plating on all areas of the particles as well.

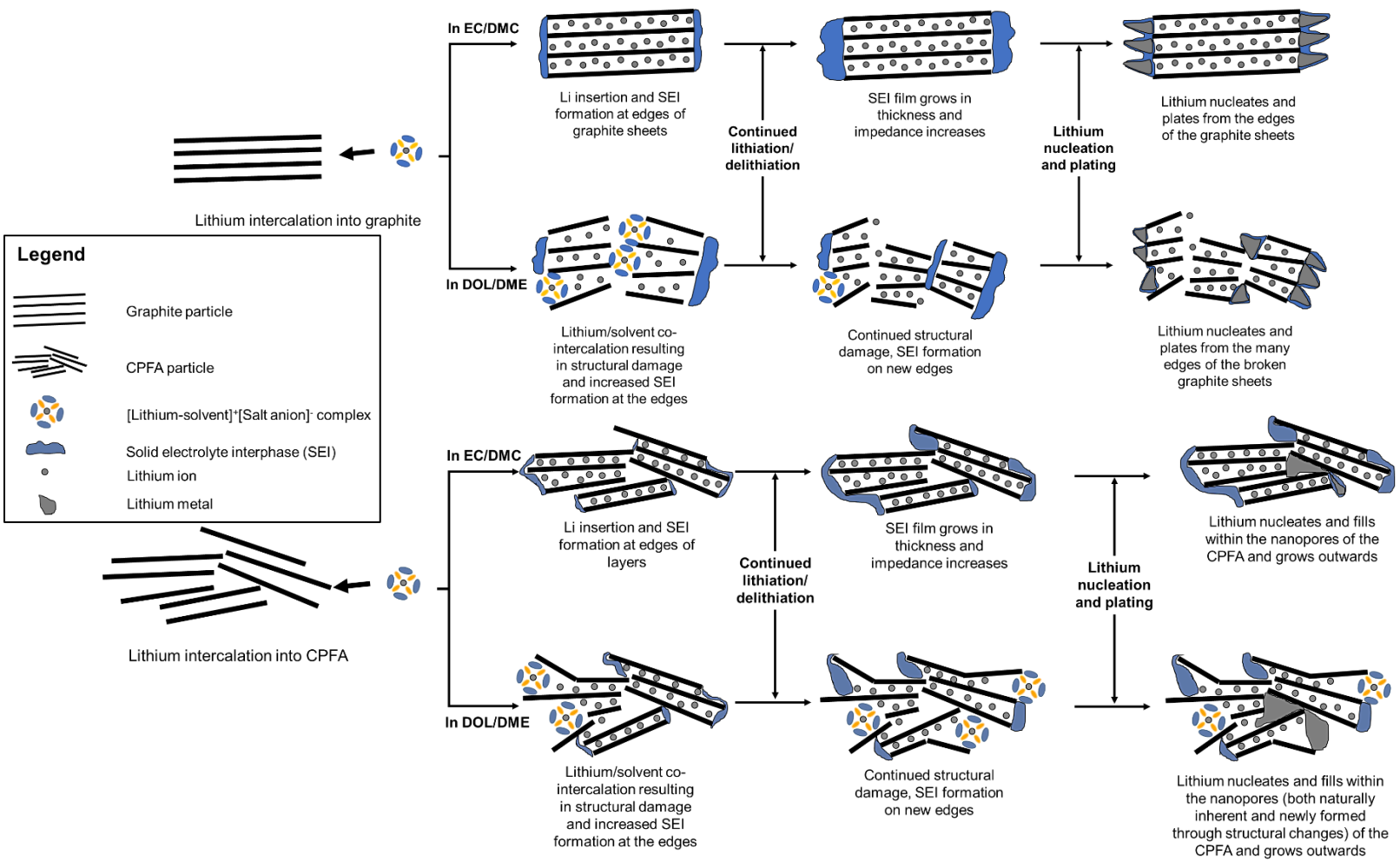

Figure 39. Schematic for proposed mechanisms of lithium lithiation/delithiation as well as plating in graphite and CPFA in ether- or carbonate-based electrolyte

The plating efficiency as a function of cycle number for each set of electrode materials, graphite, CPFA and copper, are plotted in Figure 40a), b) and c), respectively. Copper electrodes were tested in this set of experiments in order to obtain a comparison of SEI stability in different electrolytes without the convolution of data contributed by effects of volume change of the electrode or partially lithiated carbon (which would lead to some of the lithium plated being used for lithium insertion).

Across the three electrode materials, it is observed that F3 and F4, both ether-based electrolytes, perform worse in both the coulombic efficiency (CEff) and the stability of the CEff upon cycling than F1 and F2, the carbonate-based electrolytes. As this is present in also the copper samples, it is clear that the ether-based electrolytes decompose into unstable SEI, consuming more electrolyte upon cycling, and it is not simply an exfoliation of the carbon layers that causes poor CEff in the graphite and CPFA samples.

Another trend observed regardless of the substrate used is that F4, the 1M LiTFSI in 1:1 DOL/DME electrolyte, yields a very low CEff at the initial cycles but is afterwards quite relatively stable, despite its solvent's nature to exfoliate carbon particles. This suggests that the LiTFSI is effective at forming an SEI resistant to further decomposition after its initial reduction [109]. On the other hand, in the same solvent, the electrolyte with 1M $LiClO_4$ seems to experience a somewhat stable CEff at the initial cycles, but for graphite and CPFA, after 10-15 cycles, the CEff becomes unstable. Even in the copper sample, at about 15 cycles, the CEff becomes less stable than before, though less erratic compared to the carbon electrodes. This may indicate that the decomposition products of the $LiClO_4$ are not stable enough to form a protection layer for Li metal to be plated underneath without further side reactions with the electrolyte.

In the graphite samples, the electrolyte yielding the highest CEff while being the most stable is F2, 1M LiTFSI in EC/DMC, though even at its peak CEff, only 92.75% is achieved. This may be attributed to the substrate being graphite and the volume change present in the lithiation/delithiation between 0.1V and 0V during each plating and stripping cycle may have caused the constant need for more SEI to be "regenerated" from breakage during the volume change.

For CPFA, a number of interesting observations can be made. The first that is quite glaring is that all but one (F3) of the samples begin with a low CE around 70% and over the next 5-10 cycles, the CEff is built up and becomes somewhat stabilized. This is probably due to the filling, removal and refilling of the nanopores with metallic lithium during the first few cycles prior to plating on the surface of the CPFA. It is possible that some of the lithium is removed from the nanopores, but not all, leading to a lower CEff. Yet with the subsequent cycles, more and more of the nanopores are permanently filled with metallic lithium, leading to a stabilized CEff from lithium plating and stripping only on the surface of the CPFA particles.

Another important observation is the erratic yet consistently above 100% CEff of the F3 sample. This could be that some of the filled nanopores are slowly opened up by the ether-based electrolyte, allowing more regions of lithium metal to be accessible by the electrolyte so that what is stripped is more than just what is plated. A potential reason for why this phenomenon is observed by the F3 electrolyte with $LiClO_4$ salt and not with the F4 electrolyte with LiTFSI salt is that the complex formed, $[Li\text{-solvent}]^+[Salt\ anion]^-$, is smaller with the ClO_4^- anion than the $TFSI^-$ anion. As a result, the complex in the F3 electrolyte is more capable of co-intercalating into areas that the complex in the F4 electrolyte cannot, hence the increased instability in all the CEff's for the F3 samples in both the graphite and CPFA cells.

Lastly, unlike with graphite, F2 is not the most preferable electrolyte for CPFA, but rather F1 with 1M $LiClO_4$ is, with the CEff in most cycles above 95%. But absent of any effects with the carbon material on the copper substrate, for the carbonate-based electrolyte, the F2 electrolyte with the LiTFSI salt yields a much more stable CEff over the cycle life than does the F1 electrolyte, though only by about 2%. This may suggest that a presence of possibly any residual impurities such as hydrogen (C-H bonds) on the CPFA may contribute positively with the $LiClO_4$ decomposition products to form an even more stable SEI film over the CPFA. Although it is expected that at 1100°C, all of the oxygen-based functional groups would have been removed, C-H bonds may not be and thus would be sites of higher reactivity with the electrolyte and lithium.

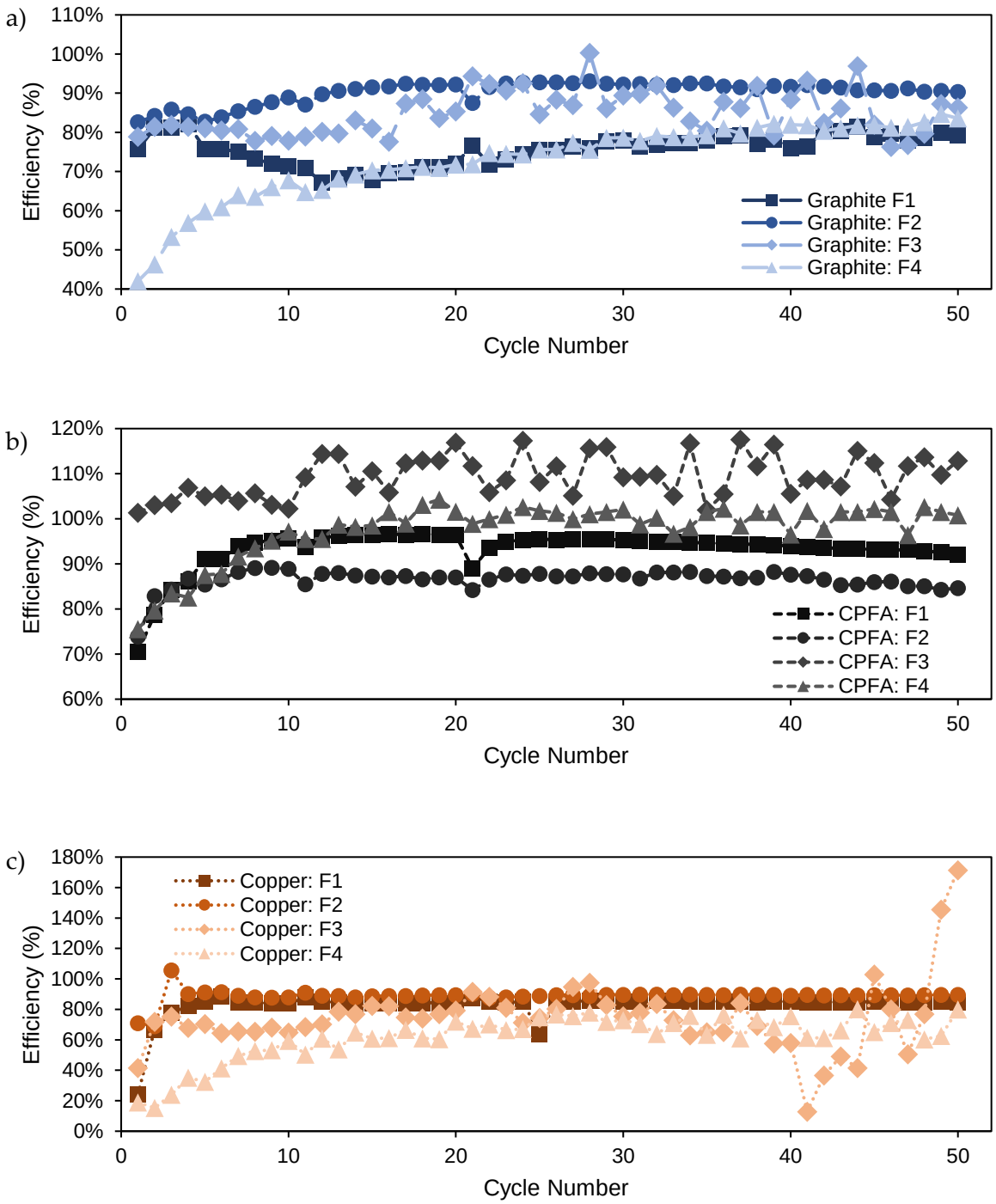

Figure 40. Galvanostatic cycling efficiency results of a) graphite, b) CPFA and c) copper electrodes in various electrolyte formulations, where F1 = 1M $LiClO_4$ in 1:1 EC/DMC, F2 = 1M LiTFSI in 1:1 EC/DMC, F3 = 1M $LiClO_4$ in 1:1 DOL/DME, F4 = 1M LiTFSI in 1:1 DOL/DME

To understand how the nature of the electrodes change as lithium plating substrates during the many plating and stripping cycles, the plating curve for select samples were compared at the 1st, 2nd and 20th plating step for the graphite, CPFA and copper electrodes (Figure 41). As a general observation, the samples with F3 (b, d, and f) all possess lower nucleation potentials due to the fact that DOL/DME has a lower surface energy on the carbon and copper surfaces than does EC/DMC due to its low viscosity. Additionally, most samples that cycle stably experience a reduction in nucleation overpotential when comparing the 1st plating to the 20th plating. The exception to this appears to be the graphite cells (G2F2 and G3F3) where only a small reduction in nucleation overpotential is observed for G2F2 and a significant reduction in nucleation overpotential is observed for G3F3.

In the CPFA samples (c,d) it is clear that the initial two cycles are characterized by a downward slope prior to the valley that is indicative of a nucleation overpotential, while this is not observed in the 20th cycle. This is due to an over-lithiation/nucleation process within the nanopores of the CPFA prior to the nucleation of Li metal on the surfaces of the CPFA particles, proving the claim made previously on Li metal filling the nanopores in initial cycles resulting in poor CEff until the 10th-15th cycles.

One last observation is the unique plating curve of CPFA and copper with the F3 electrolyte. In the second cycle for both samples, the voltage contains a typical sharp downward peak for the nucleation overpotential, followed by an increase in potential that slowly slopes downwards before increasing again. This behaviour disappears slowly in the latter cycles for copper but in the CPFA sample, it is extended somewhat so that the secondary maximum of the overpotential is shifted from the middle of the plating cycle to near the end of the plating cycle. This behaviour in the initial cycling of symmetric Li vs. Li is typical and has been verified to be independent of any diffusional resistances but purely due to the spatially varying rate constant across the interphase at the electrode/electrolyte [110]. This disappears in later cycles when diffusional resistances do affect the transport of Li to the bulk electrode. It might be in the case of the CPFA sample with F3 that the solvent co-intercalation opens up many new surface areas that inhibit the presence of diffusional resistances even over the course of many cycles, as is apparent with the

low impedances shown in the EIS spectra in Figure 38d). However, this is merely speculation and further characterization and experiments would be required to determine a true explanation of the behaviour.

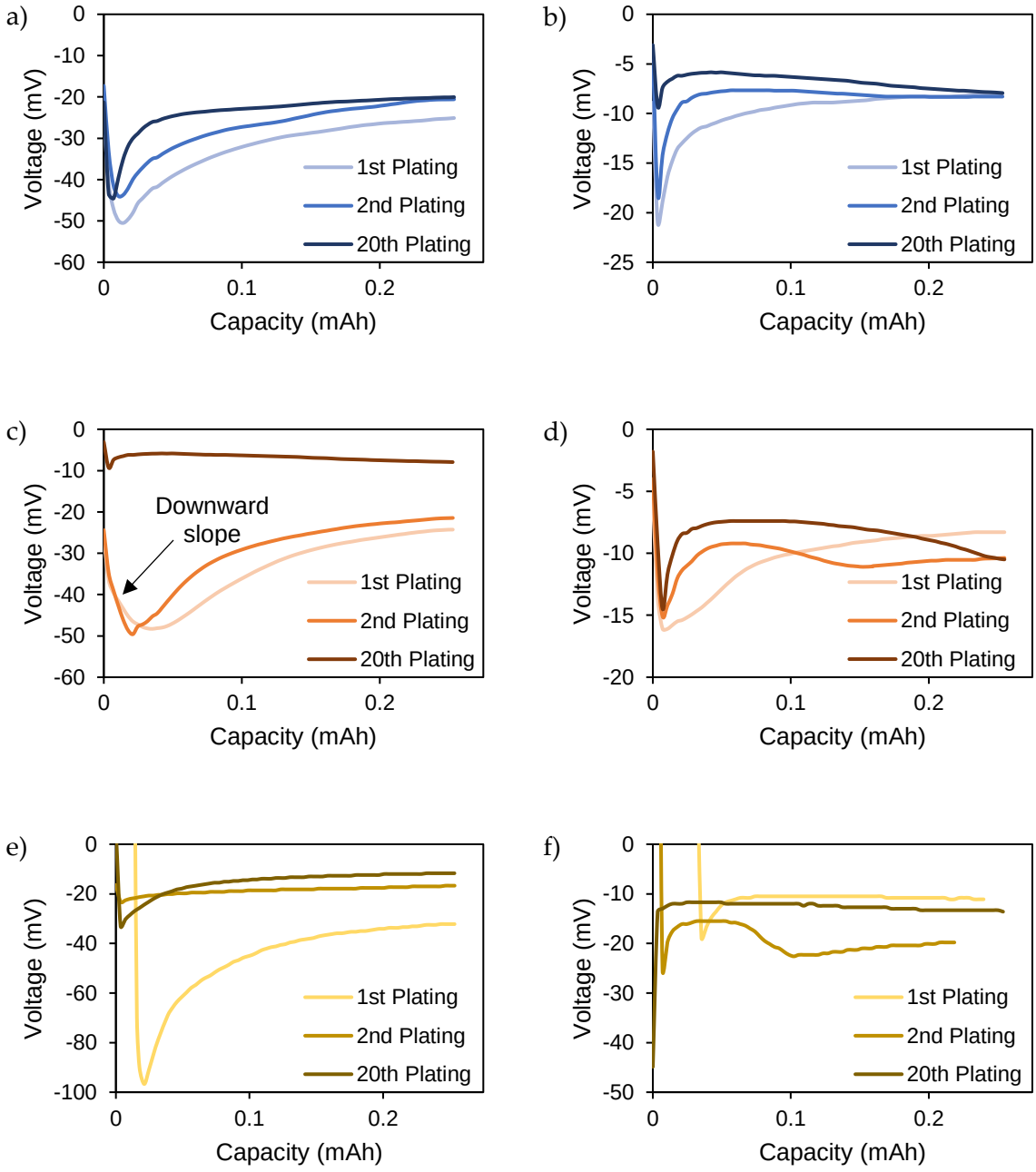

Figure 41. Plating curves for lithium on graphite, CPFA and copper at specific cycles for a) G2F2, b) G3F3, c) P2F2, d) P3F3, e) C10F2, f) C11F3

4.4 Conclusions

From this plating study of lithium metal on soft versus hard carbons, namely graphite versus CPFA, it was found that the best combination of carbon with electrolyte and salt yielding the highest CEff and cycling stability is CPFA with the 1M $LiClO_4$ in 1:1 EC/DMC electrolyte. Although this is the combination yielding the highest CEff, graphite as a Li plating substrate is not too poor as long as an appropriate electrolyte, specifically 1M LiTFSI in 1:1 EC/DMC as tested in this experiment, is used. Graphite with this electrolyte yielded a CEff that is just 2% lower than the CPFA with the $LiClO_4$ salt in carbonate-solvent. Furthermore, due to the nanopores present in hard carbons, the initial Li plating cycles on CPFA lose some capacity to the filling of these nanopores with metallic lithium that can be difficult to retrieve upon regular stripping. It is beneficial that solvent molecules cannot easily reach the nanopores to irreversibly react and form SEI, however, it is also not easily accessible to strip. This leads to a low CEff in the initial cycles. On the other hand, graphite does not experience a gradual increase in CEff in the same way with the exception of $LiClO_4$ in the ether-based electrolyte, which was suspected to produce unstable SEI that needed to be built up over many cycles to increase its stability in the system.

Also, it seems that while LiTFSI as a salt in the electrolyte is capable of decomposing into a more stable SEI in the case of graphite and copper, it does not quite exhibit the same effect with a hard carbon like CPFA. However, it is clear that between the ether-based electrolyte and the carbonate-based electrolyte, the ether-based electrolyte certainly leads to an accelerated degradation of the carbon material and forms highly unstable SEI through the exfoliation of the graphene layers in both graphite and CPFA. Aside from the property of it being capable of co-intercalating with Li ions, the ether-based solvents are found to decompose into structurally unstable SEI, as found in the copper samples, though the electrolyte with $LiClO_4$ is performs worse than that with LiTFSI. The ether-based electrolyte with the $LiClO_4$ salt also presented some anomalies in the plating voltage curve that may need to be further explored to mechanistically and physically understand the processes leading to the shape of the overpotential curve during plating.

While the electrolyte used in the electrodeposition of Li for the LSFB in Chapter 2 was F1 (1M $LiClO_4$ in 1:1 EC/DMC), from the results of both Chapter 3 and this chapter, it is clear that perhaps the LiTFSI salt should have been used for the introduction of a more stable SEI that may have improved the cycling of the full cell. This is under the assumption that the LIG material is more graphitic than it is like hard carbon.

In light of these findings, it is obvious that carbonate-based electrolytes are required to stably and effectively plate Li metal onto a carbon host (where the type of lithium salt used will depend on the hardness of the carbon). However, it is also known that carbonate-based electrolytes are not stable within the LiS battery system as the carbonate solvents tend to react with the lower order polysulfide species, leading to a reduced capacity over time [48], hence the need for ether-based electrolytes for battery cycling. This poses quite a challenge in order to be able to electrodeposit Li metal into a foreign host and then to be able to use it for cycling within a battery system as such. In a recent paper by Ming et al. [104], it was discovered that graphite lithiated and delithiated in a carbonate-based electrolyte to form stable SEI is insufficiently protected against solvent co-intercalation when transferred into an ether-based electrolyte. The Li-solvent complexes formed in the ether-based electrolyte were still capable of exfoliating the graphite, damaging the structure of the particles and leading to high irreversible capacities. This was found to reduce dramatically with the disruption of these complexes through a 2.5 time increase in salt concentration. Though this is not an ideal solution due to the high cost of lithium salts, it also points to the need for further developments in order to realize a low cost, high efficiency method of reducing Li metal use in Li-based batteries.

5.0 Conclusions and Future Work

5.1 Summary of Findings

In this work, proof-of-concept, flexible lithium-sulfur batteries based on LIG from commercial polymers were shown to be possible by sequentially patterning the cathode and anode in a 2D interdigitated structure and the step-by-step introduction of the active materials, sulfur and lithium, into the LIG fingers. The novel technique of heterogeneously nucleating sulfur followed by a melt imbibition was found to be effective to distribute sulfur over the surface area of the LIG while Ag NP seeds combined with RPP were successful in smoothly plating lithium (macroscopically) onto the rough LIG fingers at a relatively high current density of 1 mA/cm^2.

Initial cycling showed that the battery can achieve an energy density as high as 196.9 mWh/cm^3, which exceeds that of most published reports on lithium-ion microbatteries produced through nano-templating and microfabrication techniques. However, the retrievable capacity appeared to rapidly drop past the first cycle due to irreversible lithium-electrolyte reactions, which consumed the usable plated lithium. Furthermore, large pockets of agglomerated sulfur were found in the macropores of the graphene electrodes that are not electronically accessible by the electrolyte, thus inhibiting the electrodes from achieving their maximum capacity. This pointed to a dire need for a better understanding of the nature of LIG in order to properly tune characteristics such as the defectiveness, electrode density and surface area (and thus pore structure) as well as conductivity so that LIG can be a better substrate and host for electrochemical devices.

From studying various laser parameters, it was found that denser electrodes could be achieved with higher surface area by using a lower laser power at the expense of decreased conductivity. However, by annealing the material through multiple laser passes or defocusing of the beam, the LIG film can become more conductive. From additional analysis, the LIG films were also found to be inhomogeneous along the height of the electrodes, particularly that the bottom of the films close to the PI film were more amorphous while the more graphenic regions of the film were found near the top, closer to the irradiation source.

Additionally, in light of the realization of the inhomogeneity of the LIG film, it was necessary to understand the behaviour and efficiency of using carbons as lithium plating substrates within different electrolytes. From studying a soft carbon versus a hard carbon and two different lithium salts and an ether-based electrolyte versus a carbonate-based electrolyte, it was generally determined that carbonate-based electrolytes are more ideal for the lithiation/delithiation of the carbon electrodes as well as forming stable protective solid electrolyte interphases (SEI). And as for the salt in the carbonate-based electrolyte, it was found that graphene was capable of being more efficiently plated with the LiTFSI salt while CPFA performed best with the $LiClO_4$ salt. Depending on the "hardness" or degree of sp^3 versus sp^2 regions within the carbon substrate, the solvent and salt of choice within the electrolyte may need to be adjusted or even combined together.

5.2 Recommendations for Future Work

Though the LSFB may not be a high performance microbattery, it has succeeded in its proof of concept, while being unoptimized in the finger spacing, LIG pore structure, active material loading etc. Other similar systems using the interdigitated electrodes can be pursued in attempts to better understand any battery chemistry system because of the open architecture which allows for many *in operando* techniques. For example, in the case of the LiS chemistry, it would be interesting to probe the location of polysulfide species which are active materials that migrate away during cycling. Additionally, the performance and failure modes of a near-stoichiometric LiS battery could be well studied in such an open architecture.

There is also another possibility for the poor Li utility in this Li-limited system. For RTILs, it was found that while the electrochemical stability windows are large, the cations may not always be stable. For example, in EMImTFSI, the $EMIm^+$ cation was reported to reduce while being unable to form a protective SEI layer on graphite. This led to the inability of it aiding the intercalation of Li into graphite despite reaching voltages of 0V vs. Li. [111] While this report was not focused on the effects of using RTIL for Li plating, the finding of the cation instability could

suggest that RTILs may not be suitable for Li plating in Li metal batteries, despite their improved safety over organic electrolytes. Thus, RTILs must be further researched for their fitness in Li metal battery systems.

In order to achieve a fully practically flexible system for a variety of applications, ideally the ionic liquid-based electrolyte would be converted to a gel electrolyte for confinement of the electrolyte. Additionally, a polar LiPSS scavenger could be added, such as PEI [112], to the gel matrix so that it can be beneficial in preventing the migration of LiPSS away from the cathode, thereby reducing the capacity of the cell over the cycle life.

As a material, LIG is promising because of its ease and speed of fabrication as well as its versatility with various substrates. However, though this work has contributed towards understanding the effects of various parameters on the pore structure, defectiveness and conductivity of these films, more work is required in order that more homogeneous electrodes can be formed towards its use in electrochemical applications. Ideally, there would also be methods to tune the hardness of the carbon formed. It is known that more sp^3 regions can be formed in the material, but perhaps with some other laser parameters and irradiation environments, the carbon can become more like hard carbon.

While the six parameters (two carbons, two solvent mixtures, two lithium salts) studied for the lithium electrodeposition investigation led to some interesting results regarding the nature of the interactions between the carbon and the lithium-electrolyte complexes, some of the speculation regarding the size of the complex and the ability to exfoliate the layers ought to be further pursued through the use of other salts. It is particularly interesting that the hard carbon was found to be subject to the co-intercalation of ether solvent molecules. Traditionally, hard carbons were thought to be resistive to co-intercalation due to their amorphous and non-graphitizable nature. Continued study on various types of ether solvents and their effects on co-intercalation of hard carbons could be of interest. Also, the unique plating voltage profile of 1M $LiClO_4$ in 1:1 DOL/DME could be investigated in terms of the diffusional and kinetic changes within the system that produces it. Though it has been shown that the carbonate-based

electrolytes are better for lithium electrodeposition onto graphite and CPFA, the full LiS system cannot cycle in a carbonate-based electrolyte. Thus, either modifications and additives would need to be added into an ether-based electrolyte or possibly other electrolytes would need to be explored in the future.

6.0 References

[1] "Mobile and tablet internet usage exceeds desktop for first time worldwide | StatCounter Global Stats." [Online]. Available: http://gs.statcounter.com/press/mobile-and-tablet-internet-usage-exceeds-desktop-for-first-time-worldwide. [Accessed: 07-May-2018].

[2] A. Voice, "The Flexible Tech Revolution, and What It Can Do For Your Organization," *Forbes*, Feb-2017.

[3] "The Flexible Battery Market - The Independent Global Source for the Flexible and Printed Electronics Industry." [Online]. Available: https://www.printedelectronicsnow.com/issues/2017-03-01/view_features/the-flexible-battery-market/46383. [Accessed: 07-May-2018].

[4] "Wearable Medical Technology – Opening New Frontiers for Healthcare! | The Longevity Network." [Online]. Available: https://www.longevitynetwork.org/news/wearable-medical-technology-opening-new-frontiers-healthcare/. [Accessed: 18-Jun-2018].

[5] "Smart Card Working, Applications and Access Control Advantages." [Online]. Available: https://www.elprocus.com/working-of-smart-card/. [Accessed: 18-Jun-2018].

[6] "Introduction to VeChain's new Partner: Jiangsu Printed Electronics Co., Ltd." [Online]. Available: https://medium.com/@vechainofficial/introduction-to-vechains-new-partner-jiangsu-printed-electronics-co-ltd-e6b87582e3c2. [Accessed: 18-Jun-2018].

[7] M. Winter and R. J. Brodd*, "What Are Batteries, Fuel Cells, and Supercapacitors?," 2004.

[8] X. He, "Flexible, Printed and Thin Film Batteries 2016-2026: Technologies, Markets, Players: IDTechEx," *IDTechEx*. [Online]. Available: https://www.idtechex.com/research/reports/flexible-printed-and-thin-film-batteries-2016-2026-technologies-markets-players-000463.asp. [Accessed: 21-May-2018].

[9] J. H. Pikul, H. Gang Zhang, J. Cho, P. V. Braun, and W. P. King, "High-power lithium ion

microbatteries from interdigitated three-dimensional bicontinuous nanoporous electrodes," *Nat. Commun.*, vol. 4, p. 1732, Apr. 2013.

[10] M. Koo *et al.*, "Bendable Inorganic Thin-Film Battery for Fully Flexible Electronic Systems," *Nano Lett.*, vol. 12, no. 9, pp. 4810–4816, Sep. 2012.

[11] L. Li *et al.*, "A Foldable Lithium–Sulfur Battery," *ACS Nano*, vol. 9, no. 11, pp. 11342–11350, Nov. 2015.

[12] L. Li *et al.*, "High-Performance Solid-State Supercapacitors and Microsupercapacitors Derived from Printable Graphene Inks," *Adv. Energy Mater.*, vol. 6, no. 20, p. 1600909, Oct. 2016.

[13] L. Hu, H. Wu, and Y. Cui, "Printed energy storage devices by integration of electrodes and separators into single sheets of paper," *Appl. Phys. Lett.*, vol. 96, no. 18, p. 183502, May 2010.

[14] M. F. El-Kady, V. Strong, S. Dubin, and R. B. Kaner, "Laser Scribing of High-Performance and Flexible Graphene-Based Electrochemical Capacitors," *Science (80-.).*, vol. 335, no. 6074, pp. 1326–1330, Mar. 2012.

[15] J. Lin *et al.*, "Laser-induced porous graphene films from commercial polymers," *Nat. Commun.*, vol. 5, p. 5714, Dec. 2014.

[16] L. Li *et al.*, "High-Performance Pseudocapacitive Microsupercapacitors from Laser-Induced Graphene," *Adv. Mater.*, vol. 28, no. 5, pp. 838–845, Feb. 2016.

[17] M. A. Pope and I. A. Aksay, "Structural Design of Cathodes for Li-S Batteries," *Adv. Energy Mater.*, vol. 5, no. 16, p. 1500124, Aug. 2015.

[18] "The toll of the cobalt mining industry on health and the environment - CBS News." [Online]. Available: https://www.cbsnews.com/news/the-toll-of-the-cobalt-mining-industry-congo/. [Accessed: 10-Jul-2018].

[19] X. Ji, K. T. Lee, and L. F. Nazar, "A highly ordered nanostructured carbon–sulphur cathode for lithium–sulphur batteries," *Nat. Mater.*, vol. 8, no. 6, pp. 500–506, Jun. 2009.

[20] H. Pan *et al.*, "Non-encapsulation approach for high-performance Li-S batteries through controlled nucleation and growth," *Nat. Energy*.

[21] "What is triboelectric generator? How does it work? - Quora." [Online]. Available: https://www.quora.com/What-is-triboelectric-generator-How-does-it-work. [Accessed: 18-Jun-2018].

[22] "Thermoelectric Energy Generation." [Online]. Available: http://large.stanford.edu/courses/2012/ph240/doshay2/. [Accessed: 18-Jun-2018].

[23] "Piezoelectric materials - NamesakExperT." [Online]. Available: http://namesake-expert.blogspot.com/2010/12/piezoelectric-materials.html. [Accessed: 18-Jun-2018].

[24] F. R. Fan, W. Tang, and Z. L. Wang, "Flexible Nanogenerators for Energy Harvesting and Self-Powered Electronics," *Adv. Mater.*, vol. 28, no. 22, pp. 4283–4305, Jun. 2016.

[25] V. L. Pushparaj *et al.*, "Flexible energy storage devices based on nanocomposite paper."

[26] C. Liu, Z. Yu, D. Neff, A. Zhamu, and B. Z. Jang, "Graphene-Based Supercapacitor with an Ultrahigh Energy Density," *Nano Lett.*, vol. 10, no. 12, pp. 4863–4868, Dec. 2010.

[27] S. Hu, R. Rajamani, and X. Yu, "Flexible solid-state paper based carbon nanotube supercapacitor," *Appl. Phys. Lett.*, vol. 100, no. 10, p. 104103, Mar. 2012.

[28] L. Yuan *et al.*, "Paper-Based Supercapacitors for Self-Powered Nanosystems," *Angew. Chemie*, vol. 124, no. 20, pp. 5018–5022, May 2012.

[29] Z. Weng, Y. Su, D.-W. Wang, F. Li, J. Du, and H.-M. Cheng, "Graphene-Cellulose Paper Flexible Supercapacitors," *Adv. Energy Mater.*, vol. 1, no. 5, pp. 917–922, Oct. 2011.

[30] A. M. Gaikwad, A. C. Arias, and D. A. Steingart, "Recent Progress on Printed Flexible Batteries: Mechanical Challenges, Printing Technologies, and Future Prospects."

[31] Q. Li and H. Ardebili, "Flexible thin-film battery based on solid-like ionic liquid-polymer electrolyte," *J. Power Sources*, vol. 303, pp. 17–21, Jan. 2016.

[32] Z. Tehrani *et al.*, "Ultra-thin flexible screen printed rechargeable polymer battery for wearable electronic applications," *Org. Electron.*, vol. 26, pp. 386–394, Nov. 2015.

[33] M. D. Patel *et al.*, "Vertically oriented MoS 2 nanoflakes coated on 3D carbon nanotubes for next generation Li-ion batteries," 2016.

[34] Y. Zhang, Y. Liu, and M. Liu, "Nanostructured Columnar Tin Oxide Thin Film Electrode for Lithium Ion Batteries."

[35] J.-S. Kim *et al.*, "A Half Millimeter Thick Coplanar Flexible Battery with Wireless Recharging Capability," *Nano Lett.*, vol. 15, no. 4, pp. 2350–2357, Apr. 2015.

[36] J. Song *et al.*, "Solid-state microscale lithium batteries prepared with microfabrication processes," *J. Micromech. Microeng*, vol. 19, pp. 45004–6, 2009.

[37] C. W. Foster *et al.*, "3D Printed Graphene Based Energy Storage Devices," *Sci. Rep.*, vol. 7, p. 42233, Mar. 2017.

[38] Y. Wang *et al.*, "3D-Printed All-Fiber Li-Ion Battery toward Wearable Energy Storage," *Adv. Funct. Mater.*, vol. 27, no. 43, p. 1703140, Nov. 2017.

[39] N. Nitta, F. Wu, J. T. Lee, and G. Yushi, "Li-ion battery materials: present and future," *Mater. Today*, vol. 18, no. 5, pp. 252–264, 2015.

[40] A. Rosenman, E. Markevich, G. Salitra, D. Aurbach, A. Garsuch, and F. F. Chesneau, "Review on Li-Sulfur Battery Systems: an Integral Perspective," *Adv. Energy Mater.*, vol. 5, no. 16, p. 1500212, Aug. 2015.

[41] L. Borchardt, M. Oschatz, and S. Kaskel, "Carbon Materials for Lithium Sulfur Batteries - Ten Critical Questions," *Chem. - A Eur. J.*, vol. 22, no. 22, pp. 7324–7351, May 2016.

[42] E. Peled and S. Menkin, "Review—SEI: Past, Present and Future," *J. Electrochem. Soc.*, vol. 164, no. 7, pp. A1703–A1719, Jun. 2017.

[43] W. Xu *et al.*, "Lithium metal anodes for rechargeable batteries."

[44] K. Yan *et al.*, "Selective deposition and stable encapsulation of lithium through heterogeneous seeded growth," *Nat. Energy*, vol. 1, no. 3, p. 16010, Feb. 2016.

[45] Ratyakshi and R.P. Chauhan, "Colloidal Synthesis of Silver Nano Particles," *Asian J. Chem.*, vol. 21, no. 10, pp. S113-116, 2009.

[46] M. S. Chandrasekar and M. Pushpavanam, "Pulse and pulse reverse plating—Conceptual, advantages and applications," *Electrochim. Acta*, vol. 53, no. 8, pp. 3313–3322, Mar. 2008.

[47] H. Yang, E. O. Fey, B. D. Trimm, N. Dimitrov, and M. S. Whittingham, "Effects of Pulse Plating on lithium electrodeposition, morphology and cycling efficiency," *J. Power Sources*, vol. 272, pp. 900–908, Dec. 2014.

[48] J. Gao, M. A. Lowe, Y. Kiya, H. Ector, and D. Abru~, "Effects of Liquid Electrolytes on the Charge/Discharge Performance of Rechargeable Lithium/Sulfur Batteries: Electrochemical and in-Situ X-ray Absorption Spectroscopic Studies," *J. Phys. Chem. C*, vol. 115, pp. 25132–25137, 2011.

[49] X.-B. Cheng, J.-Q. Huang, and Q. Zhang, "Review—Li Metal Anode in Working Lithium-Sulfur Batteries," *J. Electrochem. Soc.*, vol. 165, no. 1, pp. 6058–6072, 2018.

[50] M. Wall, "The Raman Spectroscopy of Graphene and the Determination of Layer Thickness Raman Spectroscopy and the Raman Spectrum of Graphene."

[51] M. Yabushita, *A study on catalytic conversion of non-food biomass into chemicals : fusion of chemical sciences and engineering*. .

[52] A. C. Ferrari and J. Robertson, "Interpretation of Raman spectra of disordered and amorphous carbon."

[53] X. Yang *et al.*, "Liquid-mediated dense integration of graphene materials for compact capacitive energy storage.," *Science*, vol. 341, no. 6145, pp. 534–7, Aug. 2013.

[54] Y. Chyan, R. Ye, Y. Li, S. P. Singh, C. J. Arnusch, and J. M. Tour, "Laser-Induced Graphene by Multiple Lasing: Toward Electronics on Cloth, Paper, and Food," *ACS Nano*, vol. 12, no.

3, pp. 2176–2183, Mar. 2018.

[55] R. Ye *et al.*, "Laser-Induced Graphene Formation on Wood," *Adv. Mater.*, vol. 29, no. 37, p. 1702211, Oct. 2017.

[56] A. C. Ferrari *et al.*, "Raman Spectrum of Graphene and Graphene Layers."

[57] P. Strubel, S. Thieme, C. Weller, H. Althues, and S. Kaskel, "Insights into the redistribution of sulfur species during cycling in lithium-sulfur batteries using physisorption methods," *Nano Energy*, vol. 34, pp. 437–441, Apr. 2017.

[58] K. R. Kim, S.-H. Yu, and Y.-E. Sung, "Enhancement of cycle performance of Li–S batteries by redistribution of sulfur," *Chem. Commun.*, vol. 52, no. 6, pp. 1198–1201, Jan. 2016.

[59] M. Paunovic, M. Schlesinger, and John Wiley & Sons., *Fundamentals of electrochemical deposition*. Wiley, 2006.

[60] L. Gireaud, S. Grugeon, S. Laruelle, B. Yrieix, and J.-M. Tarascon, "Lithium metal stripping/plating mechanisms studies: A metallurgical approach," 2006.

[61] K. Kwon, F. Kong, F. Mclarnon, and J. W. Evans, "Characterization of the SEI on a Carbon Film Electrode by Combined EQCM and Spectroscopic Ellipsometry," 2003.

[62] "Product Matrix | BrightVolt." [Online]. Available: https://www.brightvolt.com/product-matrix/. [Accessed: 06-Jul-2018].

[63] "Thin Flexible Batteries | Battery Solutions." [Online]. Available: https://www.bluesparktechnologies.com/index.php/products-and-services/battery-products. [Accessed: 06-Jul-2018].

[64] "Panasonic Develops Bendable, Twistable, Flexible Lithium-ion Battery | Headquarters News | Panasonic Newsroom Global." [Online]. Available: https://news.panasonic.com/global/press/data/2016/09/en160929-8/en160929-8.html. [Accessed: 06-Jul-2018].

[65] C. Jin *et al.*, "3D lithium metal embedded within lithiophilic porous matrix for stable

lithium metal batteries," *Nano Energy*, vol. 37, pp. 177–186, Jul. 2017.

[66] D. Lin *et al.*, "Layered reduced graphene oxide with nanoscale interlayer gaps as a stable host for lithium metal anodes," *Nat. Nanotechnol.*, vol. 11, no. 7, pp. 626–632, Jul. 2016.

[67] A. K. Geim, "Graphene: status and prospects.," *Science*, vol. 324, no. 5934, pp. 1530–4, Jun. 2009.

[68] D. Chen, L. Tang, and J. Li, "Graphene-based materials in electrochemistry," *Chem. Soc. Rev.*, vol. 39, no. 8, p. 3157, Jul. 2010.

[69] F. Torrisi *et al.*, "Inkjet-Printed Graphene Electronics," *ACS Nano*, vol. 6, no. 4, pp. 2992–3006, Apr. 2012.

[70] K. Parvez, S. Yang, X. Feng, and K. Müllen, "Exfoliation of graphene via wet chemical routes," *Synth. Met.*, vol. 210, pp. 123–132, Dec. 2015.

[71] J. M. Tour, "Top-Down versus Bottom-Up Fabrication of Graphene-Based Electronics."

[72] W. Zhao, M. Fang, F. Wu, H. Wu, L. Wang, and G. Chen, "Preparation of graphene by exfoliation of graphite using wet ball milling," *J. Mater. Chem.*, vol. 20, no. 28, p. 5817, Jul. 2010.

[73] S. Song, F. Ma, G. Wu, D. Ma, W. Geng, and J. Wan, "Facile self-templating large scale preparation of biomass-derived 3D hierarchical porous carbon for advanced supercapacitors," *J. Mater. Chem. A*, vol. 3, no. 35, pp. 18154–18162, Aug. 2015.

[74] L. Yao *et al.*, "Scalable 2D Hierarchical Porous Carbon Nanosheets for Flexible Supercapacitors with Ultrahigh Energy Density," *CommuniCation*, vol. 17060541, no. 9.

[75] T. Purkait, G. Singh, M. Singh, D. Kumar, and R. S. Dey, "Large area few-layer graphene with scalable preparation from waste biomass for high-performance supercapacitor," *Sci. Rep.*, vol. 7, no. 1, p. 15239, Dec. 2017.

[76] T. Takeichi, Y. Eguchi, Y. Kaburagi, Y. Hishiyama, and M. Inagaki, "Carbonization and graphitization of Kapton-type polyimide films prepared from polyamide alkyl ester,"

Carbon N. Y., vol. 36, no. 1–2, pp. 117–122, Jan. 1998.

[77] F. Wang *et al.*, "Laser-induced graphene: preparation, functionalization and applications," *Mater. Technol.*, vol. 33, no. 5, pp. 340–356, 2018.

[78] Z. Peng, J. Lin, R. Ye, E. L. G. Samuel, and J. M. Tour, "Flexible and Stackable Laser Induced Graphene Supercapacitors," *ACS Appl. Mater. Interfaces*, 2015.

[79] L. Li *et al.*, "High-Performance Pseudocapacitive Microsupercapacitors from Laser-Induced Graphene," *Adv. Mater.*, 2016.

[80] J. Zhang, C. Zhang, J. Sha, H. Fei, Y. Li, and J. M. Tour, "Efficient Water-Splitting Electrodes Based on Laser-Induced Graphene," *ACS Appl. Mater. Interfaces*, 2017.

[81] A. Lamberti, F. Clerici, M. Fontana, and L. Scaltrito, "A Highly Stretchable Supercapacitor Using Laser-Induced Graphene Electrodes onto Elastomeric Substrate," *Adv. Energy Mater.*, vol. 6, no. 10, p. 1600050, May 2016.

[82] C. M. Tittle, D. Yilman, M. A. Pope, and C. J. Backhouse, "Robust Superhydrophobic Laser-Induced Graphene for Desalination Applications," *Adv. Mater. Technol.*, vol. 3, no. 2, p. 1700207, Feb. 2018.

[83] Y. Li *et al.*, "Laser-Induced Graphene in Controlled Atmospheres: From Superhydrophilic to Superhydrophobic Surfaces," *Adv. Mater.*, vol. 29, no. 27, p. 1700496, Jul. 2017.

[84] Y. Li *et al.*, "Laser-Induced Graphene in Controlled Atmospheres: From Superhydrophilic to Superhydrophobic Surfaces," *Adv. Mater.*, 2017.

[85] R. Ye *et al.*, "Laser-Induced Graphene Formation on Wood," *Adv. Mater.*, 2017.

[86] J. A. Lochala, H. Zhang, Y. Wang, O. Okolo, X. Li, and J. Xiao, "Practical Challenges in Employing Graphene for Lithium-Ion Batteries and Beyond," *Small Methods*, vol. 1, no. 6, p. 1700099, Jun. 2017.

[87] Y. Liu, D. Lin, Z. Liang, J. Zhao, K. Yan, and Y. Cui, "Lithium-coated polymeric matrix as a minimum volume-change and dendrite-free lithium metal anode," *Nat. Commun.*, vol. 7,

p. 10992, Mar. 2016.

[88] S. M. Kim, A. Hsu, and Y.-H. Lee, "Thinning of large-area graphene film from multilayer to bilayer with a low-power CO2 laser."

[89] W. Xu *et al.*, "Lithium metal anodes for rechargeable batteries," *Energy Environ. Sci.*, vol. 7, no. 2, pp. 513–537, Jan. 2014.

[90] X.-B. Cheng, R. Zhang, C.-Z. Zhao, F. Wei, J.-G. Zhang, and Q. Zhang, "A Review of Solid Electrolyte Interphases on Lithium Metal Anode," *Adv. Sci.*, vol. 3, no. 3, p. 1500213, Mar. 2016.

[91] J. Park, J. Jeong, Y. Lee, M. Oh, M.-H. Ryou, and Y. M. Lee, "Micro-Patterned Lithium Metal Anodes with Suppressed Dendrite Formation for Post Lithium-Ion Batteries," *Adv. Mater. Interfaces*, vol. 3, no. 11, p. 1600140, Jun. 2016.

[92] L. Shi *et al.*, "High-safety lithium-ion sulfur battery with sulfurized polyacrylonitrile cathode, prelithiated SiOx/C anode and carbonate-based electrolyte," *J. Alloys Compd.*, vol. 723, pp. 974–982, Nov. 2017.

[93] Y. Yan, Y.-X. Yin, S. Xin, J. Su, Y.-G. Guo, and L.-J. Wan, "High-safety lithium-sulfur battery with prelithiated Si/C anode and ionic liquid electrolyte," *Electrochim. Acta*, vol. 91, pp. 58–61, Feb. 2013.

[94] F. Holtstiege, P. Bärmann, R. Nölle, M. Winter, and T. Placke, "Pre-Lithiation Strategies for Rechargeable Energy Storage Technologies: Concepts, Promises and Challenges," *Batteries*, vol. 4, no. 1, p. 4, Jan. 2018.

[95] S. F. Liu *et al.*, "Recent development in lithium metal anodes of liquid-state rechargeable batteries," *J. Alloys Compd.*, vol. 730, pp. 135–149, Jan. 2018.

[96] Y. Liu, D. Lin, Z. Liang, J. Zhao, K. Yan, and Y. Cui, "Lithium-coated polymeric matrix as a minimum volume-change and dendrite-free lithium metal anode," *Nat. Commun.*, vol. 7, p. 10992, Mar. 2016.

[97] K. Xu, "Nonaqueous Liquid Electrolytes for Lithium-Based Rechargeable Batteries."

[98] A. E. Sedykh, E. G. Gordeev, E. O. Pentsak, and V. P. Ananikov, "Shielding the chemical reactivity using graphene layers for controlling the surface properties of carbon materials," *Phys. Chem. Chem. Phys.*, vol. 18, no. 6, pp. 4608–4616, Feb. 2016.

[99] H. F. Bettinger*, "The Reactivity of Defects at the Sidewalls of Single-Walled Carbon Nanotubes: The Stone−Wales Defect," 2005.

[100] J. Yao, H. Wang, J. Liu, K.-Y. Chan, L. Zhang, and N. Xu, "Preparation of colloidal microporous carbon spheres from furfuryl alcohol," *Carbon N. Y.*, vol. 43, no. 8, pp. 1709–1715, Jul. 2005.

[101] K. M. Shaju, G. V. Subba Rao, and B. V. R. Chowdari, "Influence of Li-Ion Kinetics in the Cathodic Performance of Layered Li(Ni[sub 1/3]Co[sub 1/3]Mn[sub 1/3])O[sub 2]," *J. Electrochem. Soc.*, vol. 151, no. 9, p. A1324, Sep. 2004.

[102] Z. Q. Li, C. J. Lu, Z. P. Xia, Y. Zhou, and Z. Luo, "X-ray diffraction patterns of graphite and turbostratic carbon," *Carbon N. Y.*, vol. 45, no. 8, pp. 1686–1695, Jul. 2007.

[103] K. G. Gallagher, D. W. Dees, A. N. Jansen, D. P. Abraham, and S.-H. Kang, "A Volume Averaged Approach to the Numerical Modeling of Phase-Transition Intercalation Electrodes Presented for Li x C 6," *J. Electrochem. Soc.*, vol. 159159, no. 12129, pp. 2029–2037, 2012.

[104] J. Ming *et al.*, "New Insights on Graphite Anode Stability in Rechargeable Batteries: Li Ion Coordination Structures Prevail over Solid Electrolyte Interphases," *ACS Energy Lett.*, vol. 3, no. 2, pp. 335–340, Feb. 2018.

[105] H. Kim *et al.*, "Exploiting Lithium-Ether Co-Intercalation in Graphite for High-Power Lithium-Ion Batteries," *Adv. Energy Mater.*, vol. 7, no. 19, p. 1700418, Oct. 2017.

[106] A. Shellikeri *et al.*, "Investigation of Pre-lithiation in Graphite and Hard-Carbon Anodes Using Different Lithium Source Structures," *J. Electrochem. Soc.*, vol. 164, no. 14, pp. A3914–

A3924, Dec. 2017.

[107] G. Bieker, M. Winter, and P. Bieker, "Electrochemical in situ investigations of SEI and dendrite formation on the lithium metal anode," *Phys. Chem. Chem. Phys.*, vol. 17, no. 14, pp. 8670–8679, Mar. 2015.

[108] X. Su, F. Dogan, J. Ilavsky, V. A. Maroni, D. J. Gosztola, and W. Lu, "Mechanisms for Lithium Nucleation and Dendrite Growth in Selected Carbon Allotropes."

[109] V. Sharova, A. Moretti, T. Diemant, A. Varzi, R. J. Behm, and S. Passerini, "Comparative study of imide-based Li salts as electrolyte additives for Li-ion batteries," *J. Power Sources*, vol. 375, pp. 43–52, Jan. 2018.

[110] K.-H. Chen *et al.*, "Dead lithium: mass transport effects on voltage, capacity, and failure of lithium metal anodes."

[111] M. Holzapfel *et al.*, "Stabilisation of lithiated graphite in an electrolyte based on ionic liquids: an electrochemical and scanning electron microscopy study," *Carbon N. Y.*, vol. 43, no. 7, pp. 1488–1498, Jun. 2005.

[112] W. Chen *et al.*, "A New Type of Multifunctional Polar Binder: Toward Practical Application of High Energy Lithium Sulfur Batteries," *Adv. Mater.*, vol. 29, no. 12, p. 1605160, Mar. 2017.